Yukon

Yukon

Exploration & Geology Technical Papers

2024

Yukon Geological Survey staff.

Back (left to right): *Alex Brubacher, Maurice Colpron, Tyler Ambrose, Amy Stuart, Derek Cronmiller, Rosie Cobbett, Carolyn Relf, Spencer Skerget, Chad Côté.*
Middle (left to right): *Panya Lipovsky, Emilie Stewart-Jones, David Moynihan.*
Front (left to right): *Sarah Ellis, Tiera Naber, Moya Painter, Sarah Schultz, Leyla Weston, Patrick Sack.*
Missing: *Tamara Annau, Amanda O'Connor, Sydney van Loon.*

Yukon

Yukon Exploration & Geology Technical Papers 2024

Edited by

L.H. Weston, A. Stuart,
S.K. Schultz, A.D. Brubacher,
and D.C. Cronmiller

Yukon Geological Survey

Energy, Mines and Resources

Government of Yukon

Published under the authority of the Department of Energy, Mines and Resources, Government of Yukon, https://yukon.ca.

Publié avec l'autorisation du Ministères de l'Énergie, des Mines et des Ressources du gouvernement du Yukon, https://yukon.ca.

ISSN 1718-8342 (online version)

Yukon Geological Survey publications can be obtained from:
Yukon Geological Survey
102-300 Main Street
Box 2703 (K-102)
Whitehorse, Yukon, Canada Y1A 2C6

email geology@yukon.ca

Yukon Geological Survey website https://yukon.ca/en/science-and-natural-resources/geology

In referring to this publication, please use the following citation:
Yukon Geological Survey, 2025. Yukon Exploration and Geology Technical Papers 2024.
L.H. Weston, A. Stuart, S.K. Schultz, A.D. Brubacher and D.C. Cronmiller (eds.), Yukon Geological Survey, 95 p.

Front cover photograph: View from a ridge looking south over Engineer Creek and the Dempster Highway below. (Photo by Emilie Stewart-Jones, Yukon Geological Survey.)

Preface

The Yukon Exploration and Geology (YEG) volumes include two publications: Yukon Exploration and Geology Overview, and Yukon Exploration and Geology Technical Papers. These key annual publications from the Yukon Geological Survey (Energy, Mines and Resources, Government of Yukon) highlight geoscience research and activities across the Yukon from the previous year. The YEG Overview includes four papers that provide summaries of the Yukon Geological Survey's staff activities, as well as exploration and development overviews for both the hardrock and placer industries in the Yukon. The YEG Technical Papers volume contains a number of current research reports on various geoscience projects across the territory. The YEG Overview is available in digital format and in a limited colour print run. The YEG Technical Papers volume is available in digital format only. All Yukon Geological Survey publications can be downloaded from our website, https://data.geology.gov.yk.ca/.

As in previous volumes, YEG 2024 aims to provide the most up-to-date information on mining and mineral exploration activity in the Yukon, both in the hardrock and placer sectors. The success of YEG relies on the continued contributions from prospectors, exploration and government geologists, mining companies, and academic students, all of whom are willing to contribute to public geoscience for the benefit of the scientific community, the public, and the mineral industry of the Yukon. Their work is greatly appreciated.

More importantly, I would like to acknowledge the support from our 14 Yukon First Nation partners whose lands and traditional territories we continue to work on. The mining industry and the valuable geoscience data that is gathered would not happen without their engagement and support. We look forward to strengthening and fostering honest and meaningful partnerships with all Yukon First Nations.

I hope you enjoy the volume. Any input or suggestions you may have to improve future YEG publications are welcome. Please contact us at geology@yukon.ca.

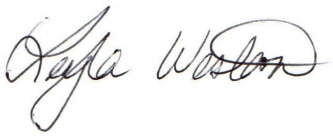

Leyla Weston

Yukon Exploration and Geology Technical Papers 2024

Table of Contents

Valley deposit: A geological introduction and overview

Sergio Gamonal, Thomas Branson, Andy Turner, Hannah Couper and Sunny Yao*

Snowline Gold Corp.

Gamonal, S., Branson, T., Turner, A., Couper, H. and Yao, S., 2025. Valley deposit: A geological introduction and overview. *In*: Yukon Exploration and Geology Technical Papers 2024, L.H. Weston, A. Stuart, S.K. Schultz, A.D. Brubacher and D.C. Cronmiller (eds.), Yukon Geological Survey, p. 1–18.

Abstract

The Valley deposit is located in east-central Yukon, 367 km northeast of Whitehorse. In 2012, Golden Predator Mining Corp. originally sampled gold-mineralized quartz veins in outcrop at what is now known as the Valley deposit. Snowline Gold Corp. subsequently followed up on the mineralization through diamond drilling from 2021 to present. The Valley deposit is a reduced intrusion-related gold system characterized by sheeted quartz-carbonate veins hosting free gold and associated lead-bismuth-tellurium sulphides, within a multi-phase, reduced granodiorite intrusion. The phases of the intrusion are physically and chemically distinct, exhibiting the evolution of a magma over time. Gold mineralization is strongly associated with vein density, whereby vein densities of >10 veins per metre correlate with gold grades of >1 g/t. In June 2024, the initial mineral resource estimate defined an Indicated Mineral Resource of 76 Mt at 1.66 g/t Au for 4.05 Moz Au, and an Inferred Mineral Resource of 81 Mt at 1.25 g/t Au for 3.26 Moz Au using a 0.4 g/t Au cut-off grade (Burrell et al., 2024).

Plain language summary

Snowline Gold Corp. is a Yukon-based mineral exploration company that has carried out a substantial drilling campaign between 2021 and 2024 on the newly discovered Valley deposit. The deposit is located in east-central Yukon, 367 km northeast of Whitehorse, and 227 km east of Mayo. The Valley deposit is characterized by an intrusive rock containing a high abundance of gold-bearing quartz veins. The deposit covers an area approximately 700 by 400 m and extends to a depth of 400 m. The gold mineralization occurs at surface and is of unusually high grade for this type of deposit. This high-quality discovery has sparked interest for gold exploration in the eastern Yukon, and has stimulated further exploration for similar styles of mineralized systems. In early 2024, an initial mineral resource estimate was completed on the Valley deposit, and in 2025 this will be updated to include the most recent drilling.

* tbranson@snowlinegold.com

Introduction

The Valley gold deposit (hereafter referred to as 'Valley') is located in east-central Yukon, near the headwaters of Old Cabin Creek, centred at 63°37'45"N and 131°18'03"W. It is situated 227 km east of the Village of Mayo and 367 km northeast of Whitehorse.

In 2012, evidence of gold mineralization at Valley was discovered by Shane and Luke Carlos while working for Golden Predator, who had optioned the original claims from 18526 Yukon Inc. A bedrock chip sample along the western edge of the deposit yielded 4.2 g/t Au over 4.7 m across one of the few outcrops along Old Cabin Creek, and a select sample from an arsenopyrite-rich quartz vein on the eastern edge of the intrusion returned 152 g/t Au. Both these samples were following up on a stream-sediment gold anomaly of 110 ppb Au identified 580 m downstream, collected the previous year. Prior to this sampling, exploration programs carried out in 1963 and 1968 by Dynasty Syndicate and Atlas Explorations Limited, respectively, had mapped the outline of the main intrusion and copper-bearing veins to the north of the Valley stock, but at that time, gold was not part of the geochemical analysis.

Intermittent mineral exploration was conducted in the region in the early 1980s by AGIP Canada Ltd., who were primarily assessing the regional intrusions for uranium potential and found the first indications of gold in the vicinity of Valley. At that time, exploration efforts were focused around the Emerald Lake area, located 10 km southeast of Valley. In 1996, Yukon Gold Corp. carried out a sizable exploration program, consisting of drilling at four targets within the Rogue plutonic complex, including at the Reid target, located 9 km east of Valley. However, due in large part to the Bre-X Minerals Ltd. scandal in 1997, and Yukon Gold Corp. having claims adjacent to Bre-X's deposit in Busang, Indonesia, the company went bankrupt and much of the work was never reported. Of note, the results from the one report that was published (Lueck, 1997) were enough to entice 18526 Yukon Inc. to the region and stake the original claims at Valley.

Since 2021, Snowline Gold Corp. has completed 124 diamond drillholes (123 NQ2, 1 PQ), totalling 52 785.7 m. The Valley deposit is remarkable for a number of reasons: it has relatively consistent and continuous high grades returned for the deposit style, which was previously thought to primarily host lower gold grades (<1 g/t Au); the highest grades at Valley are near surface and distributed in a favourable way for eventual development; and initial metallurgical test work has returned favourable average gold recoveries varying from 94 to 96% across a range of grades, material sizes and metallurgical approaches.

In 2024, Snowline published an initial mineral resource estimate that defined an Indicated Mineral Resource of 76 Mt at 1.66 g/t Au for 4.05 Moz Au and an Inferred Mineral Resource of 81 Mt at 1.25 g/t Au for 3.26 Moz Au using a 0.4 g/t Au cut-off grade (Burrell et al., 2024). This resource is based on drilling completed to the end of the 2023 field season, and does not consider the additional 25 000 m drilled at Valley during the 2024 field season.

Tectonic setting

The Valley deposit is situated within the Selwyn basin, which consists of Neoproterozoic to lower Paleozoic, predominantly off-shelf sedimentary sequences, and lesser volcanic sequences, derived from, and deposited on the southwestern margin of the North American craton (Fig. 1; Colpron et al., 2007; Colpron and Nelson, 2011). The basinal rocks (NAb, Fig. 1) were deposited in shallow to deep water marine settings along the ancestral North American continental platform (NAm, Fig. 1). Terranes currently found outboard of the Selwyn basin were emplaced during progressive tectonic accretion from the latest Permian to mid-Cretaceous (Nelson et al., 2013).

Initial accretion of the Yukon-Tanana terrane and associated oceanic terranes to the continental margin is believed to have occurred during the late Permian and early Triassic. This was followed by subsequent terrane accretion and deformation in the Early Jurassic to mid-Cretaceous (115–90 Ma). Strain associated with this collision was accommodated along the Dawson, Robert Service and Tombstone thrust faults. This led to deformation and lower to middle greenschist metamorphism of the Selwyn basin and younger rocks near the thrust faults, extending outward into the eastern foreland limit of the Canadian Cordillera. This regional deformation included a phase of northeasterly directed compression that variably shortened units of the Selwyn basin through extensive faulting and folding.

The southwestern Selwyn basin is truncated by the Tintina fault, a right-lateral strike-slip fault (Fig. 1), and is bounded to the north by the Dawson thrust fault. Restoration of the displacement along the Tintina fault places the Selwyn basin adjacent to the Yukon-Tanana uplands of east-central Alaska (Gabrielse, 1985; Gabrielse et al., 2006).

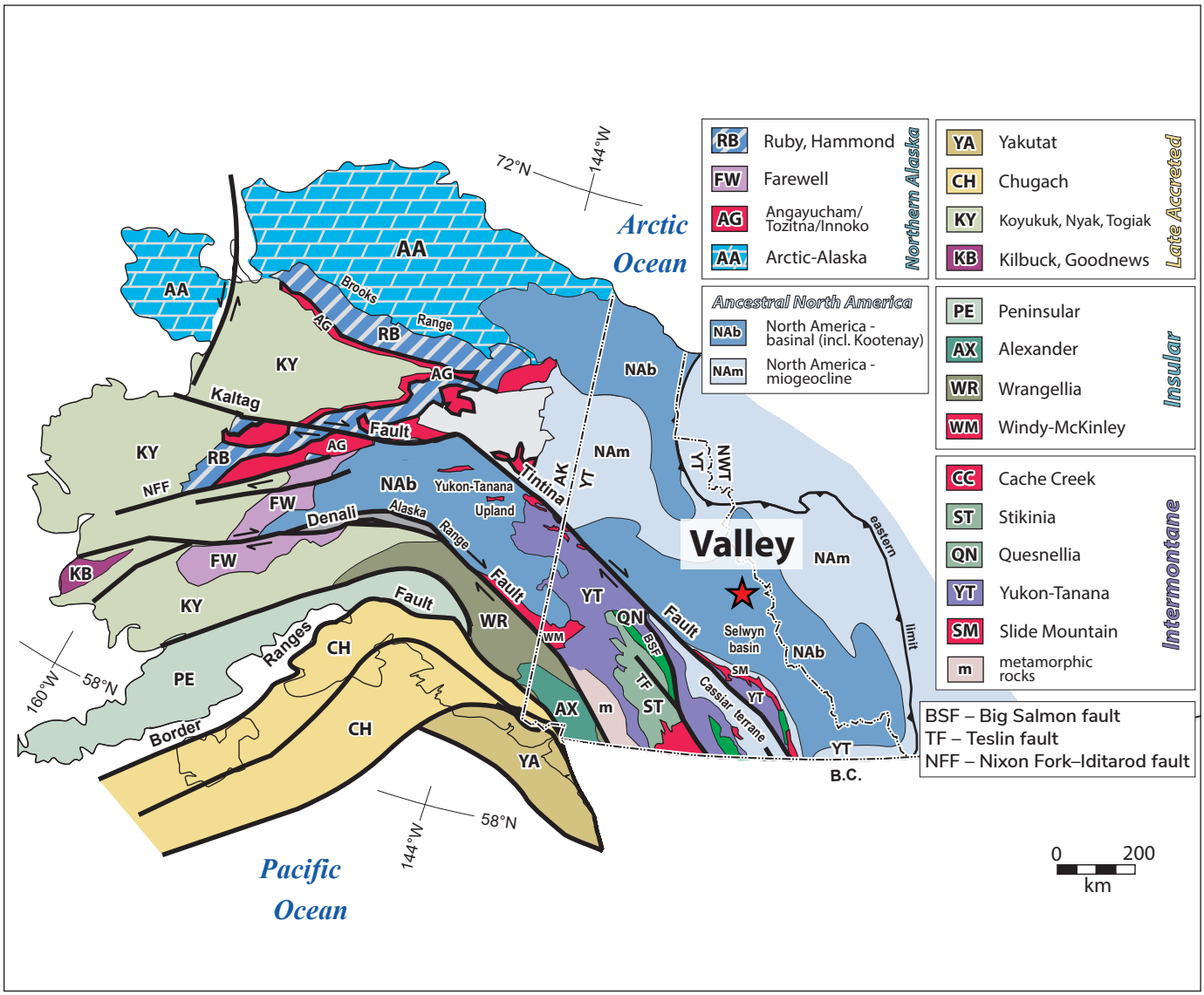

Figure 1. *Tectonic setting of the northwestern Cordillera (after Colpron et al., 2007).*

Figure 2 illustrates the known thrust fault systems in the area, which includes the Selwyn Valley, Hess-Macmillan, Elmer Creek and Arrowhead fault systems. The stratigraphy southwest of the Selwyn Valley thrust fault (northeast of the study area), as well as the Arrowhead and Elmer creek thrust faults, was regionally folded into a large drag fold along the dextral Hess-Macmillan fault system (Fig. 2), which lies just southwest of the Valley deposit.

Regional geology

Numerous plutons, stocks, plugs and associated dikes and sills of the metallogenically favourable Mayo and Tombstone plutonic suites intrude the stratigraphy within the project area. Table 1 lists the regional stratigraphy and intrusions, which will be discussed in the context of the geology below.

Sedimentary units

Lithological units within the Selwyn basin include thick sequences of weakly to moderately metamorphosed mudstone, siltstone and quartz-rich sandstone, interbedded with regionally extensive carbonate, rare carbonate debris flows, and volcaniclastic units (Fig. 3). The basal unit of the Selwyn basin is the Hyland Group, which consists of three major formations, from oldest to youngest: Yusezyu Formation (coarse with lesser fine clastic rocks); Algae Formation (limestone); and

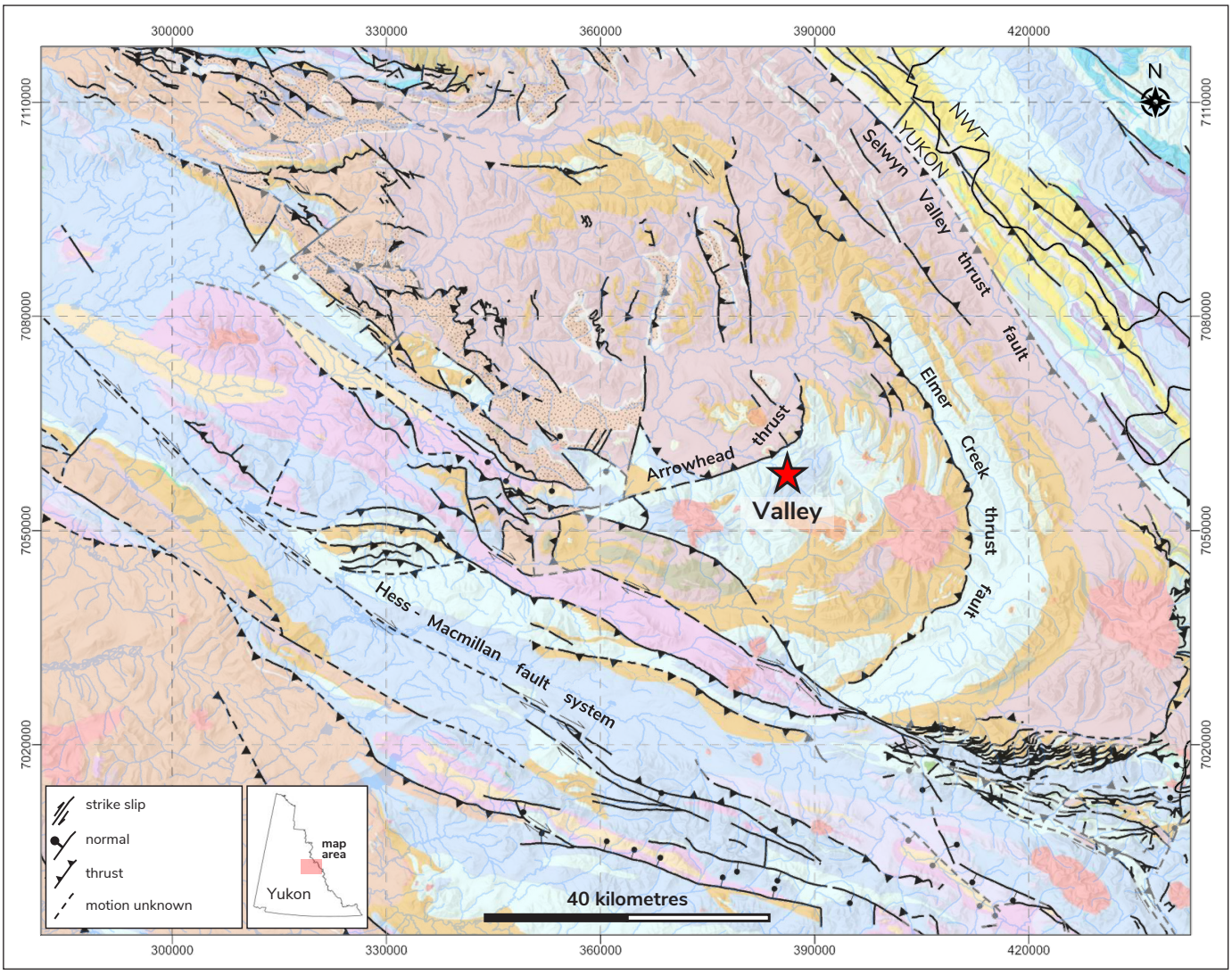

Figure 2. *Regional geology of the Rogue project area (modified from Yukon Geological Survey, 2022).*

Narchilla Formation (primarily fine clastic, including green and maroon shale divided into the Arrowhead Lake and Senoah members).

The Hyland Group is overlain by the Cambrian Gull Lake Formation (fine-grained clastic rocks, minor volcanic and volcaniclastic rocks), which is subsequently overlain by the Ordovician to Silurian Road River Group (black shale, chert and dolomitic siltstone; Fig. 3).

The Devonian to Mississippian Earn Group conformably and locally unconformably overlies the Selwyn basin succession and dominantly consists of black shale, chert and marine conglomerate (Fig. 3). Limited exposures of fine-grained clastic and carbonate rocks of the Carboniferous to Permian Mount Christie Formation are juxtaposed against the older units along faults.

Igneous units

Mid-Cretaceous (115–90 Ma) magmatic rocks are found across the Selwyn basin, and plutons of this age intrude the Neoproterozoic and Paleozoic rocks, as well as younger, overlying stratigraphy. These mid-Cretaceous plutons appear to mostly postdate the dominant, northwest-verging regional deformation, intruding across major structures and exhibiting little internal strain. The most-inboard and youngest of these intrusions form an arcuate belt of plutons, dikes and sills along the northern margin of the basin and are collectively known as the Tombstone-Tungsten belt (Mortensen et al., 2000; Hart et al., 2004). Magmatic rocks within the Tombstone-Tungsten belt are mid-Cretaceous, chemically reduced, and commonly associated with gold and tungsten mineralization

Table 1. *Table of layered and plutonic rocks (after Yukon Geological Survey, 2022).*

Geologic time/Unit name	Unit description
Mid-Cretaceous	
Tombstone plutonic suite	biotite-hornblende clinopyroxene granite (94–90 Ma)
Mayo plutonic suite	biotite granite, K-feldspar porphyry granite; includes quartz monzonite, granodiorite (98–93 Ma)
Mississippian	
Mount Christie Formation	burrowed/interbedded greenish-grey, cherty shale and green shale, chert, shale and siltstone
Devonian to Mississippian	
Earn Group	black shale and chert, chert pebble conglomerate, minor sandstone, minor felsic to intermediate volcanic rocks
Ordovician to Silurian	
Road River Group	
Steel Formation	rusty green to buff argillite, minor black shale and chert, prominent orange-weathering dolostone bed
Elmer Creek Formation	chert and siliceous shale (graphitic and bioturbated in upper part); grey chert and siliceous argillite in lower part, rare limestone
Upper Cambrian	
Old Cabin Formation	basic volcaniclastics, breccias, lapilli tuff, flows, sills, dikes, minor sedimentary units
Lower Cambrian	
Gull Lake Formation	mafic metavolcanic and volcaniclastic rocks, siltstone and argillite
	fine clastic rocks with local basal limestone, limestone conglomerate, with local volcanic and volcaniclastic units (observed at Old Cabin Creek)
Neoproterozoic to Lower Cambrian	
Hyland Group	undifferentiated
Narchilla Formation	dark grey, green and maroon shale; grey and green siltstone to phyllite; minor fine-grained, white, thinly bedded sandstone; minor green-grey sandstone interbedded with siltstone; rare medium-bedded, brown to grey quartz arenite and quartz grit
Arrowhead Lake Member	maroon-weathering, maroon and pale green argillite, minor quartzite, conglomerate, limestone
Algae Formation	limestone ± sandy with local shale, calc-silicate, marble
Yusezyu Formation	primarily maroon and red-weathering argillite and siltstone of Upper Maroon Member; calcareous, brown-weathering sandstone, grey to white-weathering quartzite, minor shale, argillite and grit

(Mortensen et al., 2000; Hart et al., 2004). The Tombstone-Tungsten belt comprises several plutonic suites including the Tombstone, Mayo and Tungsten suites (Hart, 2005). The Tombstone suite (94–90 Ma) is alkalic, variably fractionated, slightly oxidized, contains magnetite and titanite, and has primary, but no xenocrystic zircon (Table 2). The Mayo suite (98–93 Ma) is sub-alkalic, metaluminous to weakly peraluminous, fractionated, but with early felsic and late mafic phases, and moderately reduced with titanite dominant (Table 2). The Tungsten suite (98–96 Ma) is peraluminous, entirely felsic, more highly fractionated, and reduced with ilmenite dominant.

Deposit lithology

The Valley stock is a Mayo suite, multiphase granodiorite intrusion hosted by a series of steeply dipping Silurian to Devonian sedimentary beds of the Steel Formation and Earn Group. The predominant intrusive phase is a coarser grained phase of granodiorite. Distributed throughout the intrusion, and also occurring as dikes intruding the surrounding sedimentary rock package, are a medium-grained granodiorite and a fine-grained porphyritic granodiorite. The following sections detail the different lithologies identified around and within the Valley deposit.

The Steel Formation and Earn Group

The Selwyn basin sedimentary package hosting the Valley stock consists of a series of interbedded siltstone, shale, sandstone, breccia and chert of the Silurian Steel Formation. In the southeast part of the deposit area, 500 m from the known intrusion contact (Fig. 4), the bedding orientation shows a series of beds that dip steeply (>70°) to

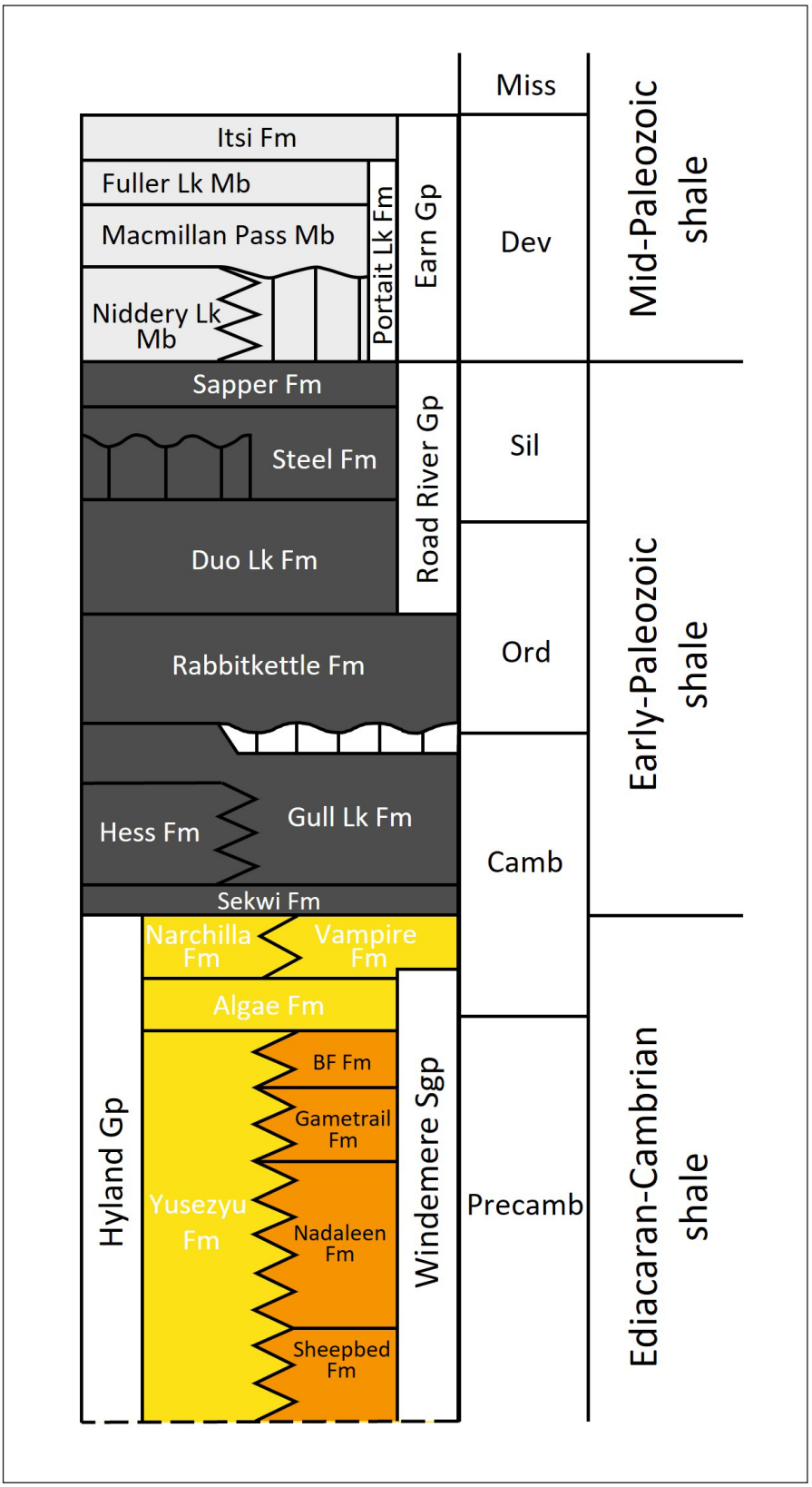

Figure 3. *Simplified stratigraphy of the Selwyn basin (after Sack et al., 2018), including the Windermere Supergroup stratigraphy, which is in the Rackla area. BF: Blueflower.*

Table 2. *Summary of characteristics of the Tombstone and Mayo plutonic suites (after Hart et al., 2004).*

Characteristics	Tombstone suite	Mayo suite
age	94–90 Ma[(1)]	98–93 Ma[(1)]
dominant lithologies	alkali feldspar, syenite to quartz syenite	monzonite to granodiorite
pluton size	moderate	small
plutons	zoned, mafic margins, felsic cores	simple, later mafic phases
grain size	coarse, cumulate	medium to fine grained, locally porphyritic
mafic phases	pyroxene (aegirine-augite)>hornblende >biotite	biotite>hornblende; clinopyroxene common
dominant Fe-Ti indicator minerals	magnetite>titanite	titanite
accessory minerals	epidote, allanite, melanite, apatite, fluorite, zircon	allanite, apatite, zircon
SiO_2 range	50–70%	55–75%
aluminum saturation index (ASI)	metaluminous, except where highly fractionated (0.65–1.1)	metaluminous to weakly peraluminous (0.6–1.15)
alkalinity	alkaline to peralkaline	subalkaline
Fe_2O_3/FeO	0.2–1.1	0.15–0.45
average magnetic susceptibility (x10-3 SI)	1.79	0.11
Cr (ppm)	most <20, some 20–80	most 20–100, some 100–600
inherited zircons	none	some
initial Sr ratio	0.710-0.720	0.7115–0.7140
εNdT	−7 to −9	−8 to −13
oxygen isotopes	9 – 11	11 – 14
zircon saturation temperature (ZST)	820°C	780°C
associated mineralization	Au-Cu-Bi-U-Th-F	Au-Bi-Te, W, As, Ag-Pb
characterization	alkalic, slightly oxidized metaluminous, radiogenic, syenite cumulates	metaluminous, moderately reduced, radiogenic, biotite granodiorite

Note: (1) Dates from Yukon Geological Survey [2023].

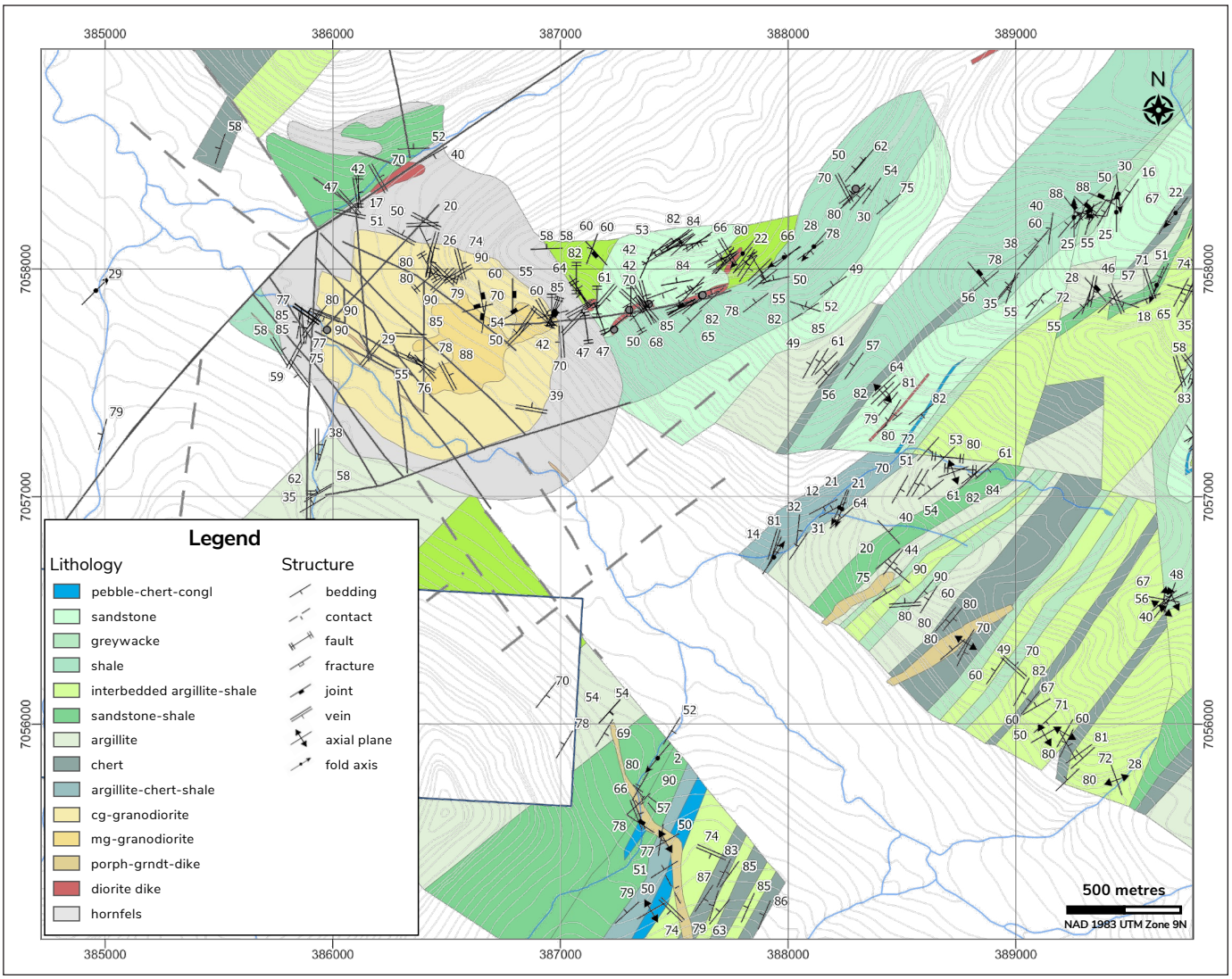

Figure 4. *Local geology of the Valley stock and surrounding sedimentary rocks (from Burrell et al., 2024). cg: coarser grained, congl: conglomerate, grndt: granodiorite, mg: medium grained, porph: porphyry.*

the northwest (220–250°). Bedding measurements adjacent to the intrusion collected from drilling and surface mapping strike roughly parallel to the intrusion contact and dip away from the intrusion. East of the Valley stock, the sedimentary package is more consistent with the siltstone, shales and sandstone observed in the Earn Group, suggesting an unconformity proximal to the Valley stock (Gamonal, 2023).

Thin sections have been collected from the hornfels section of the drill core where primary sedimentary textures are poorly preserved. The quartzite units of the sedimentary package are generally fine grained, and quartz grains are intergrown and subhedral (<1 mm); bedding is defined by changes in quartz grain size. Siltstones are predominantly quartz rich, interbedded with biotite and amphibole-rich layers. Amphibole is replaced by white mica, likely muscovite. The siltstone and shale units often contain disseminated diagenetic pyrite or pyrrhotite (Hamel, 2023).

Intrusive phases

There are two distinct phases to the granodiorite, which are both medium grained in texture; however, one is visibly coarser grained. The coarser grained phase and the finer grained phase are herein referred to as the ‘coarser grained granodiorite’ and the ‘finer

grained granodiorite', respectively. The coarser grained granodiorite is equigranular, and composed of 40% plagioclase (2 mm), 20% quartz (<7.5 mm), 15% K-feldspar (0.5 mm), 10% biotite (0.2 mm), 5% hornblende (0.2 mm) and abundant titanite (<0.5 mm; Hamel, 2023). The 800 by 1100 m intrusion is slightly elongated to the northwest, and is bounded by faults to the northwest and west. The intrusion is open at depth, and based on the drilling conducted to date, the potential for a preferred plunge orientation is currently unknown.

The finer grained granodiorite is located to the east of the coarser grained granoditorite, and has a lateral extension of 300 m. There are also shallow, east-dipping, medium-grained granodiorite dikes throughout the coarser grained phase of the intrusion. The composition of the finer grained granodiorite is very similar to the coarser grained granodiorite, but has a slightly higher quartz content and a grain size range of 0.1–1.5 mm.

A fine-grained porphyritic granodiorite unit is slightly more mafic than the coarser grained granodiorite. It is observed throughout the deposit in the form of dikes, as a minor uniform intrusion, and as an intrusive breccia hosting clasts of coarser grained granodiorite and country rock. The uniform intrusion was identified 250 m below surface, and measures approximately 500 m in length by 150 m in width. The fine-grained porphyritic granodiorite is a later phase of the multi-phase intrusion. The mineralogy consists of a bimodal population of 10–20% phenocrysts and 80–90% groundmass. The phenocrysts are plagioclase and quartz (2 mm) in a groundmass of 50% plagioclase (0.05 mm), 20% K-feldspar (<1 mm), 10% quartz (0.05 mm), 10% biotite (0.05 mm) and 1–2% pyrrhotite (0.2 mm).

Structural setting

Rocks of the Neoproterozoic to Paleozoic Selwyn basin underwent intense deformation during a compression event between the Jurassic and mid-Cretaceous. This episode of deformation caused intense shortening, resulting in tight folding and thrusting that is evidenced by the Arrowhead thrust fault, which is in the vicinity of the Valley deposit (see Fig. 2). This event also caused significant tilting of stratigraphic units producing southeast-dipping and northeast-striking beds, which is the prominent orientation observed. Folding associated with this event is seen to the east of the Valley stock, along a northeast-striking fault that puts black shales of the Earn Group in contact with sandstones and conglomerates of the Road River Group. The axial plane of these faults is controlling northeast-striking dioritic dikes.

Due to the lack of outcrop around the Valley stock, the interpretation of faults is based on geophysical data and downhole drill data. In particular, an unmanned aerial vehicle (UAV) magnetic survey flown over Valley in 2021 identified lineaments that were later confirmed as fault zones. Using these tools, steeply dipping faults oriented northwest, north, west and northeast were interpreted in the Valley deposit area. These faults are characterized by gouge material and have local slickensides, displaying minimal evidence of shear movement. In some cases, these faults are healed by hydrothermal breccias composed of quartz + pyrite cement that support angular fragments of intrusive rock. The north-oriented faults are interpreted as representing the oldest deformation event. The north-oriented faults bound northwest-oriented faults, which controlled the emplacement of the intrusive units and subsequent sheeted veins. West-oriented faults are interpreted as linkage relay structures between subparallel northwest faults. The youngest episode of deformation is represented by northeast-oriented faults such as Arrowhead Pass fault, located to the north and northeast of the Valley deposit. Kinematics of these faults have not been fully interpreted due to the absence of marker horizons and poor rock exposure; however, normal post-mineralization offsets are interpreted from geochemistry due to the zonation of gold-associated pathfinders.

Alteration

Alteration at the Valley deposit can be classified into three distinct alteration facies, each controlled by the underlying lithology. Alteration box plots in Figure 5 illustrate a predominantly fresh intrusion having local alteration trends progressing toward chlorite, sericite and potassium feldspar. Alteration within the Valley stock can be characterized based on either the granodiorite or porphyry intrusive phase. The contact metamorphic aureole is expressed over ~50–100 m from the contact of the Valley stock before transitioning into fresh, unaltered sedimentary rocks.

Intrusion-related alteration

The granodiorite has been altered by weak to strong, pervasive sericite and chlorite alteration assemblages. Argillic alteration is also present; however, it is usually localized within fault structures and fracture zones.

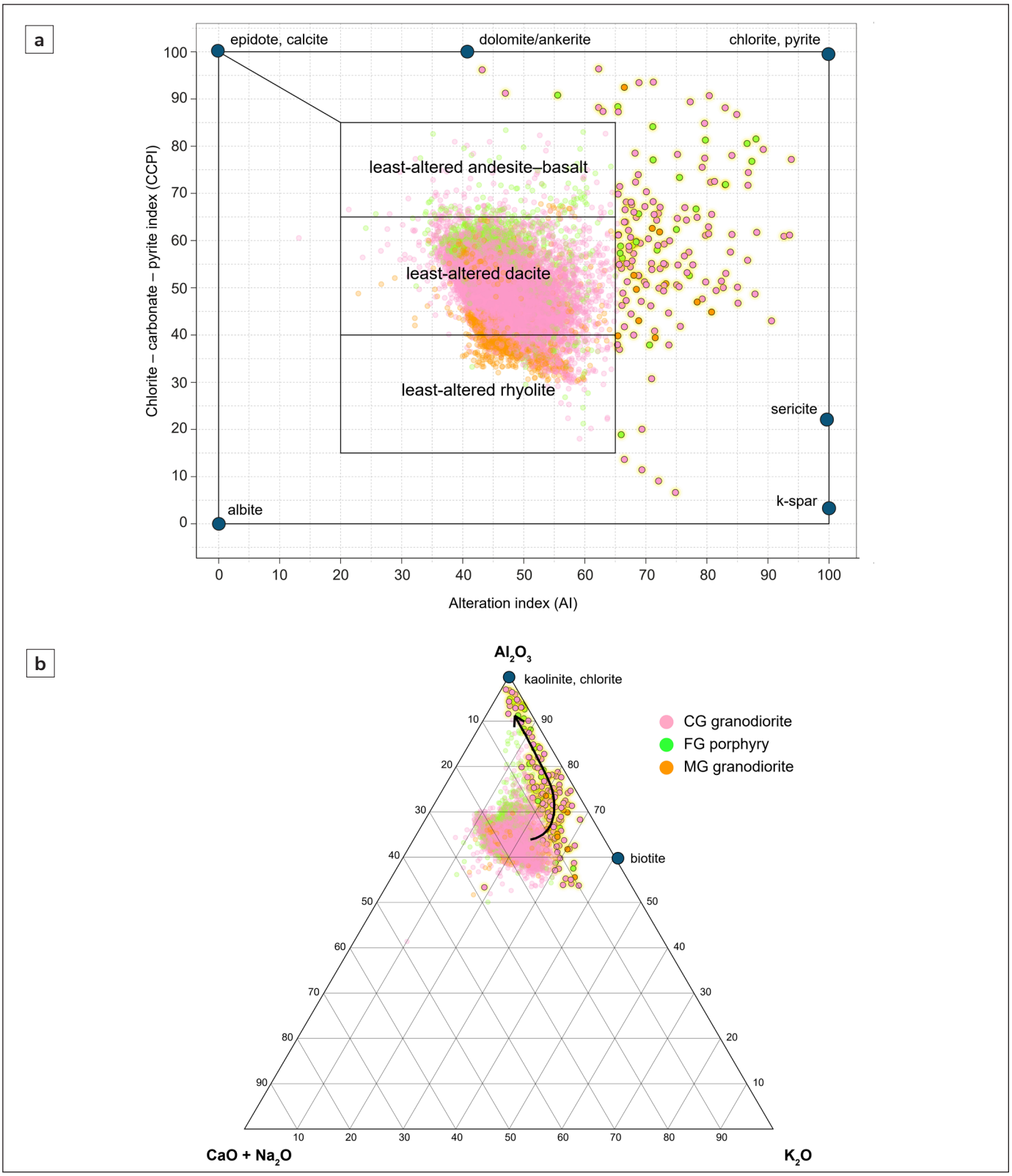

Figure 5. *Alteration box plot and ternary diagram illustrating alteration of different magma phases. The outliers are outlined in both charts.* ***(a)*** *Box plot of the three intrusive units displaying a dominant fresh rock with alteration toward chlorite, sericite and K-feldspar.* ***(b)*** *Ternary diagram illustrating a trend toward chlorite and kaolinite. CG: coarse grained, FG: fine grained, MG: medium grained*

Sericite is observed completely replacing medium-grained, subhedral crystals of plagioclase in the groundmass and as phenocrysts. Chlorite and rutile replace subhedral primary biotite and hornblende. Primary, dark brown titanium-hornblende averaging 1 mm in size displays deuteric alteration with a biotite rim and simple twinning. Anhedral, fine-grained, dark brown hydrothermal biotite is more common around alteration haloes (Hamel, 2023).

The predominant alteration assemblage in the fine-grained porphyritic granodiorite is biotite and chlorite. Both are observed replacing mafic minerals. Weak to moderate secondary biotite developed as anhedral grains in the groundmass of the fine-grained porphyritic phase. Minor intervals of argillic alteration are associated with faults and fracture structures. Moderate sericitic alteration is observed along the contact between the finer grained and coarser grained granodiorite.

Hornfelsing around the Valley stock of the interbedded, sedimentary country rock resulted in an alternating sequence of silica and biotite replacement with minor sericite. Fine-grained quartz replacement is predominantly observed in sandstone units, whereas biotite and sericite replacement is more common in siltstones and mudstones. A spatial zonation is observed, and silica replacement was mainly noted along the northwestern margin. Biotite and sericite become increasingly predominant toward the central and southern margins of the intrusion.

Several granodioritic dikes crosscut the hornfelsed sedimentary rocks and exhibit varying degrees of alteration. The dikes are commonly altered to chlorite and sericite, and have a clear spatial relationship to the intrusion. Sericite alteration is typically observed proximal to the intrusion, whereas chlorite alteration is more distal.

Vein selvage

The dominant vein assemblage hosted in the Valley stock consists of quartz-carbonate veins. These veins are characterized by an envelope of moderate to strong vein halos of sericite and chlorite alteration, and relicts of an early event of potassic alteration represented by K-feldspar. The vein envelopes vary in thickness; most measure between 2 and 5 cm, but some can be up to 10 cm. Alteration intensity is strongest in the north-central part of the intrusion, and gradually weakens toward the south. Vertically, the alteration is most pronounced from the surface down to approximately 250 m, and is particularly intense along the contact between the intrusion and the surrounding hornfels.

Mineralization

Gold mineralization within the Valley deposit is almost entirely hosted in quartz-carbonate veins; however, a few instances of visible gold are observed in vein selvages. The mineralization envelope with gold grades >1 g/t Au is consistent and continuous, and is characterized by intense sheeted veins. The mineralization envelope has an approximate volume that extends over 700 m in length, 400 m in width and 400 m in depth.

Veins

Gold mineralization is hosted in quartz-carbonate veins. There are several vein types in the Valley stock that are identified by vein assemblage (Table 3); however, not all of these host significant gold mineralization. The mineralized quartz-carbonate veins are generally narrow (0.2–2 cm), planar and crystalline, and have mineral growth that ranges from euhedral to subhedral. Vein density in the high grade (>2 g/t Au) core of the deposit is generally >15 veins per metre and decreases gradually to <5 veins per metre in the distal, low-grade (<0.4 g/t Au) zones of the intrusion. Mineralization is generally confined to the intrusive units; however, in the northwest part of the deposit, hornfelsed sedimentary rocks host moderate mineralization where they are in contact with a series of dikes.

The predominant orientation of the sheeted gold-bearing veins strikes northwest (320°) and has a consistent steep dip (80°). However, there is a spread of vein orientations ranging from north to west (dipping to the northeast), and south to east (dipping to the southwest; Fig. 6). The high-grade mineralized core of the deposit is associated with the interaction of multiple vein orientations. Northwest and north-striking vein orientations also correspond with the orientations of the two dominant fault trends within the deposit, having implications for the timing of deformation and mineralization relative to the intrusion.

Mineral assemblages

Gangue minerals within the mineralized veins include quartz, calcite, K-feldspar (often resembling plagioclase due to the reduced nature of the deposit), adularia and minor scheelite. Sulphide mineralization within the veins is low, generally <10% of the vein content, and consists

Table 3. *Summary of vein assemblages identified by diamond drilling in the Valley target area.*

Mineralogy	Location	Orientation style	Morphology
quartz-carbonate-arsenopyrite-galena	northwest margin and interior of the intrusion	strong northwest spread, steeply dipping	singular, planar (<1 cm)
arsenopyrite	northeast part of the intrusion	flat lying	singular, planar (<1 cm)
quartz-chlorite	consistent distribution	northwest, flat and east-striking	singular, planar or irregular (0.1–2 cm)
chlorite-pyrrhotite	consistent distribution	northwest, north and west-striking, steeply dipping	singular, planar or irregular (<0.5 cm)
quartz	consistent distribution	variable	variable
quartz-carbonate	consistent distribution	strike spread north to west, steeply dipping	sheeted, planar (0.1–2 cm)

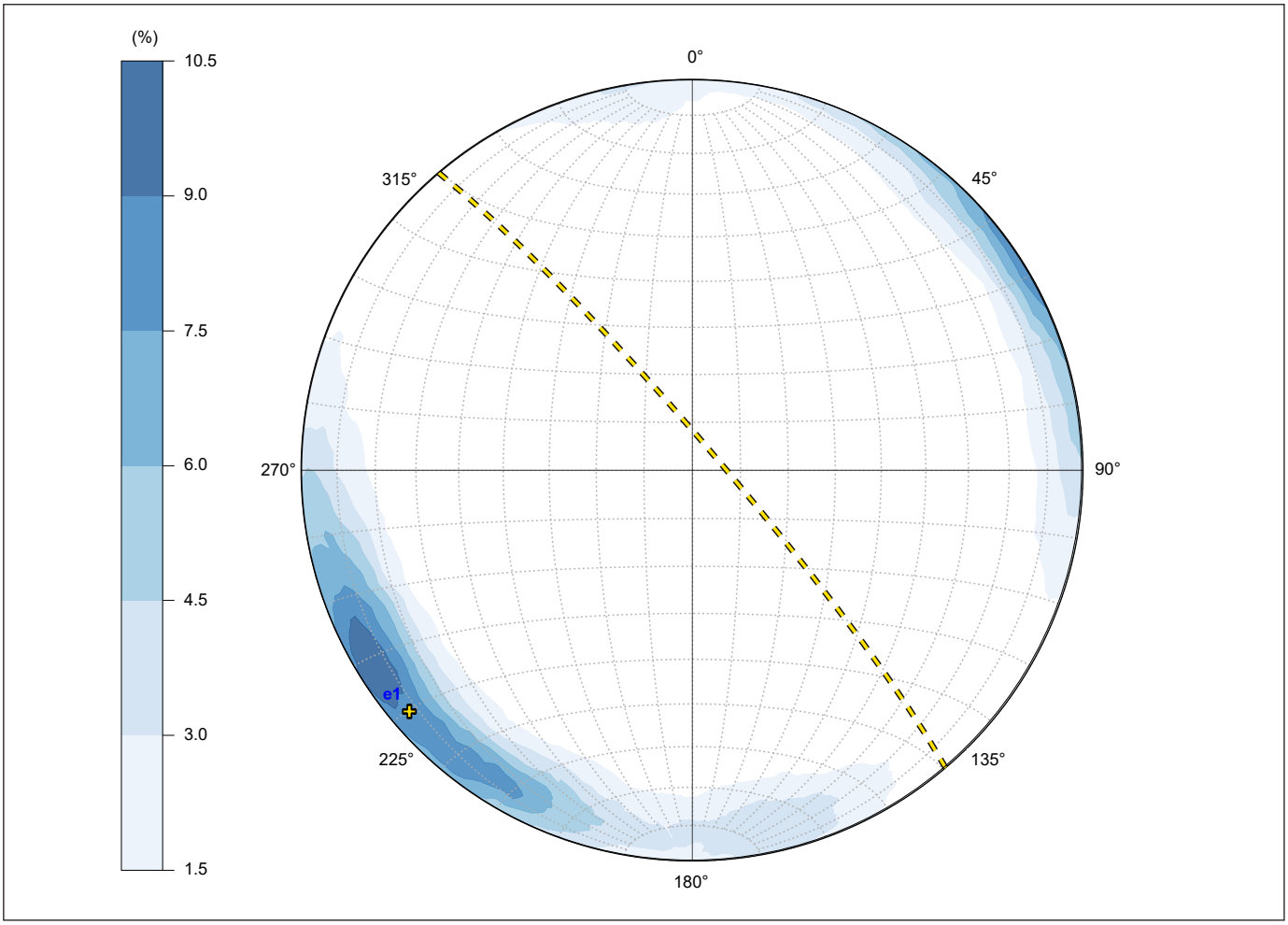

Figure 6. *Stereonet of the quartz-carbonate vein orientations with a heat map showing the spread of poles to planes. Yellow dashed line is the average plane of the veins, and the yellow cross is the average pole to the plane.*

of scheelite (1%), pyrrhotite (2%), chalcopyrite (0.3%), pyrite (0.3%), arsenopyrite (0.3%), molybdenite (0.1%) and marcasite (0.1%), as well as variable lead-bismuth-tellurium sulphides (0.1%; Hamel, 2023). Common lead-bismuth-tellurium sulphides include, bismuthinite (Bi_2S_3), lillianite ($Pb_3Bi_2S_6$), baksanite ($Bi_6Te_2S_3$), hedleyite (Bi_7Te_3), and tetradymite (Bi_2Te_2S; Fig. 7; Hamel, 2023). Arsenopyrite ± galena ± stibnite veins are also present within the Valley stock (Table 3); however, these postdate mineralization and are not interpreted to be associated with the main mineralization event.

Gold in the Valley stock is found as native particles, and has a purity up to 96.84 wt.% (Hamel, 2023). Gold commonly occurs adjacent to, or within lead-bismuth-tellurium sulphide minerals. It is also observed as free gold within the quartz veins and adjacent to other sulphides such as pyrrhotite. Element correlations using all drill data at Valley prior to 2024 demonstrates tellurium (R^2=0.86) and bismuth (R^2=0.71) and to a lesser extent, tungsten (R^2=0.43) and lead (R^2=0.25) having the strongest association with gold. Additionally, antimony, arsenic and silver are also present in the deposit and are useful pathfinders as they form a broad halo around the intrusion but are not directly associated with gold mineralization (Fig. 8).

Resource

The initial mineral resource estimate (MRE) for the Valley deposit was published in June 2024 and was completed using 27 911 m of diamond drill data collected between 2021 and 2023. Based on a preliminary pit optimization, a pit shell with a 0.72 revenue factor contains an Indicated Mineral Resource of 76 Mt at 1.66 g/t Au for 4.05 Moz Au in addition to an Inferred Mineral Resource of 81 Mt at 1.25 g/t Au for 3.26 Moz Au using a cut-off grade of 0.4 g/t Au (Table 4).

Valley drill core in Yukon Geological Survey collection

Diamond drill core from holes V-22-012 and V-23-047 (Figs. 9, 10 and 11) within the Valley deposit area have been donated to Yukon Geological Survey by Snowline Gold Corp. Hole V-22-012 is from the eastern part of the deposit, collaring in the medium-grained intrusive unit, and intersecting the coarser grained granodiorite. This drillhole is predominantly within the low grade (0.1–0.4 g/t Au) part of the initial MRE. Located in the core of the deposit,

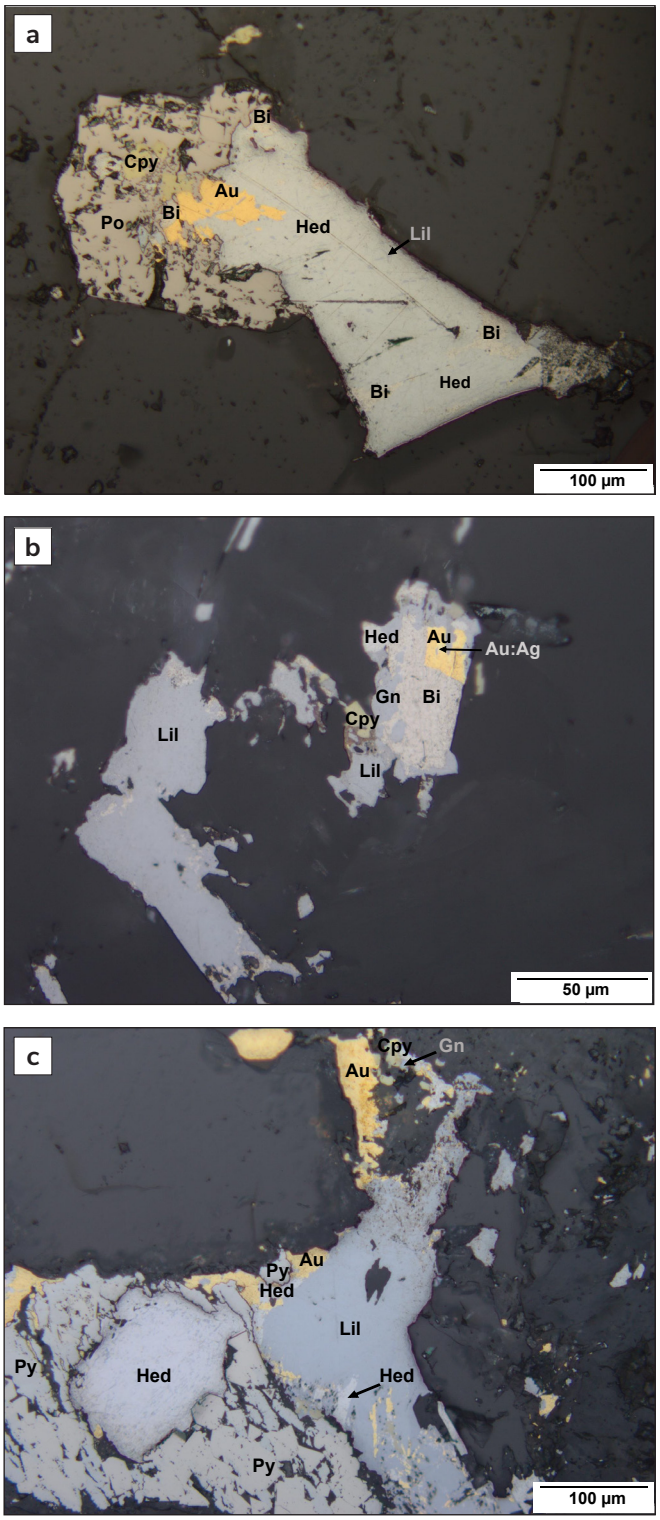

Figure 7. *Reflected light photomicrographs of gold occurrences with associated Pb-Bi-Te-sulphides from quartz-carbonate veins (Hamel, 2023). Figures* ***(a)*** *to* ***(c)****: Au: gold, Bi: bismuth, Cpy: chalcopyrite, Gn: galena, Hed: hedleyite, Lil: lillianite, Po: pyrrhotite, Py: pyrite. Figure* ***(b)*** *Au:Ag: gold with silver (1:4 ratio).*

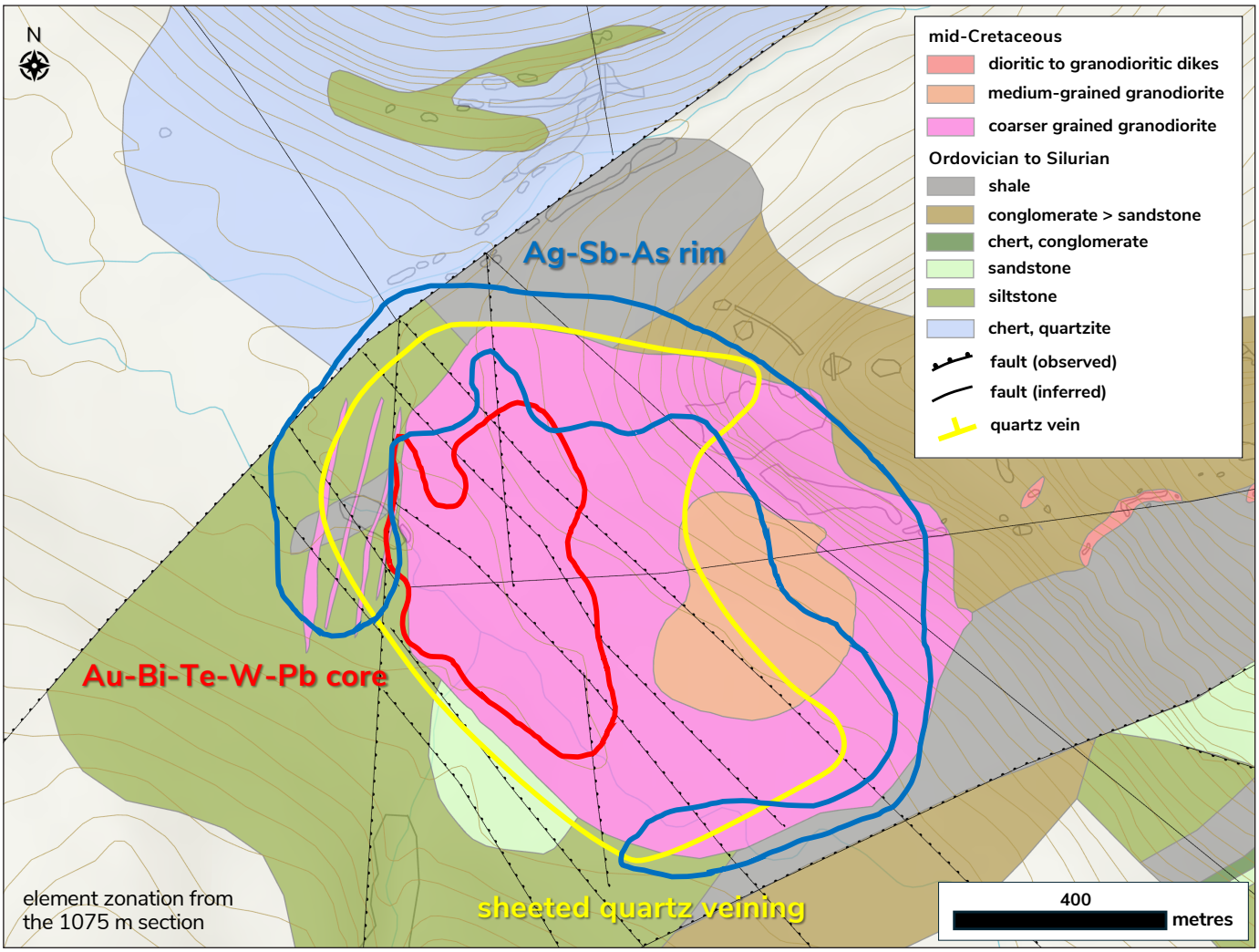

Figure 8. *Zonation of pathfinder elements of the Valley deposit. The 1075 m elevation is approximately 100 m below the surface. Au: gold, Bi: bismuth, Te: tellurium, W: tungsten, Pb: lead, Ag: silver, Sb: antimony, As: arsenic.*

Table 4. *Valley deposit mineral resource summary showing entire resource estimation as published in the NI 43-101 technical report released in June 2024 and based on a cut-off grade of 0.4 g/t Au (Burrell et al., 2024).*

Mineral resource category	Tonnage (t × 1000)	Grade (Au g/t)	Contained gold (ounces × 1000)
Indicated Resource	75 836	1.66	4052
Inferred Resource	81 039	1.25	3260
Waste material	140 124		

hole V-23-047 is collared in the high-grade (>2 g/t Au), northwest side of the intrusion. The drillhole begins in strong mineralization hosted within the coarser grained granodiorite until intersecting the hornfels where the grade abruptly decreases to <0.1 g/t Au. Both drillholes are examples of typical Valley deposit mineralization where gold is hosted within quartz-carbonate veins. Vein density and lead-bismuth-tellurium mineralization are strong controlling factors on the gold grades.

Interpretation

The Valley stock is part of a post-collisional, mid-Cretaceous magmatic event that constitutes the youngest rocks observed in the eastern Selwyn basin, exemplified by multiple stocks, plutons and dikes belonging to the Mayo, Tombstone and Tungsten suites.

The style of gold mineralization observed in the Valley deposit indicates a magmatic-hydrothermal system where intense fracturing associated with the

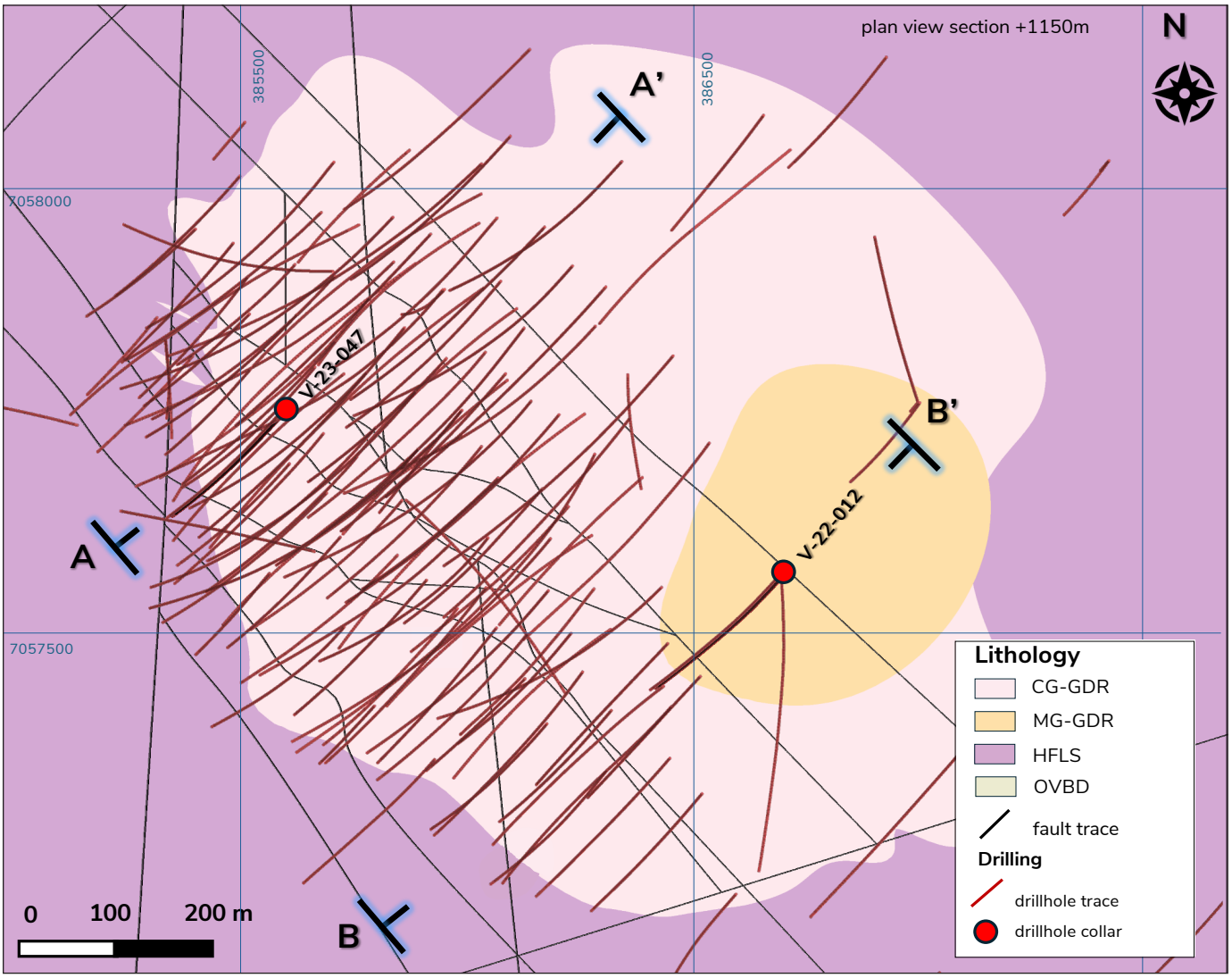

Figure 9. *Plan view map on the 1150 m elevation section illustrating drill trace locations for V-22-012 and V-23-047. CG-GDR: coarser grained granodiorite, MG-GDR: medium-grained granodiorite, HFLS: hornfels, OVBD: overburden.*

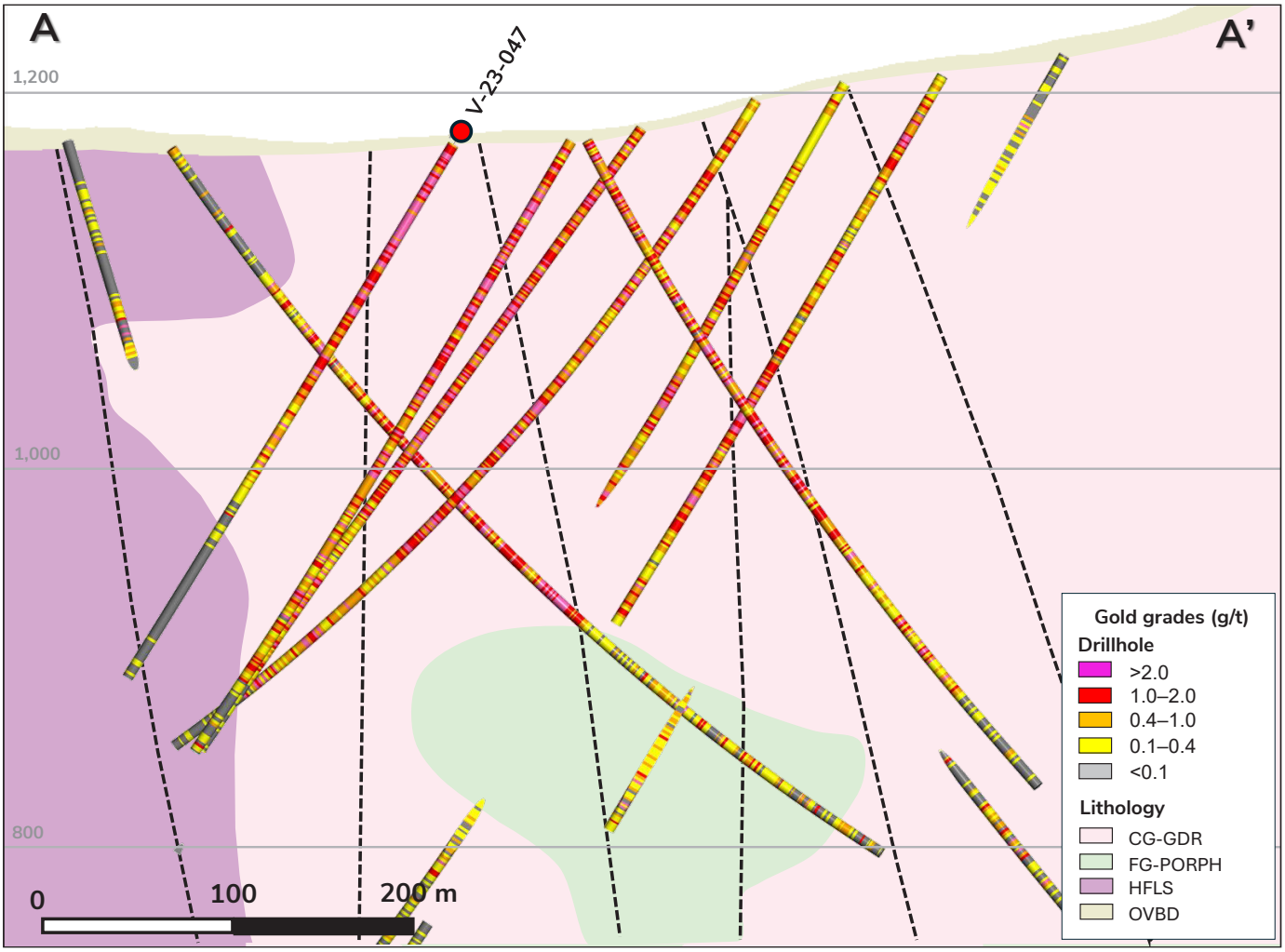

Figure 10. *Cross section (50 m width) displaying V-23-047 and surrounding drilling including gold grades along the drill traces. CG-GDR: coarser grained granodiorite, FG-PORPH: fine-grained porphyry, HFLS: hornfels, OVBD: overburden.*

cooling of the upper part of the Valley stock, allowed for the formation of quartz-carbonate veins and the precipitation of gold-bearing hydrothermal fluids with bismuth-tellurium sulphides acting as collectors of gold particles within the veins. Based on the metallogenic characteristics, pathfinder element associations, and gold mineralization hosted within an ilmenite-dominant reduced intrusion, the Valley deposit is classified as a reduced intrusion-related gold system, similar to other deposits within the Tombstone-Tungsten belt such as Fort Knox and Dublin Gulch.

Conclusions

The discovery of the Valley deposit has opened a new frontier in the eastern segment of the Tombstone gold belt, previously considered less prospective compared to the western segment of the belt, which host systems such as Dublin Gulch and Brewery Creek. Ongoing exploration of the Valley deposit aims to improve our knowledge of the orebody and this world-class system.

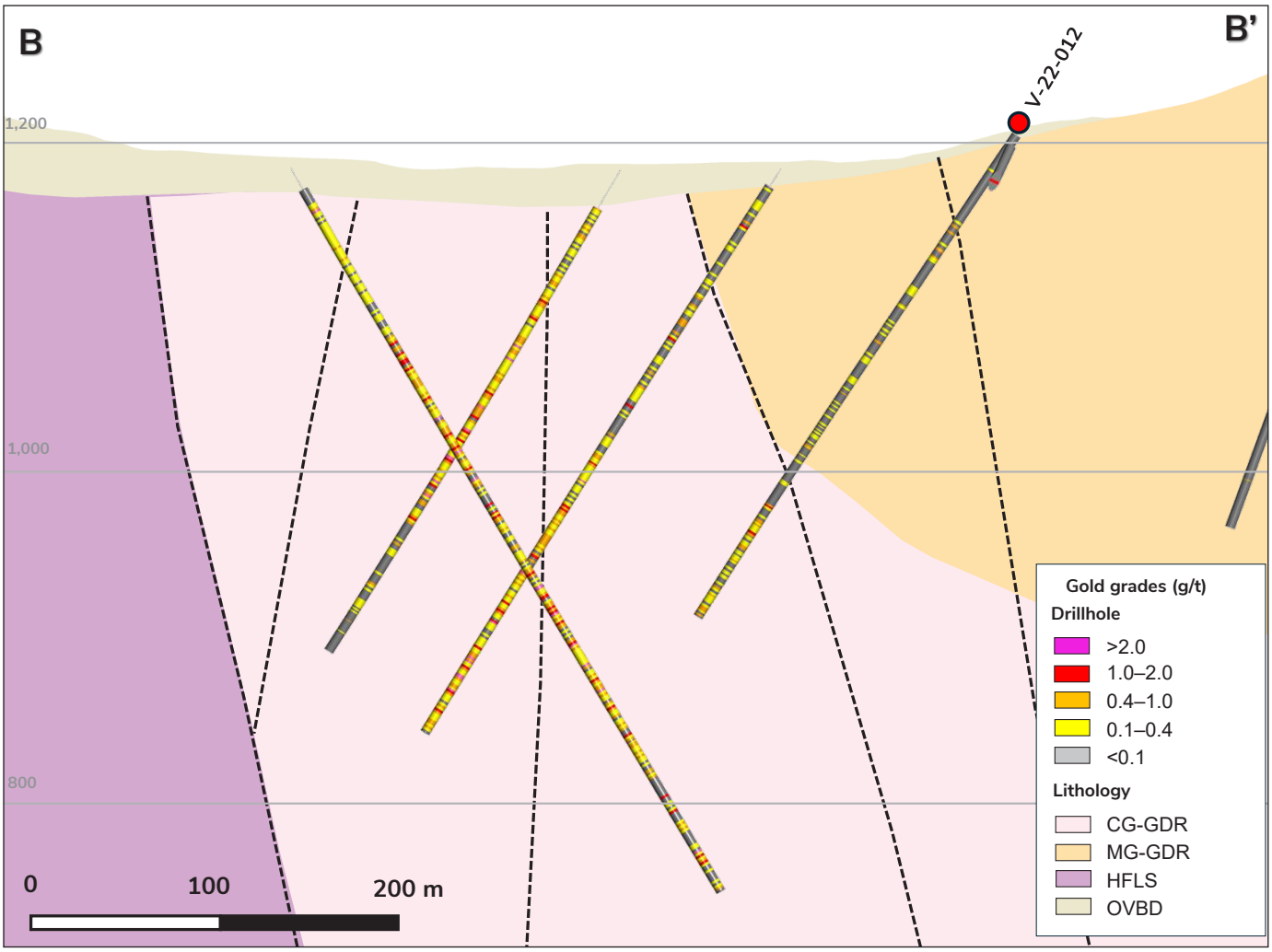

Figure 11. *Cross section (50 m width) displaying V-22-012 and surrounding drilling including gold grades along the drill traces. CG-GDR: coarser grained granodiorite, MG-GDR: medium-grained granodiorite, HFLS: hornfels, OVBD: overburden.*

Acknowledgments

Snowline would like to acknowledge the technical and operational team that has made all this work possible, along with the numerous contractors that have supported the delineation of the Valley deposit.

References

Burrell, H., Haggarty, S. and Redmond, D., 2024. Rogue Gold Project - NI 43-101 Technical Report and Mineral Resource Estimate, Yukon Territory, Canada. Prepared by Ausenco Engineering Canada ULC for Snowline Gold Corp., submitted July 23, 2024, 200 p. https://snowlinegold.com/wp-content/uploads/2024/07/Snowline-MRE-Technical-Report-Final-1.1.pdf

Colpron, M. and Nelson, J.L., 2011. A digital atlas of terranes for the Northern Cordillera. Yukon Geological Survey and British Columbia Ministry of Energy and Mines, BCGS GeoFile 2011-11. https://data.geology.gov.yk.ca/Reference/95879

Colpron, M., Nelson, J.L. and Murphy, D.C., 2007. Northern Cordilleran terranes and their interactions through time. GSA Today, vol. 17, no. 4/5, p. 4-10.

Gabrielse, H., 1985. Major dextral transcurrent displacements along the Northern Rocky Mountain Trench and related lineaments in north-central British Columbia. Geological Society of America Bulletin, vol. 96, no. 1, p. 1–14.

Gabrielse, H., Murphy, D.C. and Mortensen, J.K., 2006. Cretaceous and Cenozoic dextral orogen-parallel displacements, magmatism, and paleogeography, north-central Canadian Cordillera. *In:* Paleogeography of the North American Cordillera: Evidence for and against large-scale displacements, J.W. Haggart, R.J. Enkin and J.W.H. Monger, eds., Geological Association of Canada, Special Paper 46, p. 255–276.

Hamel, L., 2003. The Valley discovery: a new reduced intrusion-related gold system hosted in the Tintina Gold Province, eastern Yukon, Canada. Unpublished BSc thesis, University of Ottawa, Ottawa, ON.

Hart, C.J.R., 2005. Mid-Cretaceous magmatic evolution and intrusion-related metallogeny of the Tintina gold province, Yukon and Alaska. Unpublished PhD thesis, University of Western Australia, 198 p.

Hart, C.J.R, Mair, J.L, Goldfarb, R.J. and Groves, D.I., 2004. Source and redox controls on metallogenic variations in intrusion-related ore systems, Tombstone-Tungsten Belt, Yukon Territory, Canada. Earth and Environmental Transactions of the Royal Society of Edinburgh, vol. 95, p. 339–356.

Lueck, B.A., 1997. Geological and geochemical assessment report for the LM1-LM18 and APC1-APC24 Claims. Yukon Gold Corp. Yukon Energy, Mines and Resources Assessment Report 93695, 19 pages plus appendices.

Mortensen, J.K., Hart, C.J.R., Murphy, D.C. and Heffernan, S., 2000. Temporal evolution of Early and mid-Cretaceous magmatism in the Tintina gold belt. British Columbia and Yukon Chamber of Mines Cordilleran Roundup, Special Volume 2, p. 49–58.

Nelson, J.L., Colpron, M. and Israel, S., 2013. The Cordillera of British Columbia, Yukon, and Alaska: Tectonics and metallogeny. *In:* Tectonics, Metallogeny and Discovery: The North American Cordillera and Similar Accretionary Settings, M. Colpron, T. Bissig, B.G. Rusk and J.F.H. Thompson (eds.), Society of Economic Geologists Inc., Special Publication 17, p. 53–109.

Sack, P.J., Large, R.R. and Gregory, D.D., 2018. Geochemistry of shale and sedimentary pyrite as a proxy for gold fertility in the Selwyn basin area, Yukon. Mineralium Deposita, vol. 53, p. 997–1018.

Yukon Geological Survey, 2022. Yukon digital bedrock geology. Yukon Geological Survey, https://data.geology.gov.yk.ca/Compilation/3 [accessed 2024-12-01].

Yukon Geological Survey, 2023. Yukon Geochronology–A database of Yukon isotopic age determinations. Yukon Geological Survey, https://data.geology.gov.yk.ca/Compilation/22 [accessed 2024-12-01].

Geology and mineralization of the AurMac metasediment-hosted gold deposits, central Yukon (NTS 105M/13)

R. Keagan Parry and Pilar Lecumberri-Sanchez*
Earth and Atmospheric Sciences, University of Alberta

Patrick Sack
Yukon Geological Survey

Parry, R.K., Lecumberri-Sanchez, P. and Sack, P., 2025. Geology and mineralization of the AurMac metasediment-hosted gold deposits, central Yukon (NTS 105M/13). *In*: Yukon Exploration and Geology Technical Papers 2024, L.H. Weston, A. Stuart, S.K. Schultz, A.D. Brubacher and D.C. Cronmiller (eds.), Yukon Geological Survey, p. 19–39.

Abstract

The AurMac property, located 35 km north of Mayo in central Yukon, includes two metasedimentary rock-hosted gold deposits: the 6158 koz Au Powerline deposit and the 845 koz Au Airstrip deposit. Mineralization at the Powerline and Airstrip deposits is characterized by gold in sheeted quartz veins and mineralized skarn horizons, respectively. The AurMac deposits straddle the Robert Service thrust fault whereby the Powerline deposit is hosted in the Late Proterozoic to Cambrian Hyland Group hanging wall, and the Airstrip deposit is hosted in the Mississippian Sourdough Hill Member of the Keno Hill Quartzite footwall. Host rocks comprise siliciclastic metasedimentary rocks, variably calc-silicate–altered calcareous metasedimentary rocks and magmatic rocks. Magmatic rocks in the Powerline zone consist of foliated mafic horizons that are geochemically similar to Cambro-Ordovician magmatic rocks found in Hyland Group metasedimentary rocks in the McQuesten, Mayo, Clark Lakes and Hart River map areas. In the Airstrip zone, magmatic rocks include a steeply south-dipping, unfoliated, aplite dike. Evidence for intrusion-related gold mineralization at AurMac includes sheeted vein and skarn mineralization similar to the intrusion-hosted, intrusion-related gold deposits at Dublin Gulch, as well as the presence of metamorphic porphyroblast assemblages that suggest contact metamorphism. These findings suggest potential for further discovery of mineralized intrusion-hosted zones on the AurMac property and sediment-hosted, intrusion-related gold deposits elsewhere in the region.

Plain language summary

The AurMac project, located 35 km north of Mayo in central Yukon, includes two gold deposits: the Powerline and Airstrip deposits. The Powerline deposit is estimated to contain over six million ounces of gold, and the Airstrip deposit contains nearly one million ounces of gold. Mineralization in the Powerline deposit is found in quartz-rich veins, whereas gold at the Airstrip deposit is found in a type of metamorphic rock known as skarn. The Powerline deposit is hosted in rocks that are approximately 500 million years old, and the Airstrip deposit is hosted in rocks that are approximately 350 million years old. A large fault, known as the Robert Service thrust, separates the two deposits. The mineralization at the AurMac deposits have some similarities to the mineralization that is found in the deposits of the Eagle Gold Mine in central Yukon and suggests the potential for another significant economic deposit of the same style.

* rkparry@ualberta.ca

Introduction

The AurMac property, located in the McQuesten River area of central Yukon (Fig. 1), is situated equidistant between the recently producing Eagle Gold Mine (>5 Moz Au global resource; Harvey et al., 2023) and the currently producing Keno Hill district (>230 Moz Ag global production; Fig. 2; Blais et al., 2024). Two gold deposits have been defined on the property: the Airstrip deposit, containing 845 koz Au at 0.75 g/t Au hosted primarily in skarn horizons, and the Powerline deposit, containing 6158 koz Au at 0.61 g/t Au hosted primarily in sheeted quartz veins (Fig. 3; Thornton et al., 2024). The AurMac deposits are hypothesized to be part of a reduced intrusion-related gold system (RIRGS), similar to the model described for the nearby Dublin Gulch property (e.g., Hart, 2007). However, a key distinction to existing RIRGS models is that rather than gold being hosted within the carapace and surrounding hornfels of an intrusion, gold at AurMac is solely hosted in metasedimentary rocks and a causative intrusion has yet to be identified.

In this contribution, we review an updated and expanded geological context and characterization of mineralization styles of the AurMac deposits based on detailed relogging of drill core, petrography and whole-rock geochemical analyses. A correlation of lithological units observed at the AurMac deposits is made with map units from the nearby Keno Hill district, providing a southwest extension of Keno Hill district map units to the AurMac property. Resolution of the bedrock geology concludes that sheeted quartz vein mineralization observed in the Powerline deposit is hosted in Late Proterozoic to Cambrian Hyland Group metasedimentary rocks, and skarn-hosted mineralization found in the Airstrip deposit is hosted in the Mississippian to Permian(?) Keno Hill Quartzite. Evidence supporting intrusion-related mineralization is also presented, and includes the presence of contact metamorphism-related porphyroblast assemblages and mineralization styles analogous to those found at intrusion-hosted gold deposits.

Regional geology and structural setting

Stratigraphy

The AurMac property is hosted within slope and basinal Laurentian margin strata of the Selwyn basin (Fig. 1), which covers and area approximately 700 by 200 km in central and eastern Yukon. It is characterized by Neoproterozoic to Middle Devonian slope-to-basin facies strata, related to Neoproterozoic and younger rifting along the North American margin (Gordey and Anderson, 1993; Colpron et al., 2002). The Selwyn basin is bordered by the Mackenzie platform to the north, and the strike-slip Tintina fault to southwest, which mostly separates it from the Yukon-Tanana terrane (Gabrielse et al., 2006). Rocks at the AurMac property consist of Late Proterozoic to Cambrian Hyland Group metasedimentary rocks, and the Mississippian to Permian(?) Keno Hill Quartzite (Murphy, 1997; Read et al., 2020; Figs. 2 and 3).

Foliated mafic rocks within the Hyland Group have been mapped in the northern McQuesten and Mayo map areas (Murphy, 1997). These include fine to medium-grained quartz-feldspar-chlorite-biotite sills and dikes, and foliated, discontinuous and foliation-conformable plagioclase-actinolite-biotite-chlorite meta-igneous rocks (Murphy, 1997). Mafic rocks, interpreted to be analogous to those mapped by Murphy (1997), were also mapped by Abbott (1997) in the Upper Hart River area and have yielded a Cambrian U-Pb age from baddeleyite of 518.2 ± 2.9 Ma.

Sills of the Late Triassic Galena suite intrude the Keno Hill Quartzite and the underlying Earn Group, and are massive to foliated depending on their thicknesses, which can vary from less than 1 m to more than 100 m (Murphy, 1997; Read et al., 2020). Mineralogical variation is observed to be width dependent, where thinner foliated sills are composed of chlorite-actinolite-epidote (zoisite)-albite ± stipnomelane, and wider sills with massive cores range from medium-grained metadiorite and metagabbro, to plagiophyric and/or hornblende-phyric variants (McOnie, 2016). A late Middle Triassic U-Pb age from baddeleyite of 232.2 +1.5/–1.2 Ma was obtained from a Galena Suite gabbro in the Tombstone Range (Mortenson and Thompson, 1990).

Undeformed intrusions

Mid-Cretaceous intrusions of the Mayo suite (98–95 Ma; Rasmussen, 2013), as described by Hart et al. (2004), intrude metasedimentary rocks of the Hyland and Earn groups. The Mayo suite consists of metaluminous felsic to mafic plutons dominated by porphyritic quartz monzonite and are often cut by porphyritic, aplitic or pegmatitic felsic dikes and lamprophyre dikes. The Mayo suite is associated with gold mineralization such as the Eagle deposit (4.3 Moz Au [Measured and Inferred]; Harvey et al., 2023), which is hosted within the Mayo suite Dublin Gulch stock. A published U-Pb age from zircon of 94.1 ± 0.3 Ma (Yukon Geological Survey, 2023a)

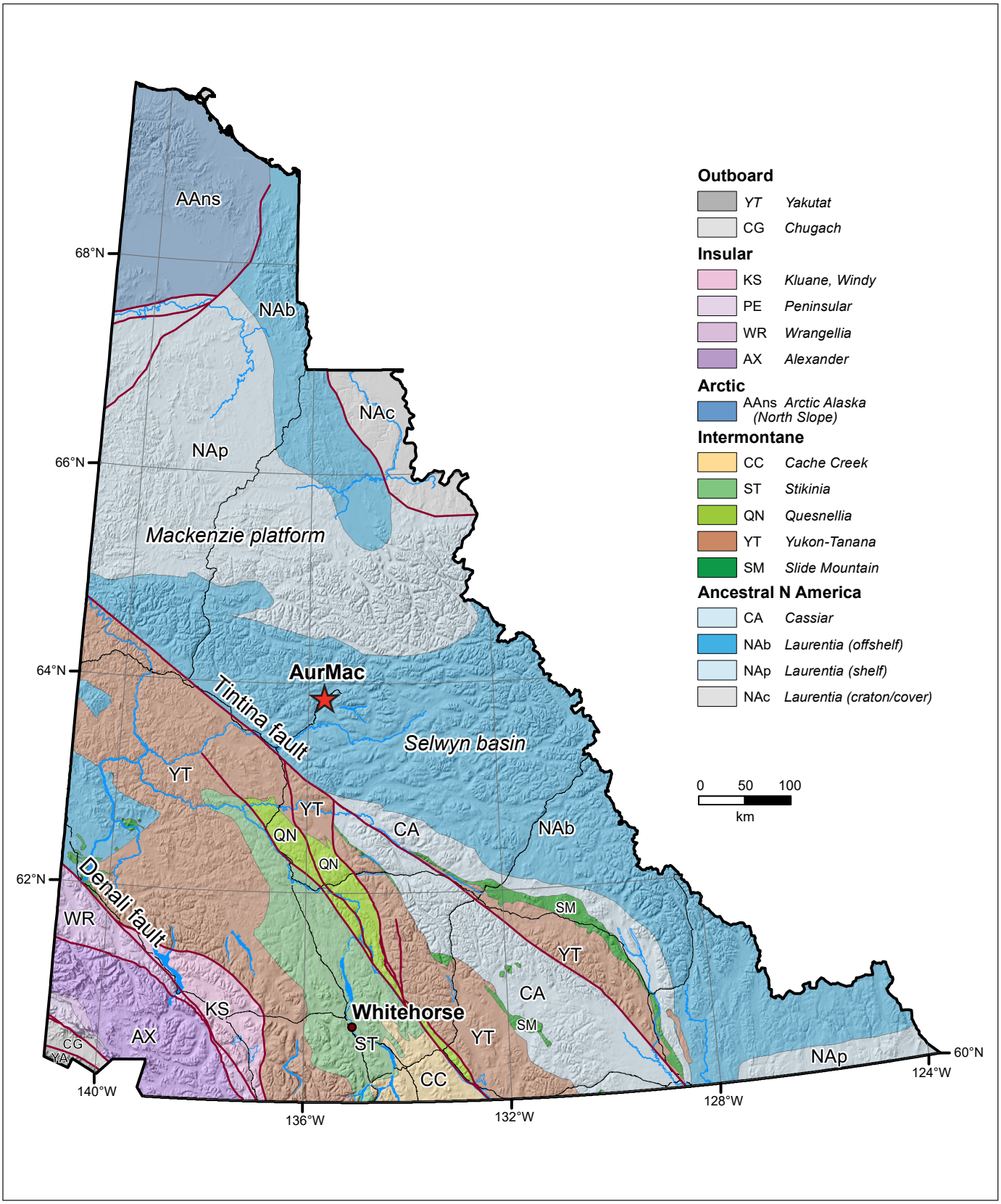

Figure 1. *Location of the AurMac property displayed on the geological terrane map of the Yukon (after Yukon Geological Survey, 2020).*

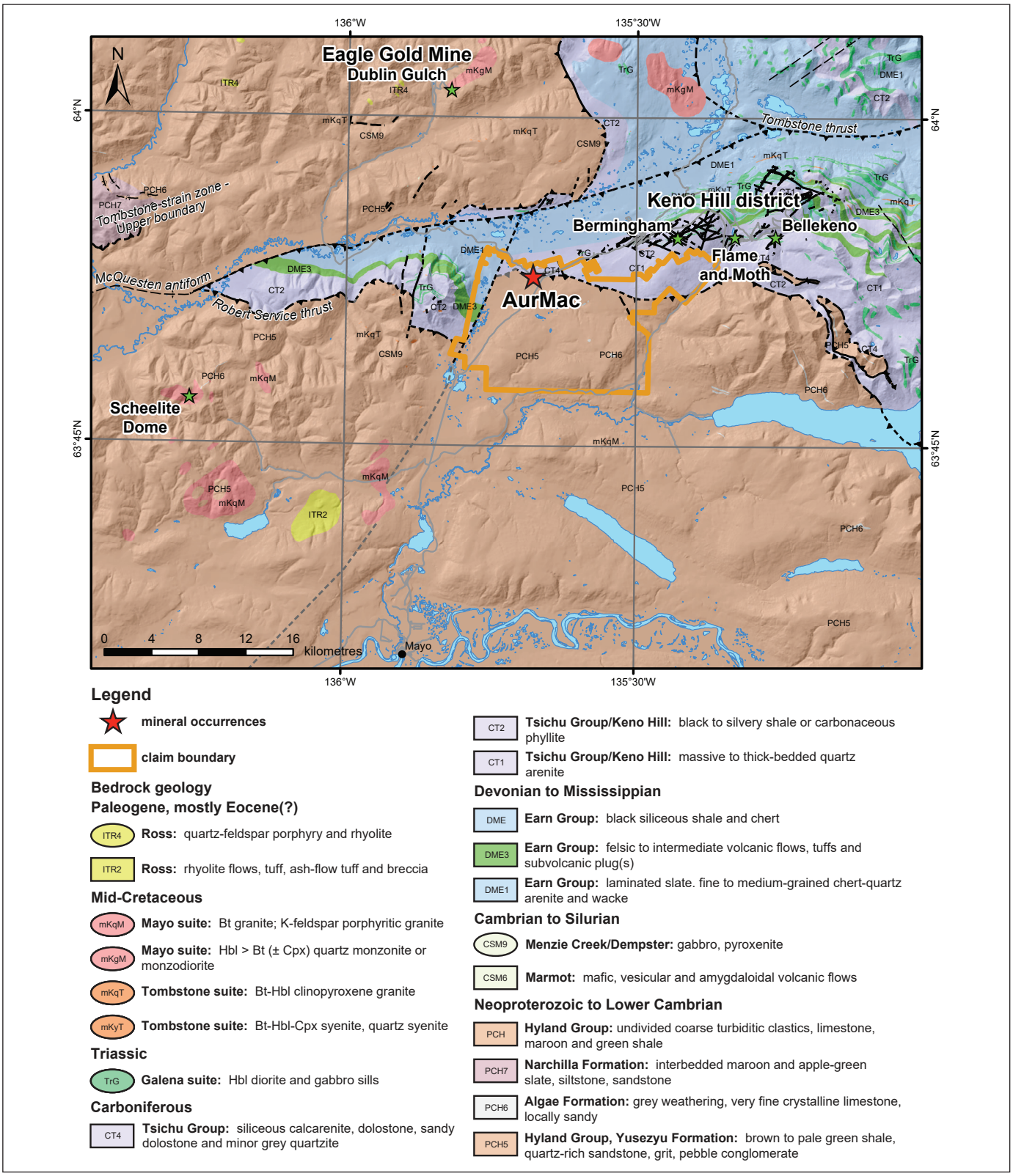

Figure 2. *Bedrock geology map of the area surrounding the AurMac property. Nearby reduced intrusion-related gold systems include Dublin Gulch at the Eagle Gold Mine, and Scheelite Dome. Silver-lead-zinc mineralization occurs in the Bermingham, Bellekeno and Flame and Moth occurrences of the Keno Hill district (after Yukon Geological Survey, 2022).*

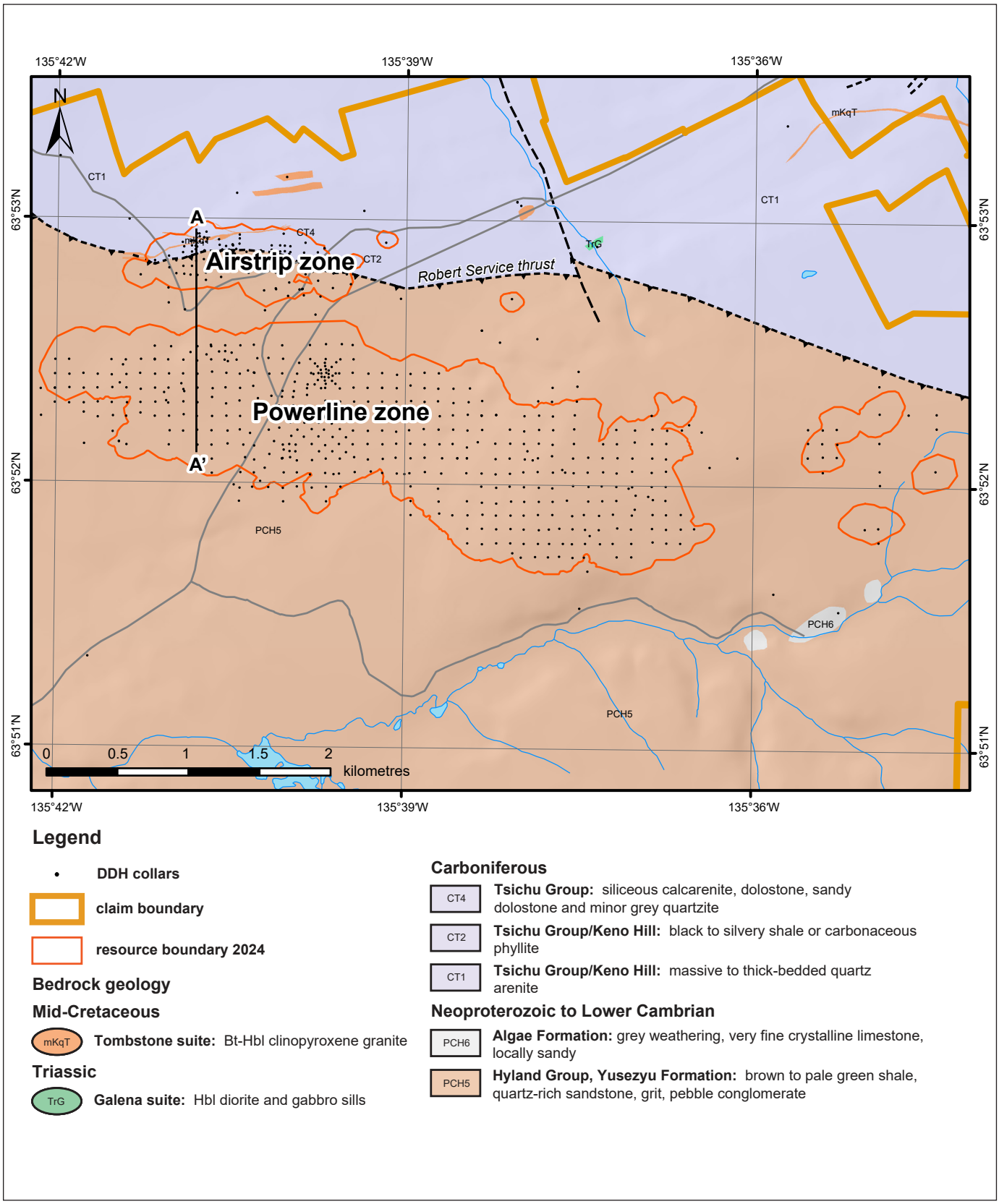

Figure 3. *Diamond drillhole (DDH) collar map illustrating the location of relogged drillhole fence A–A' (466600 mE, UTM Zone 8) through the Airstrip and Powerline zones (after Yukon Geological Survey, 2022).*

was calculated for an aplite dike crosscutting strata in the Airstrip zone, which is interpreted to belong to the Mayo suite.

The latest Cretaceous to earliest Paleocene (67–64 Ma; Murphy, 1997) McQuesten suite forms an east to northeast-trending belt situated between the Tintina fault and Sunshine Creek, and the known eastern limit is located approximately 45 km west of the AurMac property. This suite consists of reduced, peraluminous, medium to coarse-grained, megacrystic, potassium-feldspar-biotite ± muscovite granite, and quartz monzonite stocks and batholiths. The McQuesten suite is associated with silver-tin mineralization in breccias (Murphy, 1997; Rasmussen, 2013).

Regional structure and deformation

Northward Jurassic to Early Cretaceous thrusting resulted in three prominent east-trending thrust faults in the northwestern Selwyn basin area (Mair et al., 2006). The Dawson thrust fault, the farthest north and structurally lowest of the thrusts, juxtaposes Selwyn basin strata over strata of the Mackenzie platform. This thrust is interpreted as a reactivated basin-bounding fault and the defining northern boundary of convergence-related ductile deformation (Mair et al., 2006). The Tombstone thrust, positioned above the underlying Dawson thrust, displaces Mississippian to Jurassic rocks above Upper Jurassic rocks in its footwall (Murphy, 1997). The Robert Service thrust (RST; Fig. 2), the most southerly of the three thrusts, is inferred to pass through the northern part of the AurMac property, where it juxtaposes the Late Proterozoic to Cambrian Hyland Group over the Mississippian to Permian(?) Keno Hill Quartzite and Devonian to Mississippian Earn Group (Murphy, 1997; Read et al., 2020).

Associated with these faults, and structurally overprinting the AurMac property, is the Tombstone strain zone (TSZ, Fig. 2). It is a region of increased deformation characterized by more prominent foliation, lenticular fabrics rather than bedding, mineral stretching lineations, isoclinal folding, asymmetric boudinage, and a slightly higher regional metamorphic grade (Murphy, 1997). The TSZ, extending laterally from the North Klondike River region in the west, to at least the Mt. Westman map area to the east, is defined by the Tombstone thrust at its base, and extends several kilometres upward through the Earn Group, Keno Hill Quartzite, and into the Yusezyu Formation of the Hyland Group along the base of the overlying RST sheet (Murphy, 1997).

The McQuesten antiform (Fig. 2) has its axial trace running north of the AurMac property, and is a steeply south-dipping, reverse-faulted, west-southwest-plunging antiform that folds the RST, Tombstone thrust and the TSZ (Murphy, 1997; Yukon Geological Survey, 2022). This structure is interpreted as the result of out-of-sequence fault propagation fold structures splaying from the Tombstone thrust, or a fault-bend fold resulting from thrusting over underlying ramps (Murphy, 1997, Mair et al., 2006).

The cessation of ductile deformation is interpreted to be closely represented by metamorphic muscovite $^{40}Ar/^{39}Ar$ cooling ages of 100.47 ± 0.40 Ma near Scheelite Dome, and 103.90 ± 0.54 Ma and 104.6 ± 2.00 Ma from the lower RST sheet, which mark cooling through approximately 350°C (Mair et al., 2006). Ductile deformation in the footwall of the Tombstone thrust fault is cross-cut by unfoliated mid-Cretaceous (ca. 98 to 88 Ma) intrusions (Mair et al., 2006).

Brittle deformation that postdates ductile deformation is characterized by north and north-northwest-striking sinistral strike-slip faults, conjugate northeast-trending dextral faults, and east-trending tensional structures (Hart et al., 2000; O'Dea et al., 2000; Stephens et al., 2000; 2004; Mair et al., 2006).

Methodology

In the summer of 2023, detailed core logging and targeted sampling was conducted at the AurMac logging facilities. Thirteen drillholes, totalling 3602 m, were relogged along a north-south section (section A–A' located along 466600 mE from 7082500 mN to 7084100 mN, UTM Zone 8; Fig. 3) through both the Airstrip and Powerline deposits. Polished thin sections were prepared by Vancouver Petrographics Ltd. on representative samples of magmatic units and mineralization observed at the AurMac deposits. Transmitted and reflected light petrography was used for characterization. Representative samples of mafic rocks were sent to ALS Canada Ltd. of North Vancouver, British Columbia, for whole-rock geochemical analyses using the PUL-42 sample preparation and CCP-PKG03 analytical packages. This package includes whole-rock analysis by x-ray fluorescence and trace-element analysis by lithium borate fusion.

Deposit geology

The AurMac property is situated along the regional trace of the RST where the Yusezyu Formation of the Hyland Group in the hanging wall overlies the Mississippian Sourdough Hill Member of the Keno Hill Quartzite in the footwall (Figs. 2 and 3). The area has been structurally overprinted by the TSZ (Fig. 2; Yukon Geological Survey, 2022) where the S_2 foliation and transposition fabric of the TSZ, as described by Murphy (1997) and Mair et al. (2006), defines the schistosity throughout the deposits. Being situated along the southern limb of the north-verging McQuesten antiform, a consistent, moderately south-dipping foliation (Fig. 4; Thornton et al., 2024) is observed across the AurMac deposits. Predominant, north-verging asymmetric folding observed during core logging in 2023 provides evidence that the host bedrock has not experienced significant structural thickening or repetition of strata through deposit-scale folding.

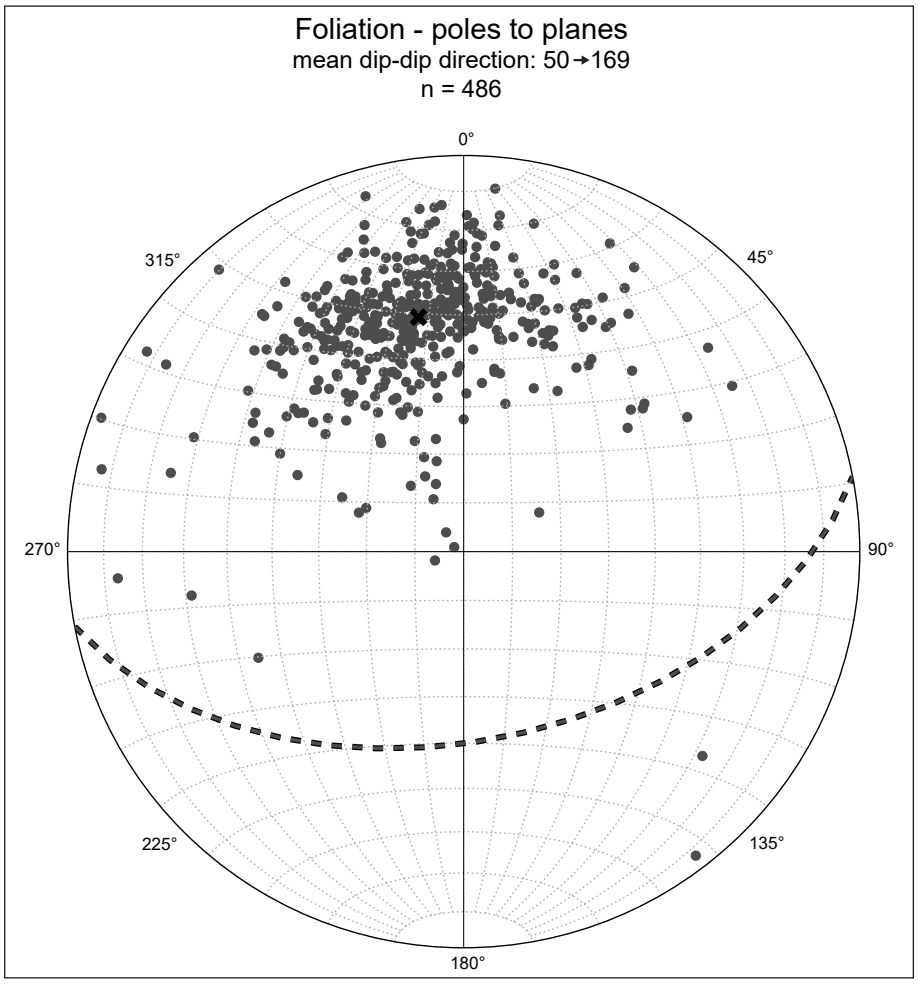

Figure 4. *Stereonet displaying poles-to-planes of south-dipping foliation observed on the AurMac property.*

Lithological units

Siliciclastic metasedimentary rocks

Micaceous metasedimentary rocks comprise the majority of host-rock lithologies at the AurMac deposits. The abundances of chlorite, white micas and muscovite in the metasedimentary lithologies vary across the deposits and are used to differentiate the various units, which are defined by the dominant mineralogy. Because of the variable nature of mica content in the metasedimentary rocks, the ideal end-member schist units described below are rare and lithologies with intermediate characteristics are more common.

Mica-quartz schist

White mica–quartz ± chlorite ± biotite schist is a fine-grained, quartz-dominated lithology that typically exhibits a light to medium grey colour, but transitions to dark grey to black and brown where it is carbonaceous and contains biotite, respectively (Fig. 5a). Micaceous laminae and bands are interspersed with planar sub-centimetre to sub-decimetre quartz segregations constituting 5–25% of the rock. Occasionally, 'gritty' bands of strained, coarse-grained (less than 3 mm), grey-black to light grey quartz clasts occur in sub-decimetre bands. The unit is more competent and resistant to scratching relative to mica-dominated schists, and silvery phyllitic foliation surfaces are exposed on broken surfaces. Where more mica-rich, the unit may host very fine to fine-grained disseminated pyrrhotite (less than 1%) and be weakly magnetic. White mica–quartz ± chlorite ± biotite schist is the most common unit in the Powerline zone and occurs in more shallow strata of the Airstrip zone.

Quartz-sericite schist

Quartz-sericite schist is a very fine grained white mica-dominated lithology characterized by its light beige-grey colour and relatively high fissility (Fig. 5b). Very narrow foliation is irregular, undulating

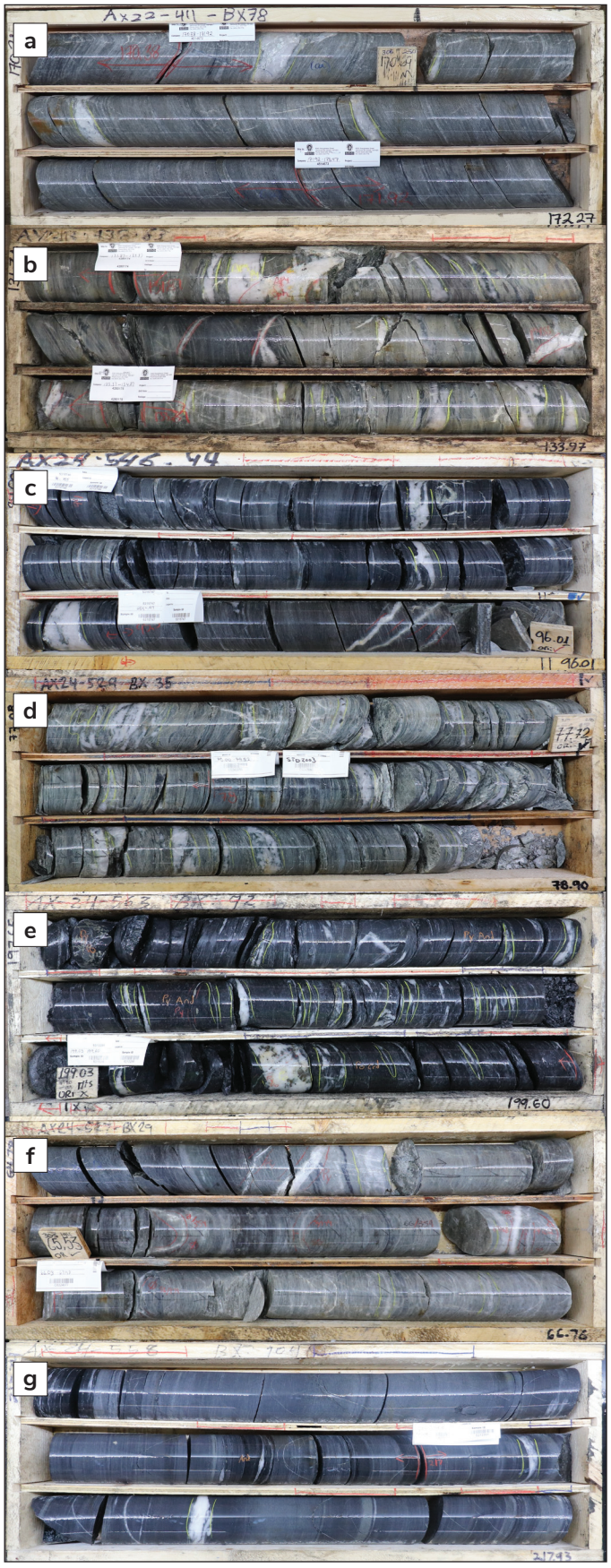

around quartz segregations, and tight to isoclinal folds are commonly observed. Sub-centimetre to sub-decimetre quartz segregations constitutes 5–20% of the unit and often appear as boudins or isoclinal rootless fold hinges with axial planes oriented parallel to foliation. Less than 5 mm, ovoid to blocky chloritoid porphyroblasts occasionally occur in white mica bands and have been completely retrograded to white mica and chlorite (Fig. 6a). Pyrrhotite, constituting less than 1% of the rock, occurs as very fine to fine-grained disseminations within micaceous bands contributing to the rocks being weakly to moderately magnetic where present. Quartz-sericite schist is identified in the Powerline and Airstrip zones.

Quartz-chlorite schist

Quartz-chlorite schist is a very fine grained, dark green-grey, chlorite-dominated lithology (Fig. 5c). Similar to the quartz-sericite schist, quartz-chlorite schist is relatively soft and fissile and has very narrow folia that undulate around quartz segregations and are commonly folded into tight to isoclinal folds. Quartz segregations generally constitute less than 10% of the rock and, like those observed in quartz-sericite schist, have sub-centimetre to sub-decimetre widths and occur as boudins and rootless isoclinal fold hinges. Cordierite porphyroblasts, although more frequent in carbonaceous units, occur in chlorite bands and appear as faint, 'ghostly', medium to dark grey, <8 mm ovoid to diamond-shaped porphyroblasts (Fig. 6b). Disseminated fine-grained pyrrhotite, comprising up to 1% of the rock, is more prevalent relative to muscovite-quartz and quartz-sericite schists and contributes to the schist's moderate to strong magnetism. Quartz-chlorite schist is identified in the Powerline zone and more shallow strata of the Airstrip zone.

Figure 5. *Core photos from drillholes on the AurMac property. Core diameter is 71 mm (HTW).* ***(a)*** *Mica-quartz schist in drillhole AX-22-411.* ***(b)*** *Quartz-sericite schist in drillhole AX-23-438.* ***(c)*** *Quartz-chlorite schist in drillhole AX-24-546.* ***(d)*** *Quartz-sericite-chlorite and quartz-chlorite-sericite schist in drillhole AX-24-546.* ***(e)*** *Graphitic schist in drillhole AX-24-563.* ***(f)*** *Quartzite in the Powerline zone from drillhole AX-24-559.* ***(g)*** *Quartzite in the Airstrip zone from drillhole AX-24-558.*

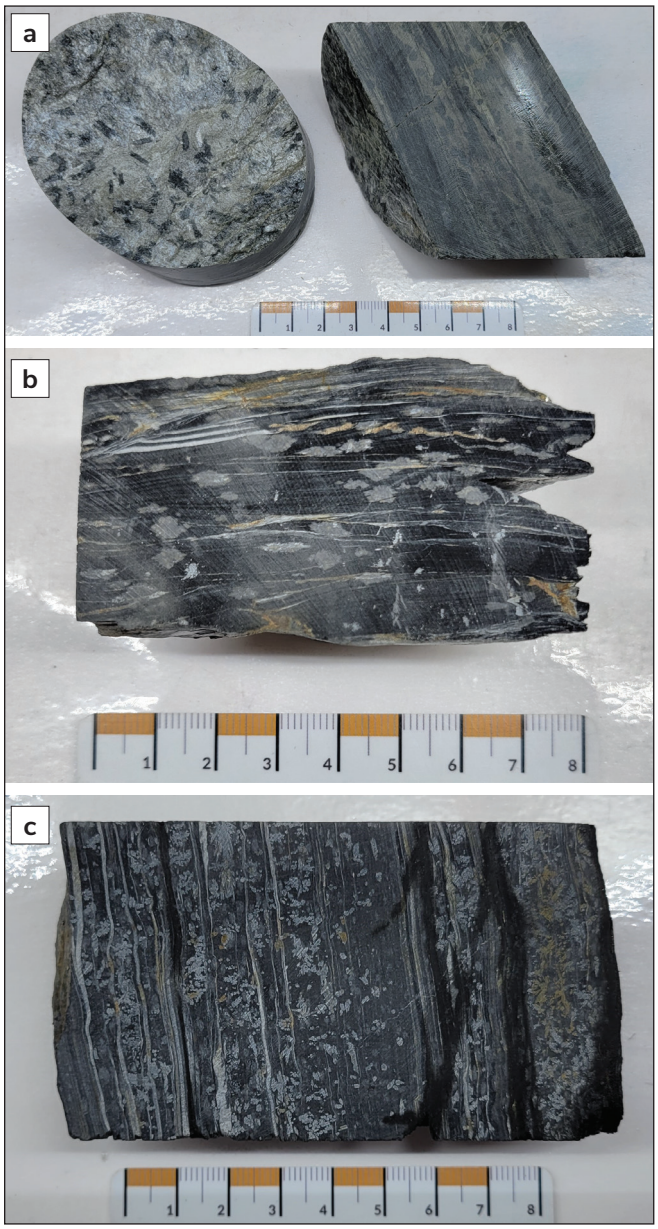

Figure 6. *Examples of minerals from the AurMac property. All scales are in centimetres.* ***(a)*** *Chloritoid porphyroblasts in quartz-sericite schist.* ***(b)*** *Cordierite porphyroblasts in graphitic schist.* ***(c)*** *Andalusite porphyroblasts in graphitic schist.*

Quartz-sericite-chlorite and quartz-chlorite-sericite schist

Quartz-chlorite-sericite and quartz-sericite-chlorite schists represent an intermediate facies between the quartz-chlorite and quartz-sericite schists. These lithologies are very fine grained and characterized by alternating or interfingering dark green-grey chlorite, beige to grey-white mica, and quartz-rich bands and laminae (Fig. 5d). As with other mica-dominated units, quartz-chlorite-sericite and quartz-sericite-chlorite schists are very soft and fissile. Folded and boudinaged quartz segregations, constituting approximately 10% of the rock, are similar to those observed in chlorite and sericite-dominated schists. Chloritoid and cordierite porphyroblasts, as observed in quartz-sericite and quartz-chlorite schists, occur in white mica and chlorite bands, respectively (Figs. 6a, b). Very fine grained disseminated pyrrhotite, which is most common in chlorite-rich bands, constitutes less than 1% of the rock and contributes to the unit's moderate to strong magnetism. Quartz-chlorite-sericite and quartz-sericite-chlorite schists are identified in the Powerline zone.

Graphitic schist

Quartz-rich graphitic schist is present in the Powerline zone as metre-scale horizons and found in larger decametre-scale horizons in the Airstrip zone. This lithology is very fine grained and consists predominantly of black graphite laminae and bands, which are interspersed with grey-black carbonaceous quartz and occasional chlorite bands and laminae (Fig. 5e). Among the schist varieties at AurMac, graphitic schist is the most fissile and soft, and is notably prone to faulting resulting in prominent rubble and gouge-rich fault zones. Quartz segregations within the graphitic schist are similar to those in mica-dominated schists, occurring as sub-centimetre to sub-decimetre boudins and rootless isoclinal fold hinges. Fine to coarse-grained andalusite porphyroblasts are observed at depth in the Airstrip zone and appear as white, sub-centimetre radiating columnar clusters or as square cross sections of individual crystals (Fig. 6c). The unit hosts less than 1% fine-grained euhedral pyrite and up to 5% very fine grained to blebby pyrrhotite occasionally intergrown with chalcopyrite, which contributes to a pervasive, moderate to strong magnetism that differentiates the unit from other schists. Very fine grained disseminated carbonate is more common in graphitic schists in the Airstrip zone, where reactions to dilute muriatic acid are moderately vigorous. Quartz-graphite schist is identified in the Powerline and Airstrip zones.

Quartzite

Quartzite is present in both the Powerline and Airstrip zones, although it is more prevalent and visually distinct in the Airstrip zone.

In the Powerline zone, quartzite units are relatively uncommon and characterized by their fine to coarse-grained texture, light grey colour with dark grey to black

carbonaceous banding, and vitreous texture (Fig. 5f). Relative to mica-rich schists, quartzite exhibits wider banding with more consistently planar foliation, and bands of coarse-grained, rounded grey to dark-grey quartz clasts or 'grit' are a common feature. Quartzite units have the highest competency among the units in the Powerline zone and in drill core, and have scratch-resistant polished surfaces. Quartzite units are less fissile than mica-bearing schists, and fracture surfaces expose uneven, mica-poor surfaces. Quartz segregations in these units are similar to that found in schists, comprising less than 10% of the rock (rarely up to 20%), and have sub-centimetre to sub-decimetre widths. Disseminated fine-grained to blebby pyrrhotite is most often absent, which differentiates quartzite horizons from more quartz-rich schist units.

In the stratigraphically deeper parts of the Airstrip zone, quartzite units are very fine to fine grained, are carbonaceous with a medium grey to black colour, and lack the coarse-grained 'gritty' bands observed in quartzite of the Powerline zone (Fig. 5g). Graphitic partings and bands are common and host radiating, white, fine to coarse-grained andalusite porphyroblasts like those observed in graphite schists (Fig. 6c). Mica content in the Airstrip zone quartzite units is notably elevated relative to quartzite in the Powerline zone, and where present, is associated with zones of increased fissility. These quartzite units exhibit high competency and resistance to scratching, similar to those found in the Powerline zone. Horizons of very fine grained carbonate disseminations are more common in the Airstrip zone quartzite and react moderately with dilute muriatic acid. Disseminated, very fine grained to blebby pyrrhotite occurs in more carbonaceous and calcareous horizons, and is associated with weak to moderate magnetism. Brecciation is prevalent in the Airstrip zone quartzite units, characterized by an iron carbonate matrix hosting fine to coarse-grained sphalerite ± galena ± arsenopyrite ± pyrite ± pyrrhotite.

Calcareous metasedimentary rocks

Calcareous units are found throughout the AurMac deposits but are notably more abundant in the Airstrip zone, where gold mineralization is primarily associated with skarn horizons (Gray and Thom, 2021). Calcareous units are differentiated by their carbonate content and varying degrees of silicification and alteration, and rarely have sharp, well-defined contacts.

Calcareous schist

Calcareous schist units, which are defined by an elevated concentration of limey horizons within micaceous schists, are observed in both the Powerline and Airstrip zones. The mineralogical composition of these units varies and ranges from being dominated by quartz, chlorite or white mica. This unit exhibits similar colour, foliation, competency and quartz segregation abundances with previously described schists. The primary distinction made between calcareous schists and previously described metasedimentary units is based on elevated, very fine to fine-grained carbonate disseminations and limey, fine-grained laminae and banding, which contribute to a pervasive, moderate to strong reaction with dilute muriatic acid. Disseminated fine-grained to blebby pyrrhotite is more abundant in calcareous schists, comprising up to 2% of the units, and results in these units having moderate to strong magnetism. Calcareous schists are identified throughout the AurMac deposits but are more prevalent in the Airstrip zone.

Marble

Marble is notably more widespread in the Airstrip zone compared to the Powerline zone and is visually distinct between the two deposits.

In the Powerline zone, foliated marble is fine to medium grained and ranges in colour from white to blue-grey. Powerline zone marble is predominantly composed of calcite, and has less than 10% fine-grained quartz and very fine grained micaceous laminae (Fig. 7a). Individual limestone horizons typically do not exceed 5 m in width and are often intercalated with dark green to grey, quartz-chlorite schist or beige-grey, quartz–white mica schist. These marble horizons possess higher competency and hardness relative to schists and are most readily identified by their vigorous reaction to dilute muriatic acid, having the strongest reaction relative to all other units. although laminae and banding are generally planar, well-developed, open to narrow folding can be observed. Sub-centimetre quartz-carbonate segregations are rare, comprising up to 5% of the unit.

Marble horizons are more extensive in the Airstrip zone and individual band thicknesses average approximately 2 m and occasionally reach up to 10 m. In contrast to marble in the Powerline zone, marble in the Airstrip zone is fine grained and has chlorite, white mica and graphitic partings contributing to its grey, green and black hues (Fig. 7b). Although marble horizons in

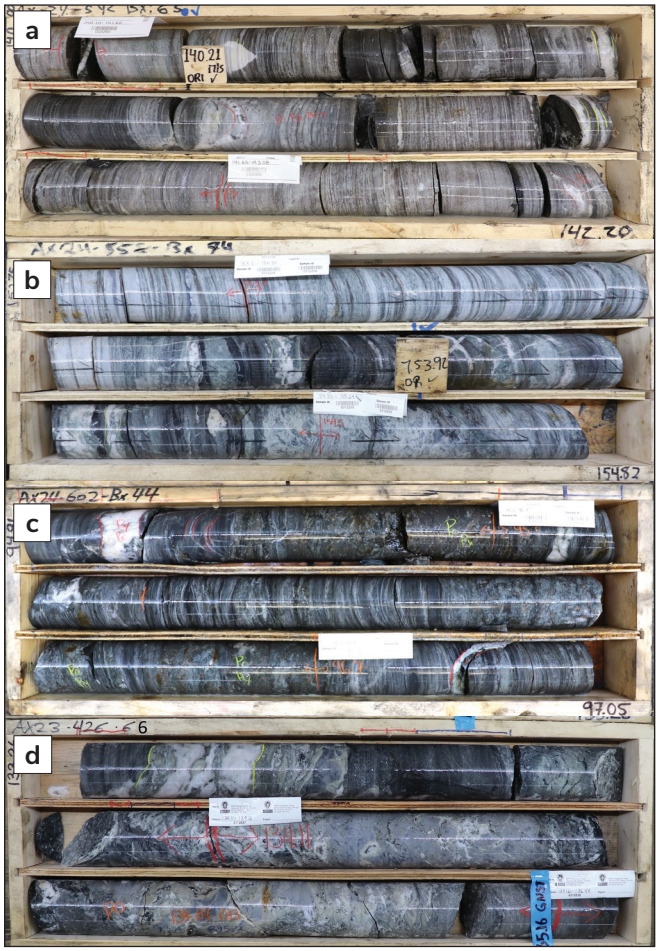

Figure 7. *Core photos from drillholes on the AurMac property. Core diameter is 71 mm (HTW).* ***(a)*** *Marble in the Powerline zone from drillhole AX-24-542.* ***(b)*** *Marble in the Airstrip zone from drillhole AX-24-558.* ***(c)*** *Alternating foliated calc-silicate and massive skarn from drillhole AX-24-558.* ***(d)*** *Very fine grained calcareous quartzite in drillhole AX-23-426.*

the Airstrip zone are relatively competent, they are comparatively less so than those in the Powerline zone due to their higher mica content. Centimetre to sub-decimetre-wide quartz-carbonate segregations are more abundant in the Airstrip zone marble, comprising up to 10% of the unit.

Foliated calc-silicate rocks

In the Airstrip zone and less frequently in the Powerline zone, foliated, fine-grained, banded to laminated calc-silicate rocks (Fig. 7c) occur along margins of marble, calcareous schist and massive skarn horizons; they typically have widths of <2 m. Calc-silicate hornfels are green-grey, grey-brown or beige, and feature wispy white mica and chlorite laminae, which separate massive, light to medium-grey-green lenses of fine-grained calcite, quartz and epidote-clinozoisite. The competency of these calc-silicate rocks varies with zones of increased natural fracturing associated with elevated mica content. Foliated calc-silicate horizons host up to 2% fine-grained disseminated pyrrhotite, trace chalcopyrite and rare fine to medium-grained scheelite. Where pyrrhotite is present, the unit is moderately to strongly magnetic. Reactions with dilute muriatic acid are moderate to strong, and primarily occur along the calcite-bearing bands between white mica folia.

Massive skarn

Skarn horizons are most prominent in the Airstrip zone where they can reach several metres in width. In contrast, skarn horizons in the Powerline zone are scarce and widths rarely exceed 1 m. Skarn horizons are characterized by their grey to brown colour, abundant sulphide content, intense silicification, high competency and massive fine to coarse-grained texture (Fig. 7c). Sulphides in skarn horizons, sometimes exceeding 10% of the unit, consist of net-textured to blebby pyrrhotite, lesser fine to medium-grained pyrite and arsenopyrite, and very fine to fine-grained chalcopyrite. Due to the high pyrrhotite content, skarn horizons are the most strongly magnetic of all units observed on the AurMac property. Carbonate content is low in these units and when tested with dilute muriatic acid, reactions are generally weak to moderate, and observed sporadically.

Petrographic analysis reveals that skarn units have a quartz-calcite matrix surrounding equant, fine to medium-grained clinopyroxene; fine-grained, elongate and fibrous amphibole; and fine-grained feldspar. It also contains fine to coarse-grained scheelite, fine-grained biotite and chlorite, and rare fine-grained garnet.

Very fine grained calcareous quartzite(?)

Very fine grained, variably calcareous quartzite(?) horizons are only observed in the Powerline zone and occur as distinct highly competent, light grey to black, very fine grained, massive calcareous and siliceous rocks, and widths rarely exceed 1 m (Fig. 7d). Carbonate content is lower than that of marble, and when tested with dilute muriatic acid, exhibits a pervasive, weak to moderately vigorous reaction. Brecciation is common in these quartzite horizons and typically occurs as mosaic breccias with black intraclastic crackle brecciation. Calc-

silicate alteration, where present, can be near pervasive, and is texturally destructive, resulting in a green-grey to brown mottled colouration. Unlike in previously described units, quartz segregations are absent. Fine to medium-grained pyrrhotite disseminations and blebs are present where calc-silicate alteration occurs, comprising up to 1% of the unit, and are associated with moderate to strong magnetism. Unit margins are generally obscured by alteration; however, where unaltered, they exhibit sharp and conformable contacts.

Magmatic rocks

Mafic rocks

Foliated mafic units at the AurMac property are confined to the Powerline zone and occur as fine to medium-grained sets of sub-metre thick bands that rarely exceed 20 m in true thickness. The mafic units are characterized by a dark green to grey and brown banded appearance, and contain fine-grained pervasive chlorite, very fine grained disseminated carbonate, and brown, fine-grained laminated to banded biotite (Fig. 8a). The rocks are relatively competent compared to surrounding schists and exhibit minimal natural fracturing. Carbonate is generally pervasive and has a weak to moderately vigorous reaction with dilute muriatic acid. Key characteristics that assist with differentiating the unit from others include the absence of quartz segregations, the presence of pervasive, very fine to fine-grained pyrrhotite associated with moderate to strong magnetism, a darker colour relative to metasedimentary schists, and contacts that are sharp and conformable to foliation.

Figure 8. *Core photos from drillholes. Core diameter is 71 mm (HTW).* ***(a)*** *Mafic sills/volcanic units in drillhole AX-24-528.* ***(b)*** *Aplite dike in drillhole AX-24-598.*

Petrographic analysis reveals that the mafic units have a well-developed foliation defined by mineralogically alternating layers. These layers consist of a) fine-grained hornblende (<5%), biotite (10%) and fine-grained to blebby pyrrhotite (<5%) set in a very fine grained chlorite matrix and b) layers of fine to medium-grained biotite (10%) and fine-grained chlorite (10%) embedded in a very fine to fine-grained quartz-white mica matrix (Fig. 9).

Aplite dike

Crosscutting the schists in the Airstrip zone is a light grey to pale green, massive, fine to medium-grained quartz-phyric aplite dike (Fig. 8b). This dike is characterized by its near-pervasive carbonate alteration, exhibiting a weak to moderate reaction with dilute muriatic acid, and sparse sub-centimetre quartz phenocrysts. The aplite dike dips steeply, approximately 70° toward the south (strike of 175°) and bifurcates as it extends west from section 466600 mE (Fig. 3). The average true width, calculated from drill core intercepts, is approximately 3.5 m, but true widths can range from less than 2 m up to approximately 26 m in drillhole MQ-20-66.

Petrography reveals the dike consists of weakly strained less than 2 mm quartz phenocrysts (40%) hosted in a highly altered, fine-grained muscovite to sericite (50%;

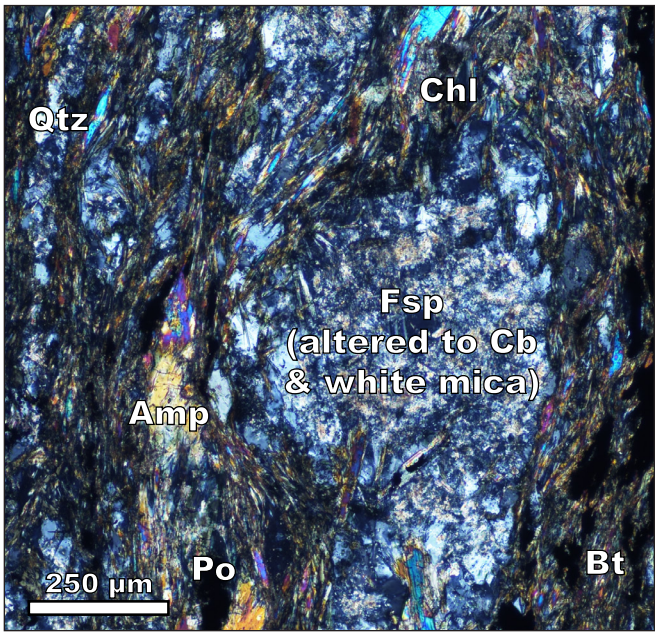

Figure 9. *Cross-polarized transmitted light photomicrograph displaying an example of mafic rocks composed of amphibole (Amp), biotite (Bt), chlorite (Chl), quartz (Qtz), pyrrhotite (Po; opaque), and feldspar (Fsp) partly altered to carbonate (Cb) and white mica.*

after feldspar?) and carbonate (10%) groundmass (Fig. 10). The aplite hosts less than 1% fine to medium-grained scheelite and up to 1% disseminated sulphides consisting of fine to medium-grained arsenopyrite, and fine-grained pyrite, pyrrhotite and sphalerite.

Geochemical analyses

Whole-rock geochemical analyses were conducted on the mafic rocks observed in the Powerline zone to characterize their compositions, rare earth element (REE) signatures, and for correlation with potentially analogous mafic units mapped outside of the AurMac property.

Zirconium (Zr) to titanium (Ti) versus niobium (Nb) to yttrium (Y) immobile element plots (Fig. 11; modified from Pearce, 1996) reveal that the mafic rocks at AurMac exhibit alkali basaltic compositions. Chondrite-normalized REE patterns (Fig. 12; Anders and Grevesse, 1989) of the mafic units exhibit a signature transitional between oceanic island basalts (OIB) and enriched mid-ocean ridge basalts (E-MORB; Sun and

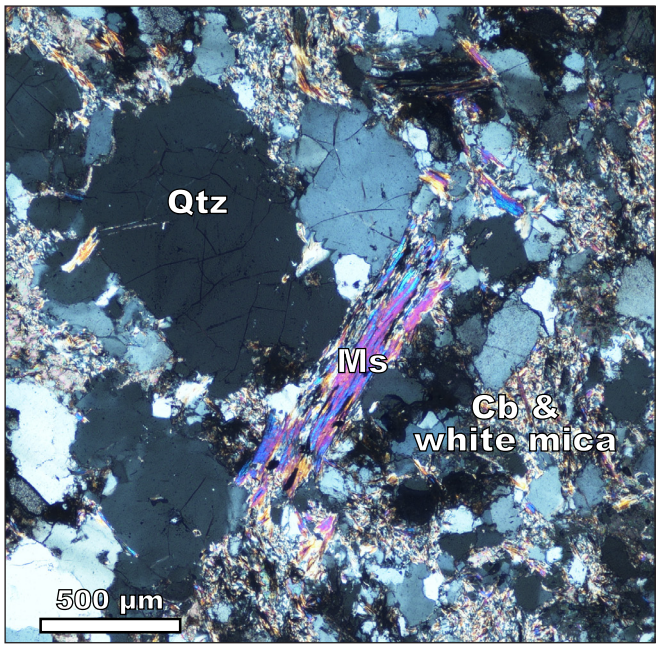

Figure 10. *Cross-polarized transmitted light photomicrograph of the aplite dike composed of quartz (Qtz) and muscovite (Ms) in a matrix that is intensely altered to carbonate (Cb) and sericite (white mica).*

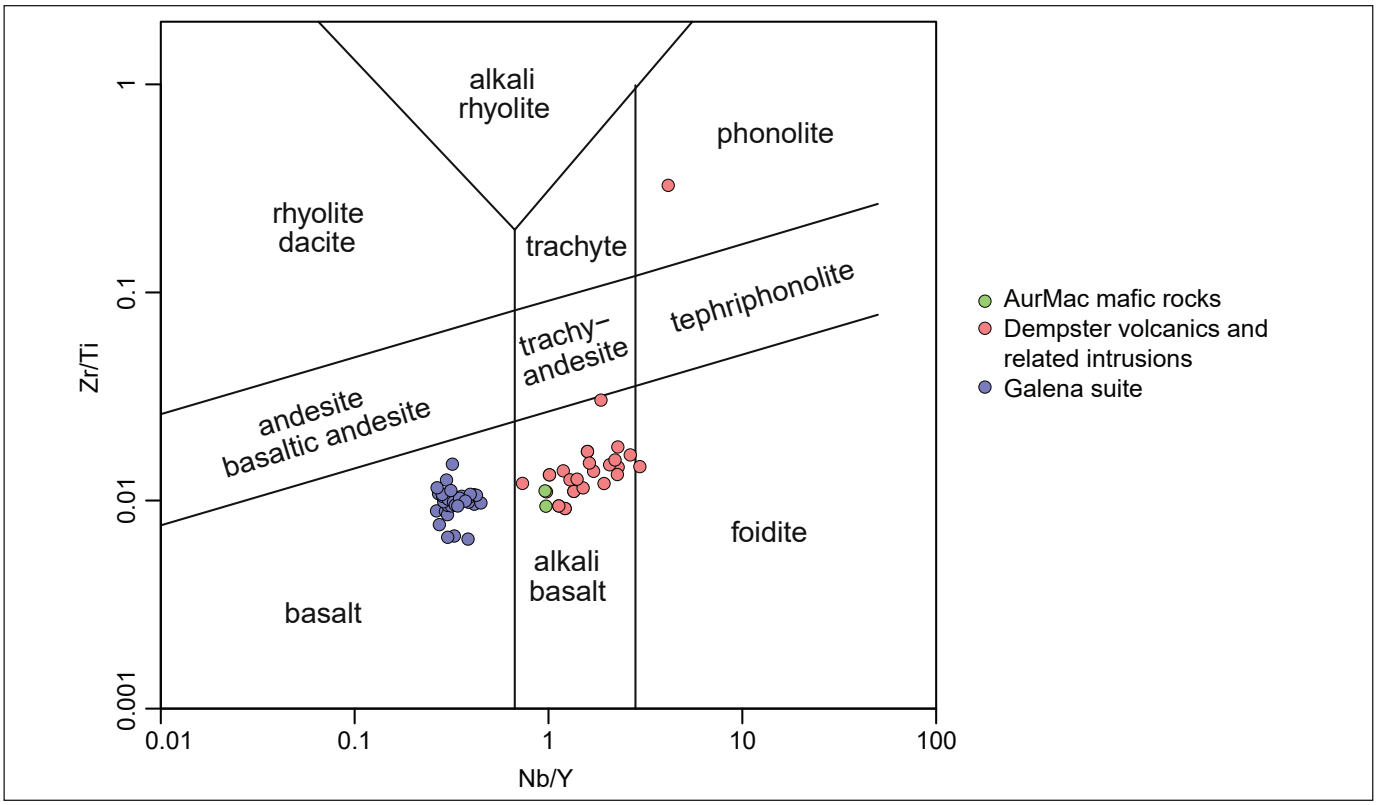

Figure 11. *Zirconium (Zr) to titanium (Ti) versus niobium (Nb) to yttrium (Y) immobile element plot (modified from Pearce, 1996) of mafic units at AurMac (this study), Triassic Galena suite sills (Yukon Geological Survey, 2023b), and Dempster volcanics and related intrusions (Yukon Geological Survey, 2023b).*

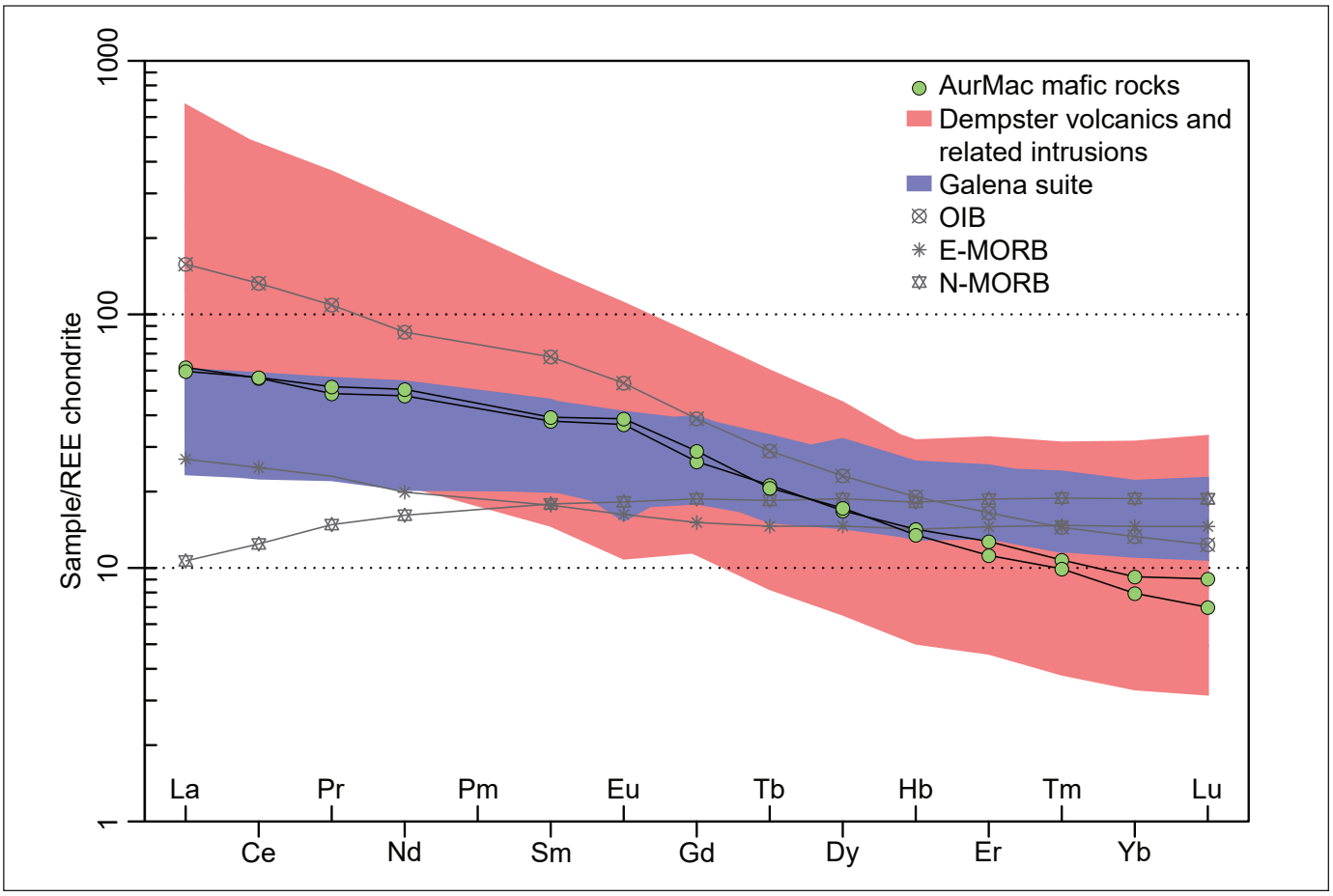

Figure 12. *Chondrite-normalized REE plot (Anders and Grevesse, 1989) of mafic units at AurMac (this study), Triassic Galena suite sills (Yukon Geological Survey, 2023b), and Dempster volcanics and related intrusions (Yukon Geological Survey, 2023b). E-MORB: enriched mid-ocean ridge basalt; N-MORB: normal mid-ocean ridge basalt; OIB: oceanic island basalt.*

McDonough, 1989), and a stronger enrichment in light REEs relative to heavy REEs.

Mafic units at AurMac could correspond to two varieties of mafic intrusions that have been mapped in the McQuesten, Mayo, Clark Lakes and Hart River map areas, including the Triassic Galena suite sills that intrude the Keno Hill Quartzite and underlying Earn Group (McOnie, 2016; Read et al., 2020), and intermediate to mafic Cambro-Ordovician intrusions and volcanic rocks (Dempster Volcanics), mapped within, and conformably overlying, the Hyland Group (Roots and Abbott, 1988; Abbott, 1997; Murphy, 1997; Skipton and Maw, 2021; Yukon Geological Survey, 2023b). The geochemical signatures of the mafic units at AurMac most closely resemble, and have been correlated with, the Cambro-Ordovician intrusions and volcanic rocks. This correlation has resulted in the interpretation that metasediment rocks hosting the Powerline zone belong to the Hyland Group and are situated in the hanging wall of the RST (Fig. 13).

Cross sections and unit correlation

Interpolation of previously described lithological units between drillholes relogged along the 466000 mE fence results in the cross section in Figure 13. A correlation of units observed at the AurMac deposits has also been made with the geology published in reports and maps from the nearby Keno Hill district (Fig. 14; Read et al., 2020). Metamorphic isograds based on porphyroblasts observed in drill core are presented in Figure 15. These porphyroblasts, grading from chloritoid in the south, to cordierite, then andalusite in the north highlight an increasing metamorphic grade to the north.

Siliciclastic metasedimentary rocks observed along the southern part of the section in the Powerline zone are

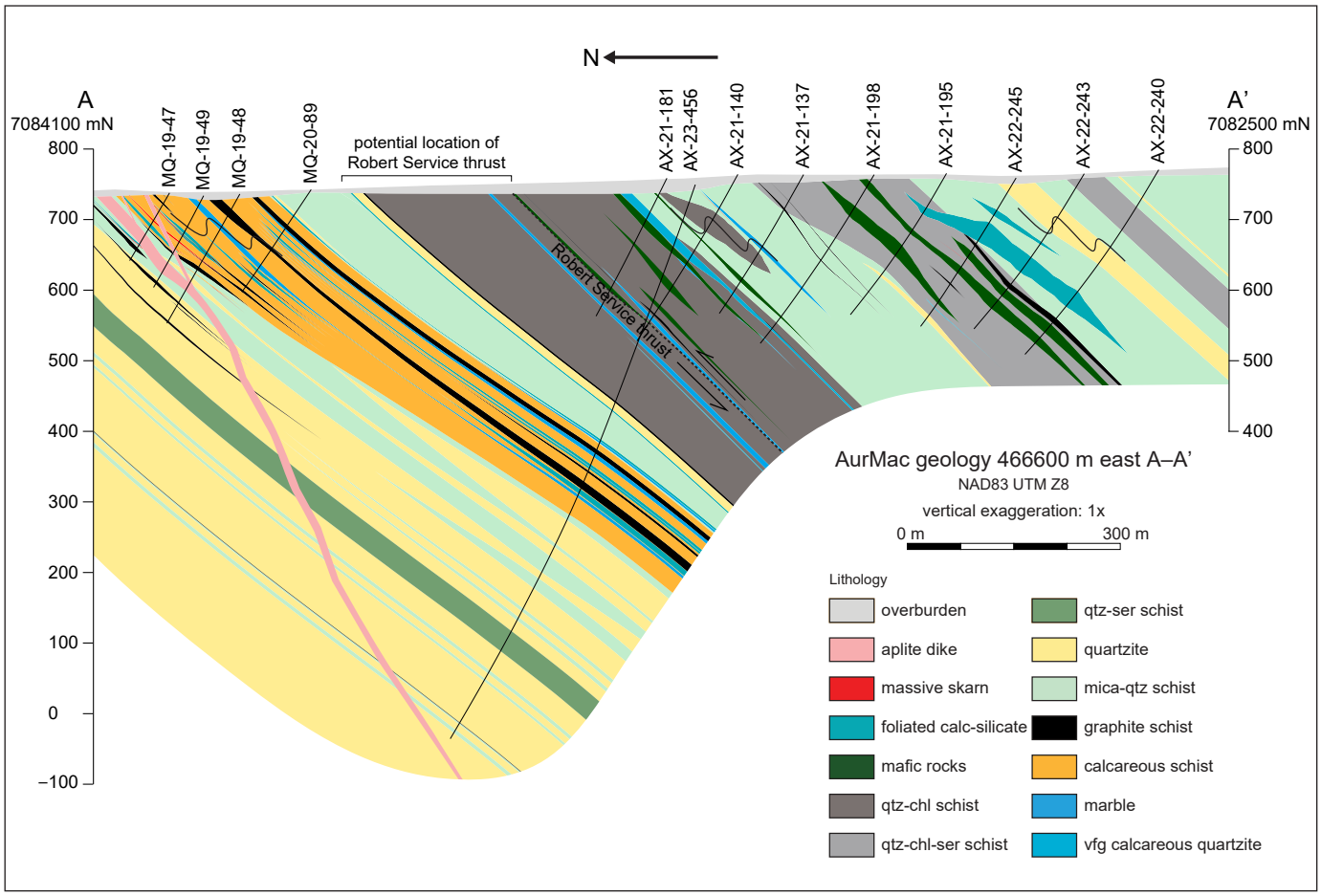

Figure 13. *Geological cross section A–A' along 466600 mE from 7084100 mN to 7082500 mN (UTM Zone 8) through both the Airstrip and Powerline zones. Chl: chlorite, qtz: quartz, ser: sericite, vfg: very fine grained.*

dominated by variable 'gritty' mica-quartz and chlorite and white mica-rich quartz-mica schists, and consist of subordinate graphitic schist, variable calc-silicate-altered marble, and quartzite. These units are correlated with Hyland Group rocks of the Yusezyu Formation (PY) in the Keno Hill district where they are described as chlorite-muscovite schists, quartz grain, gritty schists and metagrit. The lower limit of the Hyland Group and stratigraphically highest potential position of the RST in the Powerline zone is defined by the stratigraphically lowest occurrence of foliated mafic rocks, which have been correlated through whole-rock geochemistry with Cambro-Ordovician (**Cd**) mafic rocks mapped within the Hyland Group (Figs. 11 and 12; Skipton and Maw, 2021).

Quartzite observed in the lower stratigraphic levels of the Airstrip zone are correlated with the Upper Quartzite unit (MSq) in the Keno Hill district. These units share similar grey to dark grey colours, graphitic partings and fissile fracturing.

Calcareous metasedimentary rocks are observed above the Upper Quartzite in the Airstrip zone and include variably calc-silicate-altered micaceous marble and calcareous schists. These carbonate-rich horizons are flanked by variably calcareous, andalusite-bearing carbonaceous to graphitic schists, which are correlated with grey, locally phyllitic limestone (MSls), and locally limey graphitic and siliceous schists (MSg), respectively, of the Sourdough Hill Member mapped in the Keno Hill district.

Above the calcareous metasedimentary rocks in the Airstrip zone, and below the mafic units observed in the Powerline zone, are horizons of green-grey chlorite and quartz-dominated schists. These rocks have been correlated with undifferentiated green and grey-green schists of the Sourdough Hill Member (MSc) although the extent of potential intercalation with overlying Hyland Group along the RST is unknown.

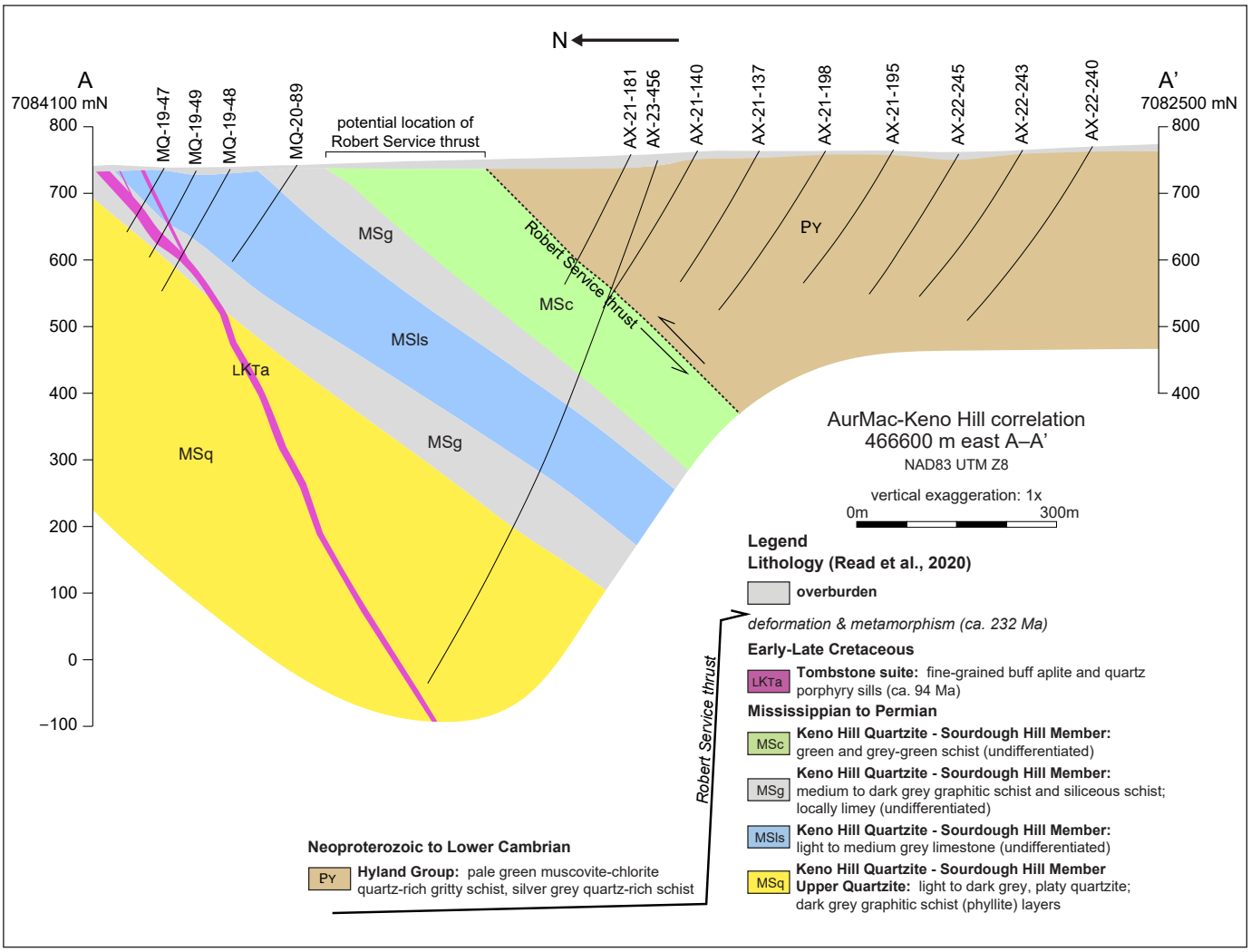

Figure 14. *Cross section A–A' along 466600 mE from 7084100 mN to 7082500 mN (UTM Zone 8) illustrating unit correlations made with Keno Hill district geology from Read et al. (2020).*

The quartz-phyric aplite dike, crosscutting strata in the Airstrip zone along the north end of the section, is correlated with mid-Cretaceous aplite and quartz porphyry sills mapped in the Keno Hill district (LKta).

Mineralization styles and alteration

Gold mineralization within the AurMac property is characterized by two primary styles consisting of lithologically controlled carbonate replacement skarn, found primarily in the Airstrip zone, and structurally controlled sheeted veining found primarily in the Powerline zone. Although currently considered economically insignificant, silver-lead-zinc mineralization postdates and crosscuts gold mineralization throughout the deposits at AurMac.

Sheeted veins

Gold mineralization in the Powerline deposit is predominantly associated with arrays of sheeted quartz–carbonate ± albite veins that crosscut all fabrics related to ductile deformation and typically host less than 5% sulphides consisting of arsenopyrite–pyrite ± pyrrhotite ± chalcopyrite ± sphalerite ± lead–bismuth sulphosalts. Vein widths range from millimetre to decimetre-scale, and have an average width of less than 2 cm. Vein density appears rheologically controlled, and higher vein densities are associated with more siliceous host rocks, and in mineralized zones, they vary from approximately one to more than five veins per metre (Fig. 16a). Sheeted veins within the Powerline deposit are consistently shallowly dipping approximately 15° to the north (Fig. 17), and occur clustered in stacked horizons.

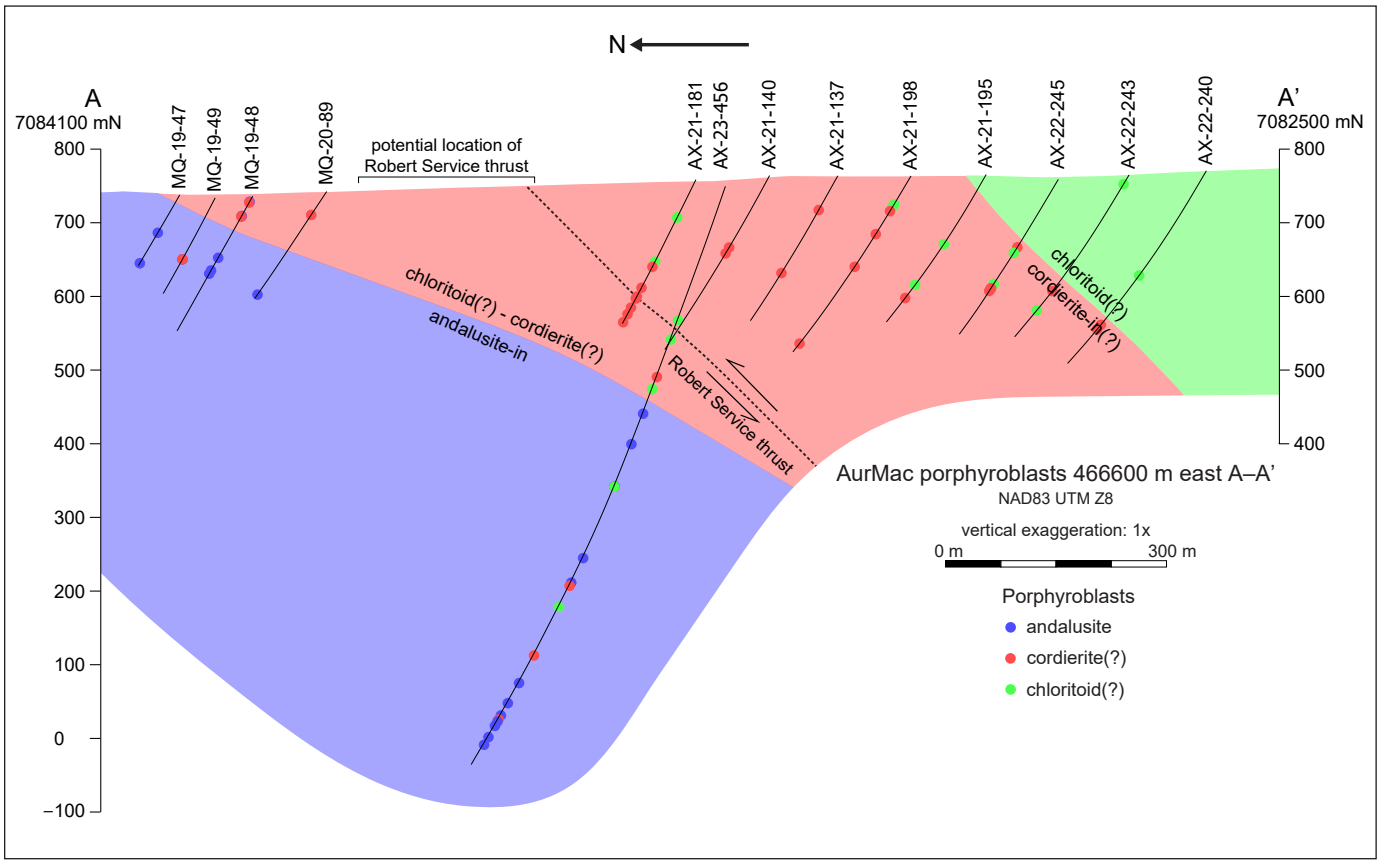

Figure 15. *Cross section A-A' along 466600 mE from 7084100 mN to 7082500 mN (UTM Zone 8) illustrating observed metamorphic isograds.*

Visible gold is common in vein-hosted mineralization, and is most often observed intergrown with fine-grained acicular and radiating lead-bismuth sulphosalts and less frequently in arsenopyrite aggregates. Reflected light petrography indicates that the majority of visible gold mineralization occurs as pyrrhotite–electrum–lead–bismuth sulphosalts ± chalcopyrite fracture fill in earlier sulphides and quartz (Fig. 18).

Alteration associated with vein mineralization consists of centimetre to metre-scale zones of silicification, sericitization, albitization and biotite-destructive bleaching. Due to the mineralogical variability in host rock metasedimentary rocks, distinguishing mineralization-related sericitization and silicification from metamorphic white micas in schists and more siliceous protoliths can be challenging.

Skarn

In the Airstrip deposit, and to a lesser extent in the Powerline deposit, gold mineralization occurs within pyrrhotite-bearing skarn horizons (Fig. 16b; Gray and Thom, 2021). The skarn horizons are characterized by massive to laminated textures, featuring relict foliation and compositional banding, and are composed of calcite, quartz, clinopyroxene, amphibole, garnet and scheelite, and sulphides generally comprise <10% of the assemblage. Sulphides consist predominantly of fine-grained to blebby disseminated to net-textured pyrrhotite with minor amounts of intergrown, very fine grained chalcopyrite (Fig. 19) and <1% early, fine-grained disseminated euhedral pyrite and arsenopyrite.

Lead-zinc-silver veins and breccias

Polymetallic silver-lead-zinc mineralization on the AurMac property is rare, typically presenting as sub-centimetre-scale veinlets and breccias, and crosscuts gold-bearing sheeted veins and skarns at the AurMac property.

Gangue minerals present in veins and breccias consist of siderite, quartz and calcite. Sulphide mineralization consists of sphalerite and galena, and accessory arsenopyrite, pyrite, chalcopyrite and pyrrhotite.

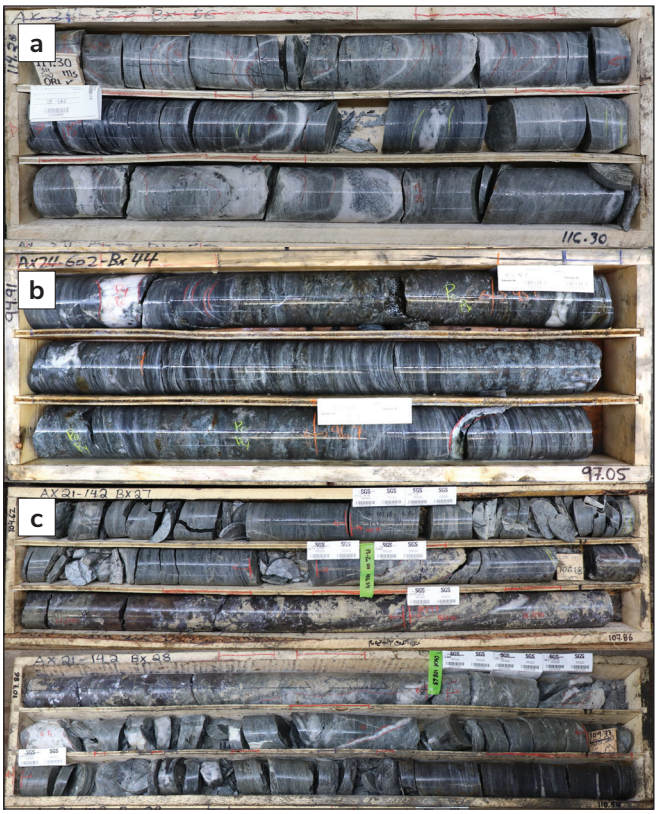

Figure 16. *Core photos from drillholes on the AurMac property. Core diameter is 71 mm (HTW).* ***(a)*** *Sheeted vein gold mineralization hosted in mica-quartz schist in drillhole AX-24-537.* ***(b)*** *Skarn mineralization in drillhole AX-24-602.* ***(c)*** *Semi-massive siderite–quartz–sphalerite–galena ± pyrite–arsenopyrite–pyrrhotite vein (75 cm true width) intersected in drillhole AX-21-142.*

This mineralization is believed to be analogous to that found in the Keno Hill silver district, which also hosts argentiferous tetrahedrite, native silver, and the silver-bearing sulphosalts polybasite, stephanite and pyrargyrite (Blais et al., 2024), although these minerals have yet to be identified in mineralization on the AurMac property.

In 2021, a 75 cm (true-width) semi-massive siderite–quartz–sphalerite–galena ± pyrite–arsenopyrite–pyrrhotite vein (Fig. 16c) was intersected in drillhole AX-21-142. The steeply east-southeast dipping vein strikes north with a dip and dip direction of approximately 80° toward 110°, and shares an attitude not dissimilar to vein orientations observed at the Bellekeno and Onek vein systems, Lucky Queen and Flame and Moth veins, and the Bermingham deposits of the Keno Hill silver district (Blais et al., 2024).

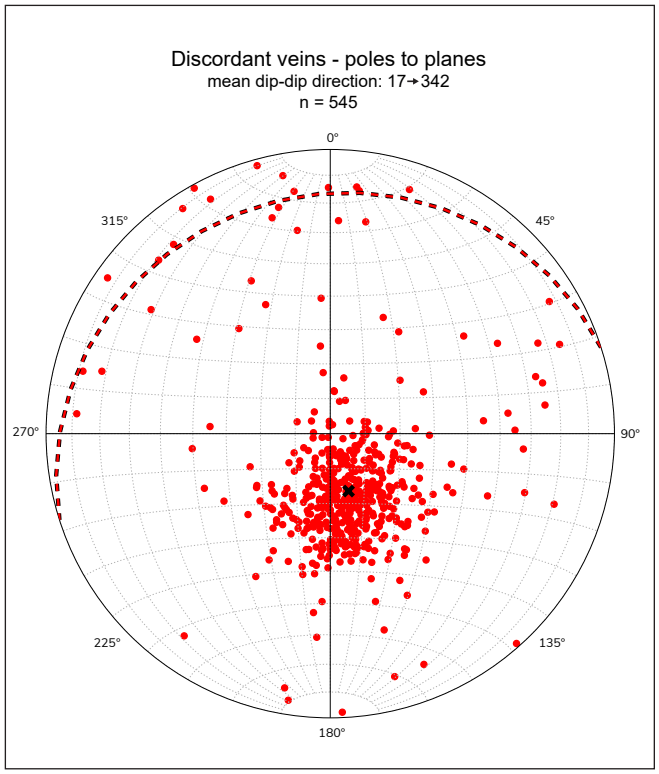

Figure 17. *Stereonet depicting poles-to-planes of shallowly north-dipping gold-bearing sheeted veins.*

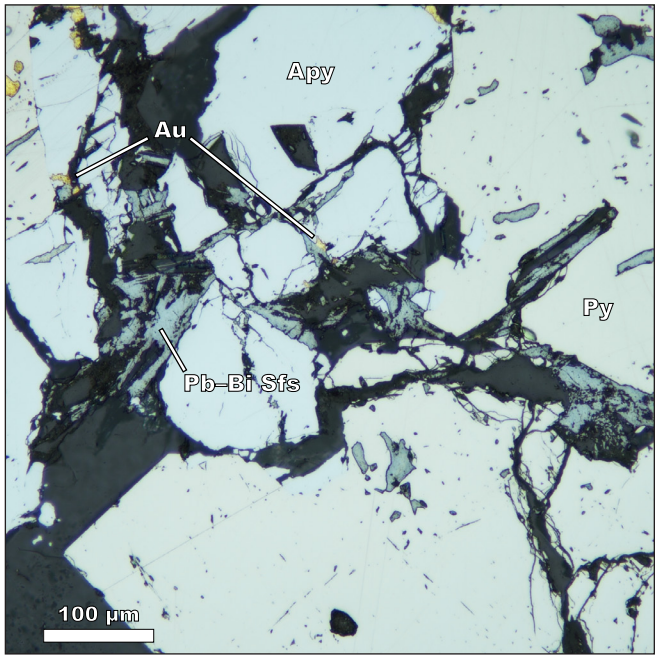

Figure 18. *Reflected light photomicrograph of lead-bismuth sulphosalts (Pb-Bi Sfs) and electrum (Au) as fracture fill in arsenopyrite (Apy) and pyrite (Py).*

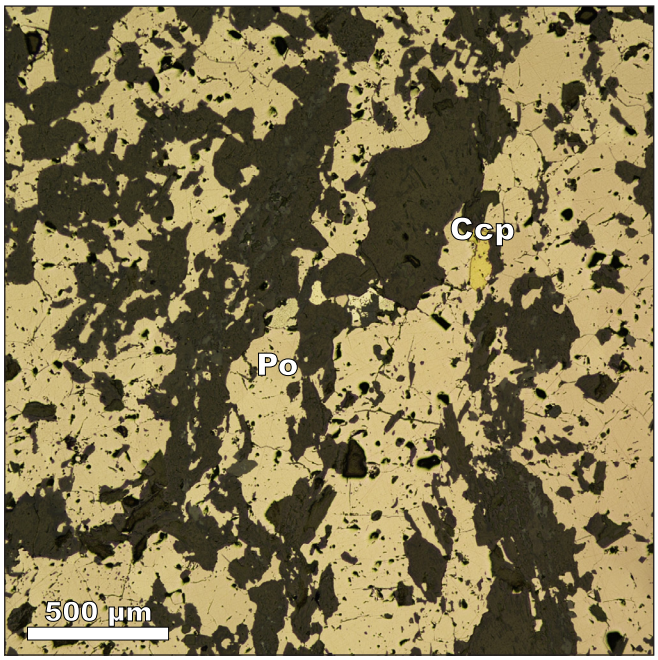

Figure 19. *Reflected light photomicrograph of sulphide-bearing skarn composed of net-textured pyrrhotite (Po) and chalcopyrite (Ccp) surrounding a quartz and feldspar matrix.*

Evidence for RIRGS-style mineralization

Although an underlying intrusion has yet to be identified at the AurMac deposits, gold mineralization observed on the property exhibits characteristics typical of intrusion-hosted RIRGS, similar to those at the nearby Dublin Gulch property. At the Powerline deposit, gold is hosted in sulphide-poor, centimetre-scale, sheeted quartz veins and is strongly associated with bismuth, which parallels the mineralization style at Dublin Gulch. Both deposits also share a sulphide assemblage including arsenopyrite, pyrite, pyrrhotite, pyrite, sphalerite and bismuth-bearing minerals (Harvey et al., 2023). Furthermore, a spatial relationship with skarn horizons, as seen in at the Wolf Skarn deposit proximal to the Dublin Gulch pluton, closely resembles the Airstrip deposit at the AurMac property, suggesting the potential presence of an unidentified intrusion on, or near the AurMac property (Kirk, 2016). The progressive increase in metamorphic grade observed in porphyroblasts through the outlined section, from chloritoid to cordierite and andalusite (Figs. 6, 14), also supports the presence of a potential heat source situated north of the Airstrip zone. Given these observations, and that mineralization in known RIRGS is typically hosted within the carapace and surrounding hornfels of intrusions (Hart, 2007), the AurMac property demonstrates considerable potential for the discovery of intrusion-hosted mineralization. AurMac deposits also highlight the existence of large-scale, bulk-tonnage, sediment-hosted intrusion-related gold systems, which may occur elsewhere in the region.

References

Abbott, G., 1997. Geology of the upper Hart River area, eastern Ogilvie Mountains, Yukon Territory (116A/10, 116 A/11). Exploration and Geological Services Division, Yukon, Indian and Northern Affairs Canada, Bulletin 9, 92 p.

Anders, E. and Grevesse, N., 1989. Abundances of the elements: Meteoritic and solar. Geochimica et Cosmochimica Acta, vol. 53, no. 1, p. 197–214.

Blais, J., Muñoz, M., Vink, C., Baoyao, T. and Blattman, M., 2024. NI 43-101 Technical Report on the Keno Hill Mine, Yukon, Canada. NI 43-101 technical report prepared by Mining Plus Canada Consulting Ltd. for Hecla Mining Company. Submitted March 28, 2024, 313 p. https://www.sedarplus.ca/csa-party/records/document.html?id=173ac1c40d3944929606358b4a9f7372659b9c053818a9e1b651696c43af59e1 [accessed 2024/11/27].

Colpron, M., Logan, J.M. and Mortensen, J.K., 2002. U–Pb zircon age constraint for late Neoproterozoic rifting and initiation of the lower Paleozoic passive margin of western Laurentia. Canadian Journal of Earth Sciences, vol. 39, no. 2, p. 133–143.

Gabrielse, H., Murphy, D.C., Mortensen, J.K., Haggart, J.W., Enkin, R.J. and Monger, J.W.H., 2006. Cretaceous and Cenozoic dextral orogen-parallel displacements, magmatism, and paleogeography, north-central Canadian Cordillera. *In*: Paleogeography of the North American Cordillera: Evidence for and against large-scale displacements, J.W. Haggart, R.J. Emskin and J.W.H. Monger (eds.), Geological Association of Canada Special Paper 46, p. 255–276.

Gordey, S.P. and Anderson, R.G., 1993. Evolution of the northern Cordilleran miogeocline, Nahanni map area (105I), Yukon and Northwest Territories. Geological Survey of Canada Memoir, no. 428, 214 p.

Gray, P. and Thom, J., 2021. Yukon Mineral Exploration Program (YMEP) final report for a 2020 Target Evaluation Program on the AurMac Property. Yukon Mineral Exploration Program (YMEP) Report 2020-14, 305 p.

Hart, C.J.R., 2007. Reduced intrusion-related gold systems. In: Mineral Deposits of Canada: A synthesis of major deposit types, district metallogeny, the evolution of geological provinces, and exploration methods, W.D. Goodfellow (ed.), Geological Association of Canada, Mineral Deposits Division, Special Publication No. 5, p. 95–112.

Hart, C.J., Baker, T. and Burke, M., 2000. New exploration concepts for country-rock-hosted, intrusion-related gold systems: Tintina gold belt in Yukon. In: The Tintina gold belt: concepts, exploration and discoveries, Special Volume 2, T.L. Tucker and M.T. Smith (eds.), British Columbia and Yukon Chamber of Mines, p. 145–172.

Hart, C.J., Mair, J.L., Goldfarb, R.J. and Groves, D.I., 2004. Source and redox controls on metallogenic variations in intrusion-related ore systems, Tombstone-Tungsten belt, Yukon Territory, Canada. Earth and Environmental Science Transactions of The Royal Society of Edinburgh, vol. 95, no. 1–2, p. 339–356.

Harvey, N., Gray, P., Winterton, J., Jutras, M. and Levy, M., 2023. Technical Report, Eagle Gold Mine, Yukon Territory, Canada. NI 43-101 technical report prepared by Victoria Gold Corporation. Submitted April 10, 2023, 333 p. https://www.sedarplus.ca/csa-party/records/document.html?id=952a15f1d0fd09d99049027e54d871659b037d1767177f2a6a6e111fed8019f6 [accessed 2024/11/27].

Kirk, A., 2016. Paragenesis, geochemistry and metallogeny of the Dublin Gulch intrusion-related Au deposit, Yukon Territory. Unpublished MSc thesis, Memorial University, Newfoundland, Canada, 362 p.

Mair, J.L., Hart, C.J. and Stephens, J.R., 2006. Deformation history of the northwestern Selwyn basin, Yukon, Canada: Implications for orogen evolution and mid-Cretaceous magmatism. Geological Society of America Bulletin, vol. 118, no. 3–4, p. 304–323.

McOnie, A., 2016. The Keno Hill silver mining district. GAC-MAC 2016 Whitehorse Field Trip Guide Book, 69 p. and 2 maps.

Mortensen, J.K. and Thompson, R.I., 1990. A U-Pb zircon-baddeleyite age for a differentiated mafic sill in the Ogilvie Mountains, west-central Yukon Territory. Geological Survey of Canada Paper 89-02, p. 23–28.

Murphy, D.C., 1997. Geology of the McQuesten River region, northern McQuesten and Mayo map areas, Yukon Territory (115P/14, 15, 16, 105M/13, 14). Exploration and Geological Services Division, Yukon, Indian and Northern Affairs Canada, Bulletin 6, 122 p.

O'Dea, M., Carlson, G., Harris, S., Fields, M., Tucker, T.L. and Smith, M.T., 2000. Structural and metallogenic framework for the Scheelite Dome deposit, Yukon Territory. *In*: The Tintina gold belt: concepts, exploration, and discoveries, Special Volume 2, T.L. Tucker and M.T. Smith (eds.), British Columbia and Yukon Chamber of Mines, Cordillera Roundup January 2000, p. 115–130.

Pearce, J.A., 1996. A user's guide to basalt discrimination diagrams. *In*: Trace Element Geochemistry of Volcanic Rocks: Applications for Massive Sulphide Exploration, D.A. Wyman (ed.), Geological Association of Canada, Short Course Notes 12, p. 79–113.

Rasmussen, K.L., 2013. The timing, composition, and petrogenesis of syn- to post-accretionary magmatism in the northern Cordilleran miogeocline, eastern Yukon and southwestern Northwest Territories. Unpublished PhD thesis, University of British Columbia, British Columbia, Canada, 788 p.

Read, P., McOnie, A. and Iles, S., 2020. Geology of the Keno Hill district. Yukon Geological Survey, Open File 2020-42, 2 sheets, scale 1:25 000 and 1:2500.

Roots, C.F. and Abbott, G., 1988. Cambro-Ordovician volcanic rocks in the eastern Dawson map area, Ogilvie mountains, Yukon. *In*: Yukon Geology Volume 2, J.G. Abbott (ed.), Exploration and Geological Services Division, Indian and Northern Affairs Canada, p. 81–87.

Skipton, D. and Maw, L., 2021. Updated geology of the Clark Lakes area in central Yukon (parts of 106D/2, 3, 6 and 7). *In*: Yukon Exploration and Geology 2020, K.E. MacFarlane (ed.), Yukon Geological Survey, p. 73–94.

Stephens, J.R., Oliver, N.H.S., Baker, T. and Hart, C.J.R., 2000. Structural evolution and controls on gold mineralization at Clear Creek, Yukon. *In*: Yukon Exploration and Geology 1999, D.S. Edmond and L.W. Weston (eds.), Exploration and Geological Services Division, Yukon Region, Indian and Northern Affairs Canada, p. 151–163.

Stephens, J.R., Mair, J.L., Oliver, N.H., Hart, C.J. and Baker, T., 2004. Structural and mechanical controls on intrusion-related deposits of the Tombstone Gold Belt, Yukon, Canada, with comparisons to other vein-hosted ore-deposit types. Journal of Structural Geology, vol. 26, no. 6–7, p. 1025–1041.

Sun, S.S. and McDonough, W.F., 1989. Chemical and isotopic systematics of oceanic basalts: Implications for mantle composition and processes. Geological Society of London, Special Publications, no. 42, p. 313–345.

Thornton, T., Jutras, M. and Malhotra, D., 2024. Technical Report, AurMac Property, Mayo Mining District, Yukon Territory, Canada. NI 43-101 technical report prepared by JDS Energy & Mining Inc. for Banyan Gold Corporation. Submitted March 18, 2024, 327 p., https://www.sedarplus.ca/csa-party/records/document.html?id=c2f3326a6bbde1f106d51acaacea522b6d8df8c921d6104b0f1d085c25bd0574 [accessed 2024/11/27].

Yukon Geological Survey, 2020. A digital atlas of terranes for the northern Cordillera. Yukon Geological Survey, https://data.geology.gov.yk.ca/Compilation/2 [accessed 2024/09/19].

Yukon Geological Survey, 2022. Yukon Digital Bedrock Geology. Yukon Geological Survey, https://data.geology.gov.yk.ca/Compilation/3 [accessed 2024/09/19].

Yukon Geological Survey, 2023a. Yukon Geochronology – A database of Yukon isotopic age determinations. Yukon Geological Survey, https://data.geology.gov.yk.ca/Compilation/22 [accessed 2024/09/19].

Yukon Geological Survey, 2023b. Yukon Lithogeochemistry data set. Yukon Geological Survey, https://data.geology.gov.yk.ca/Compilation/35 [accessed 2024/09/19].

Thermal imagery and lidar monitoring of ground instability on the Alaska Highway, southwestern Yukon

*Justin Roman and John Stix**
Department of Earth and Planetary Sciences, McGill University

Margaret Kalacska and Oliver Lucanus
Applied Remote Sensing Laboratory (ARSL), Department of Geography, McGill University

Pablo Arroyo-Mora
National Research Council of Canada, Flight Research Laboratory

Panya Lipovsky
Yukon Geological Survey

Roman, J., Stix, J., Kalacska, M., Lucanus, O., Arroyo-Mora, P. and Lipovsky, P.S., 2025. Thermal imaging and lidar monitoring of ground instability on the Alaska Highway, southwestern Yukon. *In*: Yukon Exploration and Geology Technical Papers 2024, L.H. Weston, A. Stuart, S.K. Schultz, A.D. Brubacher and D.C. Cronmiller (eds.), Yukon Geological Survey, p. 41–50.

Abstract

Permafrost is integral to the landscape of the Yukon, and influences hydrology and ecology, and impacts infrastructure. Accelerated permafrost thaw due to climate change poses significant challenges, particularly for the Alaska Highway, a vital transportation route. This study investigates how thawing permafrost may relate to ground instability, resulting in cracks and deformations along the highway. Thermal infrared imaging, and light detection and ranging (lidar) mounted on remotely piloted aircraft systems (RPAS), along with ground surveys, were completed at three localities along the Alaska Highway between the White River and the community of Beaver Creek, Yukon. Through these surveys, temperature variations and topographic changes were examined. At many locations, the damage is characterized by a 1 to 2 m-wide subsidence feature running longitudinally along the middle of the highway. Associated with these zones of subsidence are potholes, as well as longitudinal and transverse cracks. In places, the system of cracks extends to the edge and shoulder of the highway, suggesting that the cracks and deformation are currently active features.

Plain language summary

To better understand the damage to a part of the Alaska Highway in the Yukon caused by permafrost thaw, a series of drone-based surveys were conducted along the highway between the White River and the community of Beaver Creek. Three sites were surveyed where road damage is extensive; two sites had various engineered structures installed to help dissipate heat in the shallow subsurface, whereas the third site did not have any such structures. Drone-based thermal infrared imaging and lidar surveys were used to map the detailed thermal and topographic expression of the road surface, and each site was also surveyed on the ground. In the central part of the road, where damage was obvious, the surveys mapped a principal depression roughly parallel to the highway, containing more localized and deeper depressions that were slightly cooler than the surrounding road surface. Drone-based surveys offer rapid and cost-effective means of surveying and assessing critical infrastructure such as highways.

* john.stix@mcgill.ca

Introduction

Permafrost, the layer of permanently frozen ground that persists year-round in polar and subpolar environments, constitutes much of the Yukon landscape. As a defining feature of northern environments, permafrost is essential to the stability of soils and ecosystems in this region. As global temperatures rise, northern regions of Canada, including the Yukon, are experiencing increasingly rapid permafrost degradation, posing significant challenges to the environment, ecosystems, and local communities. Although permafrost thaw is a natural phenomenon, the current accelerated rates of warming have intensified this process, causing ground instability and enhanced erosion. Permafrost thaw is currently causing landslides (e.g., Patton et al., 2021), impacting groundwater systems (e.g., Wiebe et al., 2024), enhancing riverbank erosion (e.g., Geyman et al., 2024), and affecting infrastructure such as pipelines, roads and buildings (e.g., Hjort et al., 2022).

In the Yukon, permafrost conditions (i.e., thickness, ice content and temperature) vary widely within the continuous, discontinuous and sporadic permafrost zones (Lipovsky et al., 2022). This variation, combined with local factors such as variations in surficial materials and ground ice distribution, leads to complex patterns of thaw and associated ground movement. The effect of permafrost degradation on infrastructure, particularly in regions with discontinuous permafrost, is highly unpredictable without detailed geotechnical investigations. Roads, buildings and pipelines rely on stable ground for safety reasons. As the frozen ground thaws, it can no longer support the weight above, resulting in sinkholes, ground subsidence, thermokarst features (Jorgenson, 2022), and differential settling in areas where ground ice content is not uniform. This instability is a critical concern for the Alaska Highway, which serves as an essential transportation corridor linking communities in southern Canada and Alaska. Along the Yukon segment of the Alaska Highway, ground instability caused by permafrost thaw is manifested as cracks and dips in the road surface, endangering drivers and requiring costly and frequent repairs to the highway. The section of the highway between the White River and the community of Beaver Creek is particularly vulnerable due to a combination of permafrost and buried glacial ice (Calmels et al., 2015) near the last (McConnell) glacial limit (Bond et al., 2008).

Conventional methods for assessing ground stability, such as manual surveys, are limited in their ability to monitor changes over large, remote areas where these methods do not easily capture subsurface thermal changes. As a result, there is an urgent need for innovative approaches that can efficiently and accurately assess permafrost stability across different and challenging landscapes.

The principal objective of this study was to assess the surface conditions of the road at several sites along the Alaska Highway (Fig. 1). To do this, two surveys were completed to evaluate the road surface: thermal infrared imaging, and light detection and ranging (lidar) mounted on remotely piloted aircraft systems (RPAS). By combining the thermal infrared and lidar datasets, this study offers a novel means of quantifying permafrost-related ground instability. This approach not only highlights current areas of concern but also establishes a baseline for monitoring future changes.

Methodology

Study area

Three areas along the Alaska Highway between the White River and the community of Beaver Creek were selected as study areas (Fig. 1). The areas that were selected are part of a section of the Alaska Highway that is in relatively poor condition, and road degradation is characterized by deformation and features such as potholes, longitudinal cracks, and dips on the road surface. Study Area A (KM 1841) is situated at 'the Dry Creek site location' where the Yukon Department of Highways and Public Works (HPW) has installed a series of thermosiphons to help dissipate heat and protect ice-rich permafrost in the shallow subsurface (Reimchen et al., 2009; SRK Consulting, 2018). Study Area B (KM 1865) is located 5 km south of the community of Beaver Creek and is a second highly engineered site. Since 2008, various heat dissipation mitigation techniques have been monitored to determine which configuration is most efficient and cost effective (Doré et al., 2005; López et al., 2024). Study Area C (KM 1862.5) is a section of badly damaged road without engineering mitigations, located 2.5 km south-southeast of Study Area B.

Remotely piloted aircraft systems (RPAS) instrumentation

This study used thermal infrared imaging and lidar deployed on remotely piloted aircraft systems (RPAS), colloquially referred to as drones. The use of RPAS equipped with thermal infrared cameras enabled a non-intrusive examination of the surface, targeting

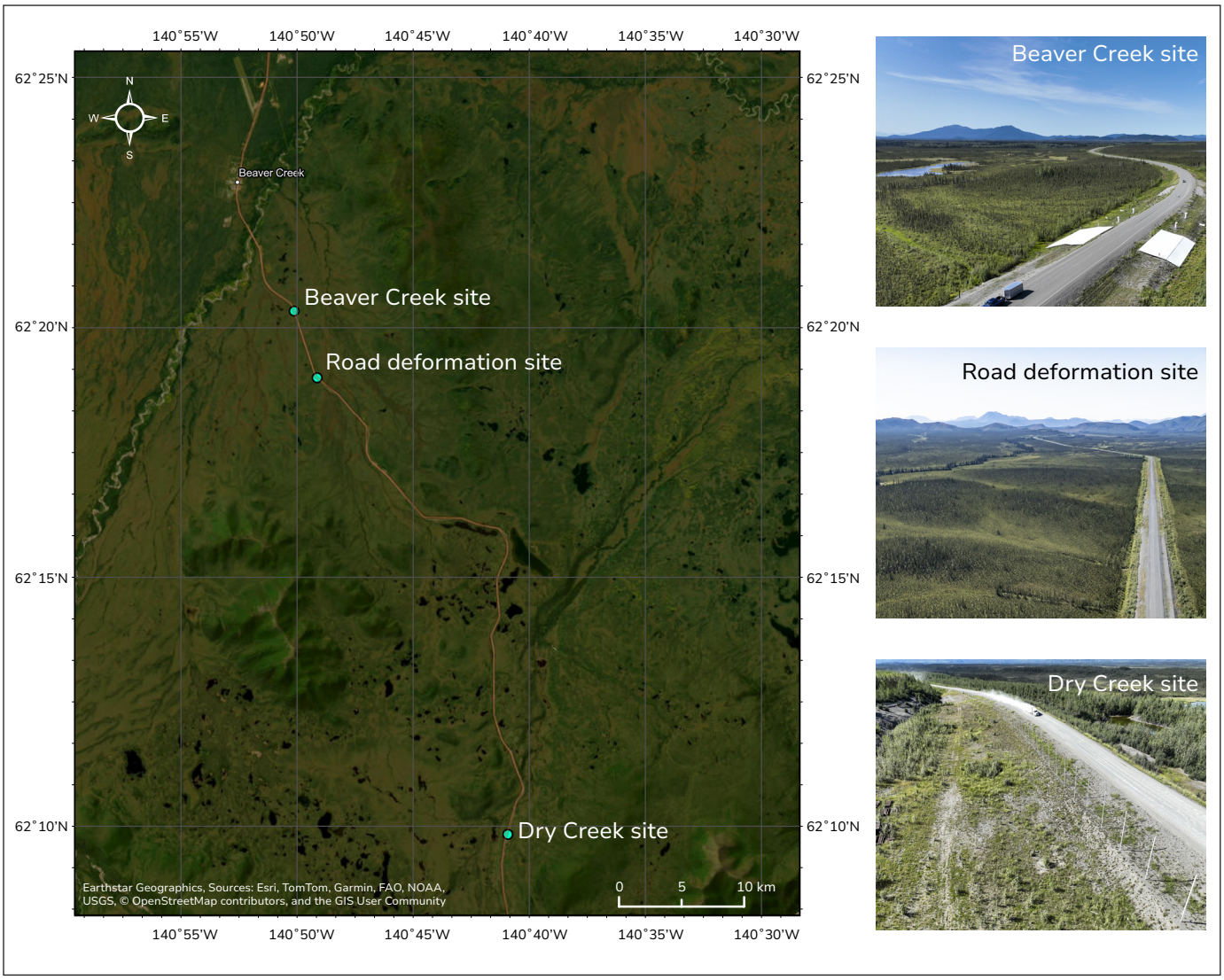

***Figure 1**. Regions of interest along the Alaska Highway (Study Area A: Dry Creek site; Study Area B: Beaver Creek site; Study Area C: Road deformation site).*

potential hotspots. Lidar provided a high-resolution 3D representation of the surface topography, allowing for precise detection of structural deformations, including depressions, potholes and cracks. Together, these technologies provide a comprehensive approach to analyze both the thermal and topographic properties of the ground surface.

Thermal infrared imaging

The thermal infrared imaging study was designed to collect data at night to minimize interference from solar heating, which makes inferences about the thermal emission of the ground surface difficult. By collecting thermal infrared imagery during the night, the analysis of temperature variations becomes more accurate. The thermal imaging data were collected using two RPAS equipped with different thermal infrared cameras. These cameras operate in the longwave infrared range, recording radiation emitted from the ground.

The first thermal camera was a DJI H20T, with a wavelength range of 8 to 14 µm, flown 45 m above ground level onboard a DJI M300RTK RPAS. The second, a DJI Zenmuse XT-R, with a wavelength range of 7.5 to 13.5 µm, was flown 25 m above ground level onboard a DJI M100 RPAS. Thermal infrared images were captured at regular intervals along each path. The different flight altitudes were selected to provide a series of images with different and complementary

spatial resolutions. The RPAS were flown along predefined flight paths using flight control software (DJI Pilot 2 for the M300 and Pix4D Capture for the M100). The M300 flights covered a series of 11 to 12 overlapping flight paths with 80% front and sidelap to ensure full coverage of the study areas, whereas the M100 flights covered smaller and more focused areas. For the M100, flight number 1 was performed at Study Area A, flown 55 m above ground level, and an area of 206 by 114 m was surveyed, creating five parallel lines. Flight number 2 at Study Area B was sectioned into two separate flights, both flown 25 m above ground level. The first flight flew parallel to the road, creating four parallel lines, and the second flight flew perpendicular to the road, creating six parallel lines. Flight number 3 at Study Area C flew two lines parallel to the road, and were 25 m above ground level.

Lidar survey

To complement the thermal infrared data, lidar was acquired to capture detailed topographic information across the study areas. Lidar technology uses pulses of light from a laser to generate precise 3D measurements of surface features by calculating the return time of each pulse. Lidar has the potential to identify and quantify temporal changes in topography, such as surface subsidence or the formation of cracks, which are characteristic of ground instability seen on the Alaska Highway. In this study, a DJI L1 lidar system was used, mounted on the DJI M300 RPAS. Flown at 70 m above ground level, 7 to 10 parallel flight lines (50% overlap) were needed at each of the three sites. Repeat surveys will be performed in the summer of 2025 to detect any changes to the road surface of the highway.

Ground truthing

For each study area, a detailed ground survey was conducted, noting important features such as cracks, areas of subsidence, potholes and drainage zones. Photographs were taken of key representative features, and the locations of these features were marked at each site.

Data analysis

A preliminary analysis was conducted of the thermal infrared, lidar and ground survey data collected in August 2024. These results are presented below, including a focus on Study Area B. In the future, a quantitative comparison will be made between the thermal infrared and lidar data collected in the summers of 2024 and 2025 for the three study areas. A comprehensive analysis of the data will also be conducted, whereby the thermal infrared images will be overlain onto a 3D lidar model to create a unified visualization of conditions along the highway. This integration will allow for a comparative analysis, where zones of thermal differences may be examined alongside corresponding topographic changes.

Results

A preliminary examination of the thermal infrared images and lidar data collected in August 2024 reveals potential indicators of permafrost-related ground instability. Although further quantitative analysis is necessary, an initial visual inspection suggests a correspondence between observed ground deformations and temperature anomalies.

The thermal infrared image presented in Figure 2 was obtained on August 9, 2024, from Study Area B using the XT-R camera. The red to white colours represent the road, whereas the darker colours correspond to the embankment and an open area beyond, which are several degrees cooler. Due to the adjustment of the image's emissivity for asphalt (ε = 0.93; Engineering Toolbox, 2024) to highlight variations in the road surface, the temperature displayed for the vegetation (which generally has an emissivity closer to 0.98) appears cooler than it actually is. The road surface is thermally heterogeneous. A main central depression is well displayed, characterized by numerous lineations that are parallel to subparallel to the road. These lineations represent fractures and cracks. The warmest areas of the road surface tend to be on either side of the central depression, although warm temperatures are also present within the depression itself. Small potholes within the depression are well displayed and are slightly cooler than the rest of the depression.

The lidar point cloud density ranged from 30 to 230 pts/m^2. Lidar data from the same locality as the thermal infrared imagery discussed above also reveals a central area of the road surface containing irregular features (Fig. 3). The main longitudinal depression feature, having a depth of 10 to 15 cm and width of 1 to 3 m, is clearly present in at least two areas of the point cloud. Within the depression, a series of smaller, darker features represent potholes and other locally deeper areas of the depression. The two cross sections contrast a 37 cm vertical difference in cross section A, and a 16 cm vertical difference in cross section B. Cross section A traverses one of the larger local depressions.

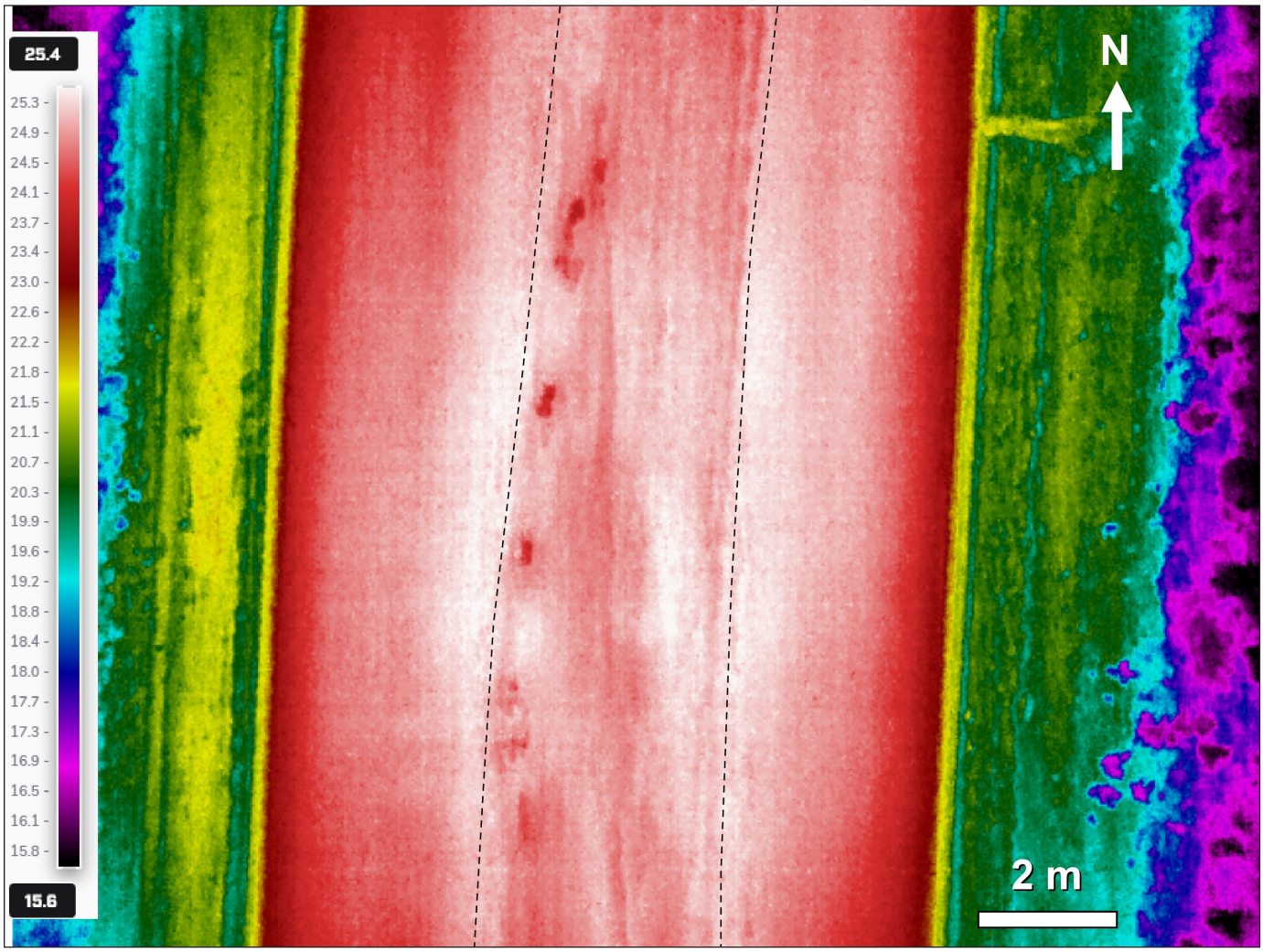

***Figure 2**. Thermal infrared image from the road deformation site acquired with the XT-R thermal camera from 25 m above ground level, indicating pronounced thermal heterogeneity in the middle section of the road corresponding with the irregular surface topography displayed in Figure 3. The black dashed lines define the main central depression. The red anomalies within the depression correspond to local depressions such as potholes. The left side of the diagram includes temperatures in degrees Celsius and the corresponding colours that are depicted on the image. Analytical parameters used: emissivity 0.93, air temperature 17˚C, external optics temperature 17˚C, reflected temperature -50˚C, relative humidity 69%, and distance 25 m. Note: to prioritize the highway, the emissivity was set to 0.93 (general estimate for asphalt) and other materials with higher emissivity such as vegetation, will be underestimated in temperature.*

Areas where thermal infrared imaging indicated lower temperatures appear to correspond with locally deep areas such as potholes in the lidar point cloud. These observations align with findings from Throop et al. (2012), who suggest that there may be similar spatial relationships between ground temperature changes and topographic changes in other permafrost landscapes.

Ground truthing information was collected at all three study areas (Fig. 1), including detailed ground surveys of each area, enabling detailed observations of the road surface. Figures 4 and 5 demonstrate the magnitude and variability of the road deformation at Study Area B, such as cracks and potholes within larger depression features. These features are all observed on the thermal infrared imagery and lidar point cloud. Other observations include features along the side of the road, such as cracks and drainage zones. These features may help to identify specific areas of weakness along the highway.

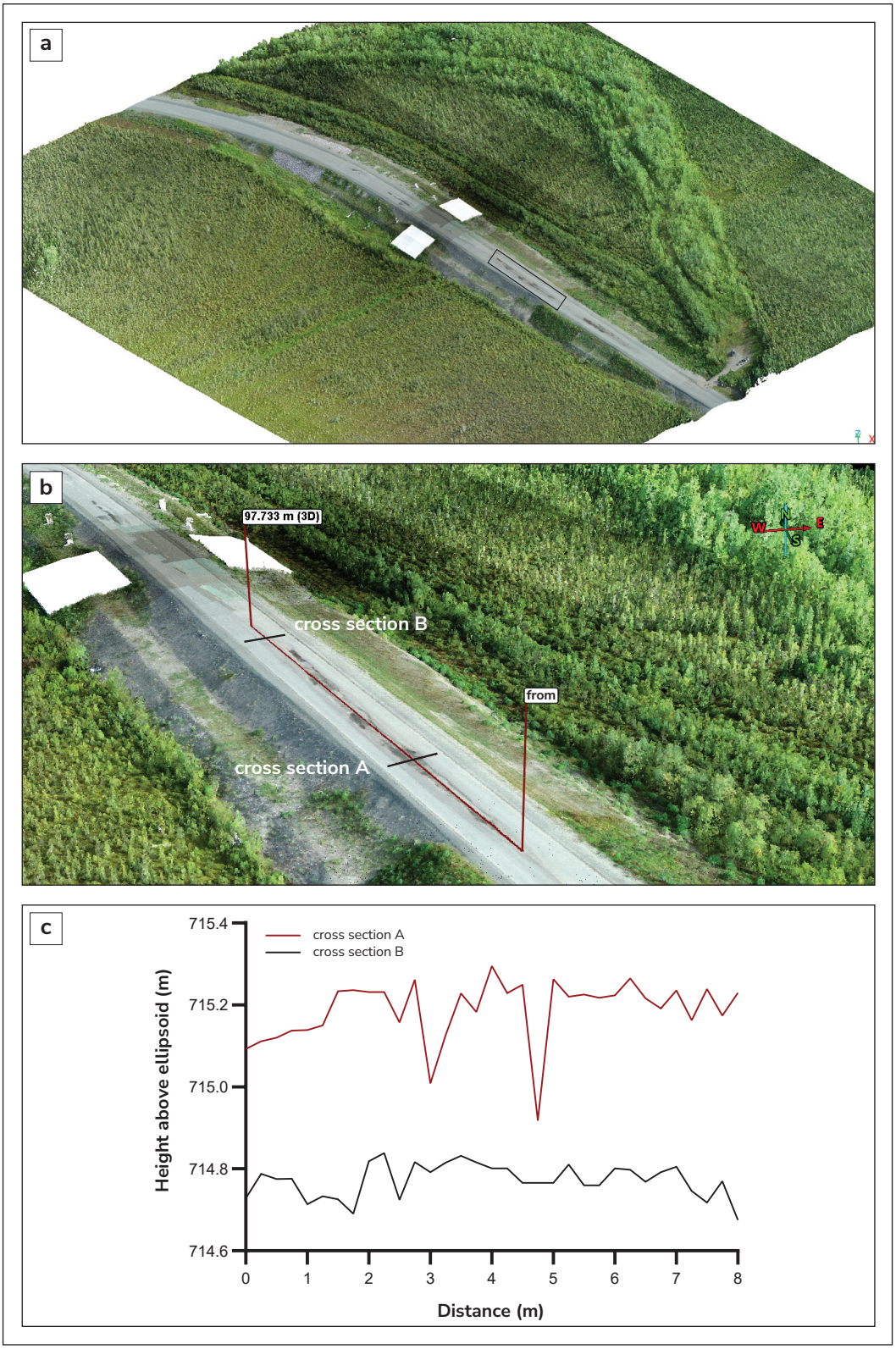

Figure 3. *Lidar point cloud from Study Area B.* ***(a)*** *Overview of the 650 by 350 m area. The black rectangle is the area visible in (b);* ***(b)*** *Close-up view of the highway with a 97.7 m centreline across which 8 m cross sections were extracted. Cross section B does not show major surface deformation. Cross section A traverses the central depression on the highway.* ***(c)*** *Elevation across the two cross sections at a resolution of 25 cm. Cross section A has a vertical difference of 37 cm, and cross section B has a vertical difference of 16 cm.*

Figure 4. *Site survey of Study Area B indicating a longitudinal depression in the central part of the highway (brown area), as well as potholes and other local depressions.*

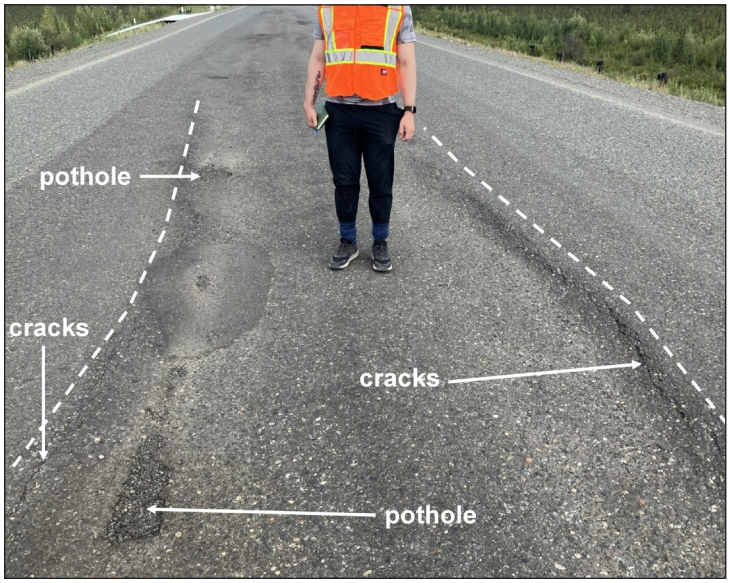

Figure 5. *Close-up view of road deformation in Study Area B. A central depression feature is visible (outlined by the dashed white lines), along with potholes and cracks, which define the margins of the depression.*

Discussion

This study used thermal infrared imaging and lidar to investigate ground instability along the Alaska Highway. Although this preliminary analysis was largely qualitative, some early results provide insights into the spatial relationship between surface deformations and temperature differences. The correspondence between ground temperatures and surface deformation, as seen from the thermal infrared and lidar point cloud, suggests that ground instability may be driving structural weaknesses along the highway. This discussion explores the implications of these observations, the strengths and limitations of the methods used, and the potential for future research to refine these initial findings.

One of the primary observations from the thermal infrared imaging data is the presence of subtle temperature anomalies in road sections that exhibit visible depressions and cracks. The slightly cooler zones such as potholes in the middle of the highway may indicate that heat dissipation is enhanced from irregular ground that is broken, fractured and deformed in these central areas. In an earlier study at Study Area A, de Grandpré et al. (2012) found a similar central road subsidence was due to groundwater flow. They concluded that permafrost degradation under the damaged road surface was due partly to the road construction and ongoing maintenance, as well as the road cross-cutting the natural groundwater drainage. The comparable surface deformation features and area topography found at Study Area B suggest the causes may be similar.

The thermal infrared image in Figure 2 indicates that the areas of maximum highway damage, as manifested by relatively deep potholes, are reflected by slightly lower temperatures relative to the rest of the road surface. These preliminary results suggest that thermal infrared imaging may serve as a sensitive and early indicator of highway damage. Such surface changes can be valuable for identifying sections of the highway where more thorough investigations may be needed that penetrate deeper in the subsurface. This information could be crucial for road maintenance teams in prioritizing repairs in areas that are most at risk of further thawing.

Lidar data can complement thermal infrared data by providing a precise, high-resolution micro-

topographic view of the road surface. In this study, lidar data revealed cracks and other deformations along a central depression structure on the Alaska Highway (Fig. 3). Further spatial analysis of the point clouds will likely reveal that surface deformations are not uniform, but vary significantly in size and distribution, with certain areas displaying more pronounced instability than others. These can be particularly interesting in the context of highway management because the work can be focused on high-risk areas. These variations may be linked to differences in local permafrost conditions, soil composition or drainage patterns, all of which can influence how thaw affects ground stability (de Grandpré et al., 2012).

The use of RPAS-based lidar appears to be advantageous for monitoring a focused section of the highway. Unlike ground-based survey methods, which can be time-consuming and limited in scope, RPAS-mounted lidar allows for rapid assessment of surface changes across the study area. A typical survey takes less than 30 minutes for an area of 650 by 350 m. This capability is particularly useful for monitoring infrastructure in remote northern regions, where field access may be limited. By capturing detailed topographic data over time, lidar can help track the progression of ground instability, identify areas where deformation is increasing and support proactive maintenance strategies.

Several limitations of this study should be noted. First, the analysis was limited to surface observations, and without subsurface measurements, the exact depth and extent of permafrost thaw is uncertain. Borehole data from the Yukon Geological Survey's permafrost database could complement these surface observations by providing a clearer picture of subsurface conditions and analysis (Douglas et al., 2021). Incorporating subsurface data would also help validate the thermal anomalies observed. Field-based validation of the surface temperature would allow further refining of the estimate of emissivity for the asphalt under various surface conditions. This would ensure a more accurate estimate of the surface temperature.

Additionally, seasonal variations in ground temperatures may be important (Douglas et al., 2021). Conducting thermal infrared imaging during the different seasons would provide a more comprehensive dataset to capture any seasonal variability that may be present. Repeating the lidar over similar time intervals could also enable a more robust assessment of the rate and extent of surface deformation over time, supporting an analysis on the impacts permafrost may have on the highway, and the degradation in the permafrost caused by the presence of the highway.

Lastly, the preliminary observations suggest a correspondence between thermal anomalies and surface deformations, but further quantitative analyses are necessary to establish a definitive link. These analyses could also be expanded to assess how different factors, such as soil type, moisture content and vegetation cover, influence the observed patterns of temperature and deformation, providing a more nuanced and in-depth understanding of permafrost dynamics and ground instability.

Concluding remarks and future work

As climate change continues to affect the Yukon, understanding the consequences of such change and its effects on the landscape will be crucial for building resilience. The Alaska Highway, like many structures in northern Canada, will increasingly require proactive measures for maintenance and adaptation to minimize risks associated with permafrost thaw. By identifying vulnerable sections of the highway and contributing to models for permafrost thaw, this research can help support the development of mitigation strategies. These strategies may include using materials and engineering techniques adapted to shifting ground conditions, such as thermosiphons, as well as developing early-warning systems to monitor temperature and ground movement in critical areas.

This research is significant for several reasons. First, it contributes to a deeper understanding of permafrost dynamics specific to the Yukon, where permafrost conditions are highly variable and sensitive to environmental change. Second, by focusing on the Alaska Highway, this study addresses challenges for a major transportation corridor that has great economic importance for the region. Ground instability along this highway disrupts not only local travel, but also broader supply chains that extend into the Yukon and beyond. Finally, the use of RPAS technology represents an innovative step in monitoring infrastructure in permafrost regions. These tools offer practical advantages over conventional methods, providing safer, more efficient and more extensive coverage for these types of areas.

This study provides preliminary insights into the use of thermal infrared imagery and lidar to assess permafrost-related ground instability along a segment of the Alaska

Highway in the Yukon. Although quantitative analysis is pending, initial observations indicate a correspondence between ground temperatures and surface deformations. These findings suggest that thermal changes could serve as early indicators of road damage and possibly permafrost thaw, whereas lidar can effectively capture the physical surface characteristics of this instability. Together, these techniques offer a promising approach to identifying and monitoring areas of infrastructure vulnerability in permafrost regions.

Future work is three-fold:

1. The three sites along the Alaska Highway will be resurveyed in summer 2025, to compare with the 2024 results, and to observe any changes that may have occurred on the road surface over the course of a year.
2. A detailed analysis of the thermal infrared imagery and lidar data will be completed to examine any differences in a quantitative fashion.
3. Since landslides are common features in the Yukon (e.g., Huscroft et al., 2004), a new demonstration project will be initiated in July 2025 using an automated drone system, the DJI Dock 2, to observe and monitor the unstable Miles Ridge landslide area near Koidern and the White River. This active landslide area is very close to the Alaska Highway, hence is cause for concern. Daily automated RPAS missions will be conducted of the landslide using visual and thermal infrared cameras during the summer from July to September.

Acknowledgments

The authors are extremely grateful for the enthusiastic support of the Yukon Geological Survey during this work. The authors would like to thank Derek Cronmiller of the Yukon Geological Survey for a very helpful critical review, which tightened and improved the paper. This research was made possible by an NSERC Alliance Society grant to John Stix and Margaret Kalacska.

References

Bond, J.D., Lipovsky, P.S. and von Gaza, P., 2008. Surficial geology investigations in Wellesley basin and Nisling Range, southwest Yukon. *In*: Yukon Exploration and Geology 2007, D.S. Emond, L.R. Blackburn, R.P. Hill and L.H. Weston (eds.), Yukon Geological Survey, p. 125–138.

Calmels, F., Roy, L.P., Laurent, C., Pelletier, M., Kinnear, L., Benkert, B., Horton, B. and Pumple, J., 2015. Vulnerability of the north Alaska Highway to permafrost thaw: A field guide and data synthesis. Northern Climate ExChange, Yukon Research Centre, Whitehorse, Yukon, 130 p., https://www.yukonu.ca/sites/default/files/inline-files/permafrost_report.pdf

de Grandpré, I., Fortier, D. and Stephani, E., 2012. Degradation of permafrost beneath a road embankment enhanced by heat advected in groundwater. Canadian Journal of Earth Sciences, vol. 49, no. 8, p. 953–962.

Doré, G., Beaulac, I. and Shur, Y., 2005. Performance of the Alaska Highway Beaver Creek area. Faculté des Sciences et de Génie, Université Laval, Final Report GCT-04-17, 108 p.

Douglas, T.A., Hiemstra, C.A., Anderson, J.E., Barbato, R.A., Bjella, K.L., Deeb, E.J., Gelvin, A.B., Nelsen, P.E., Newman, S.D., Saari, S.P. and Wagner, A.M., 2021. Recent degradation of interior Alaska permafrost mapped with ground surveys, geophysics, deep drilling, and repeat airborne LiDAR. The Cryosphere, vol. 15, no. 8, p. 3555–3575.

Engineering Toolbox, 2024. Surface emissivity coefficients, https://www.engineeringtoolbox.com/emissivity-coefficients-d_447.html [accessed 2024/12/08].

Geyman, E.C., Douglas, M.M., Avouac, J.P. and Lamb, M.P., 2024. Permafrost slows Arctic riverbank erosion. Nature, vol. 634, no. 8033, p. 359–365.

Hjort, J., Streletskiy, D., Doré, G., Wu, Q., Bjella, K. and Luoto, M., 2022. Impacts of permafrost degradation on infrastructure. Nature Reviews Earth & Environment, vol. 3, no. 1, p. 24–38.

Huscroft, C.A., Lipovsky, P.S. and Bond, J.D., 2004. A regional characterization of landslides in the Alaska Highway corridor, Yukon. Yukon Geological Survey, Open File 2004-18, 65 p., report and CD-ROM.

Jorgenson, M.T., 2022. Thermokarst. Treatise on Geomorphology (Second Edition), vol. 4, p. 392–414.

Lipovsky, P.S., Humphries, J.K., Stewart-Jones, E.T. and Cronmiller, D.C., 2022. Yukon permafrost database: A new baseline data resource. *In:* Yukon Exploration and Geology 2021, K.E. MacFarlane (ed.), Yukon Geological Survey, p. 37–49.

López, X., Bilodeau, J.-P., Doré, G. and Lemieux, C., 2024. Long-term evaluation of mitigation techniques used for permafrost thermal stabilization at the Beaver Creek (YT) experimental road site. *In:* 12th International Conference on Permafrost, Whitehorse, Yukon, p. 240–247.

Patton, A.I., Rathburn, S.L., Capps, D.M., McGrath, D. and Brown, R.A., 2021. Ongoing landslide deformation in thawing permafrost. Geophysical Research Letters, vol. 48, no. 16, e2021GL092959.

Reimchen, D., Doré, G., Fortier, D. and Walsh, R., 2009. Cost and constructability of permafrost test sections along the Alaska Highway, Yukon. *In:* 2009 Annual Conference and Exhibition of the Transportation Association of Canada-Transportation in a Climate of Change, p. 1–20.

SRK Consulting, 2018. Design report highway stabilization kilometre 1840+500 – 1840+899 (Dry Creek). SRK Consulting (Canada) Inc. Project 1CG023.004, 99 p.

Throop, J., Lewkowicz, A.G. and Smith, S.L., 2012. Climate and ground temperature relations at sites across the continuous and discontinuous permafrost zones, northern Canada. Canadian Journal of Earth Sciences, vol. 49, no. 8, p. 865–876.

Wiebe, A.J., McKenzie, J.M., Hamel, E., Rudolph, D.L., Mulligan, B. and de Grandpré, I., 2024. Groundwater vulnerability in the Yukon and Northwest Territories, Canada. Hydrogeology Journal, vol. 32, no. 2, p. 341–346.

Western Arctic Regional Network of Seismographs (WARNS): History, challenges and improvements in continuous broadband seismic data recordings in northwestern Canada

Andrew J. Schaeffer and Jeremy M. Gosselin*
Natural Resources Canada, Geological Survey of Canada - Pacific, Sidney, BC

Pascal Audet
University of Ottawa, Ottawa, ON

Maurice Colpron
Yukon Geological Survey, Whitehorse, YT

Scott Cairns and Barrett Elliott
Northwest Territories Geological Survey, Yellowknife, NT

Schaeffer, A.J., Gosselin, J.M., Audet, P., Colpron, M., Cairns, S. and Elliott, B., 2025. Western Arctic Regional Network of Seismographs (WARNS): History, challenges and improvements in continuous broadband seismic data recordings in northwestern Canada. *In*: Yukon Exploration and Geology Technical Papers 2024, L.H. Weston, A. Stuart, S.K. Schultz, A.D. Brubacher and D.C. Cronmiller (eds.), Yukon Geological Survey, p. 51–73.

Abstract

The Western Arctic Regional Network of Seismographs (WARNS) is a collection of 20 seismic stations that addresses critical gaps in the seismic network coverage in northwestern Canada. This seismic network has a complex history of adoption and integration of past temporary seismic experiments. We summarize this history along with the challenges in operating in the Canadian North. The WARNS stations provide continuous, weak-motion broadband seismic recordings. The data from these are made accessible (in real time for many stations) via integration within the EarthScope Data Management Centre. This enables open access and facilitates improvements in regional earthquake monitoring and geoscientific discovery. Northwestern Canada is geologically and tectonically complex, which leads to elevated geohazard potential. The environment in the Canadian north is also rapidly evolving in response to climate change, which has the potential to enhance hazards. Studies that rely on data from WARNS play an important role in developing adaptation strategies for the evolving needs and hazards in Canada's north.

Plain language summary

The Western Arctic Regional Network of Seismographs (WARNS) is a system of 20 seismic stations in northwestern Canada that continuously measures ground vibrations created by local and distant earthquakes. This network is designed to address gaps in earthquake monitoring across this remote region. The network builds on earlier temporary experiments. The WARNS stations provide continuous recordings of ground motion, and much of this data is available in real time through the EarthScope Data Management Centre. This open access improves earthquake monitoring and supports numerous branches of scientific research. Northwestern Canada is a geologically complex area with significant earthquake and geological hazards. This is further complicated by climate change rapidly transforming the northern environment, potentially increasing risks. Research using WARNS data is essential for developing strategies to adapt to these evolving hazards and meet the region's future needs.

* andrew.schaeffer@nrcan-rncan.gc.ca

Introduction

Northern regions have been warming at several times the average global rate during the last 50 years (Rantanen et al., 2022). In northwestern Canada, this leads to environmental changes that impact ecosystems, accessibility and economic integration, which can increase the frequency and severity of geohazards (e.g., earthquake shaking and subsequent triggered landslides; Larsen and Huskey, 2015). The impacts of climate change disproportionately affect livelihoods and Indigenous communities of Canada's northern regions (Vogel and Bullock, 2021). Studies on geological processes in the Arctic, including routine earthquake monitoring, play an important role in developing adaptation strategies for the evolving needs and hazards in Canada's north. Geologically, northwestern Canada is a region of complex, active tectonics with abundant earthquake activity. Associated elevated hazards are acknowledged in the national seismic hazard model of Canada (Kolaj et al., 2020). Yet, many details of the ongoing tectonic processes and the associated hazards (and how those hazards may be evolving with environmental forcing) are poorly understood. The information that is input for hazard models in northwestern Canada is sparse compared to Canada's southern regions.

Among several contributing factors, the remoteness of the Canadian territories has resulted in a historically sparse network of seismograph stations that are critical for research and routine earthquake monitoring. Furthermore, it has been demonstrated that large-scale geophysical observations capable of imaging the lithospheric system play a critical role in the identification and quantification of new critical mineral resources (Hoggard et al., 2020; Lawley et al., 2022). Recognition of the complex geology, hazards, natural resource potential and evolving environment has motivated scientific discovery in northwestern Canada in recent years. This has included significant changes to the regional network of seismograph stations, which is the focus of this report. As an initiative of the Geological Survey of Canada (GSC), University of Ottawa (UO), Yukon Geological Survey (YGS) and Northwest Territories Geological Survey (NTGS), WARNS represents a set of seismograph stations that complement the established Canadian National Seismograph Network (CNSN), and significantly enhance geoscientific research and earthquake monitoring. The data from these stations are made openly accessible via integration within the EarthScope Data Management Centre to promote geoscientific discovery.

Regional tectonics and seismicity

Northwestern Canada is a region of complex geology and deformation due to past and ongoing tectonism throughout the region. It can be broadly subdivided into the Beaufort-Mackenzie basin, parts of the Canadian Shield and the North American Cordillera. The Beaufort-Mackenzie basin is a large sedimentary basin located in the Beaufort Sea, off the northern shore of mainland Canada (Fig. 1). The Canadian Shield is a stable, ancient craton that forms the geological core of North America. Precambrian rocks that form the Shield indicate a long history of tectonic stability (Nelson et al., 2013; Hyndman, 2023). The Cordillera is a geologically young and active mountain belt that extends along the western margin of North America, juxtaposed against the stable craton (Nelson et al., 2013). In northwestern Canada, it is often referred to as the Northern Canadian Cordillera (NCC; e.g., Estève et al., 2023). The complex geology of the NCC is characterized by far-travelled fragments of crustal material (terranes) of different origins that have accreted to the North American margin throughout geological time (Monger and Price, 2002; Nelson et al., 2013). Terrane accretion has resulted in a variety of rock-type assemblages throughout the NCC. Active tectonics within the NCC is evidenced by ongoing orogenesis, volcanism and seismicity (Hyndman et al., 2005; Hyndman, 2010; Russell et al., 2023). As a result, the region hosts a broad range of mineral deposits (Nelson et al., 2013).

Active tectonics in northwestern Canada are driven by the oblique collision of the Pacific plate and Yakutat microplate with the North American plate. The ongoing convergence of the thick, buoyant Yakutat microplate has resulted in flat-slab subduction (Eberhart-Phillips et al., 2006; Finzel et al., 2011; Bruhn et al., 2012) and rapid uplift and exhumation of the St. Elias Mountains (Fig. 1; Enkelmann et al., 2008). Regional tectonic plate motions are accommodated by this significant coastal uplift, as well as partitioning between convergence and several major strike-slip faults. These include the Denali, Teslin and Tintina faults, crustal-scale faults that have accumulated hundreds of kilometres of right-lateral offset over geological time (Gabrielse et al., 2006; Waldien et al., 2021).

In the Richardson and Mackenzie mountains (Fig. 1), active plate tectonics is driven by the convergence of the NCC with the stable North American plate. Convergence within these inland mountain ranges is suggested to be driven by far-field stress transfer from the collision of the Yakutat microplate (Mazzotti

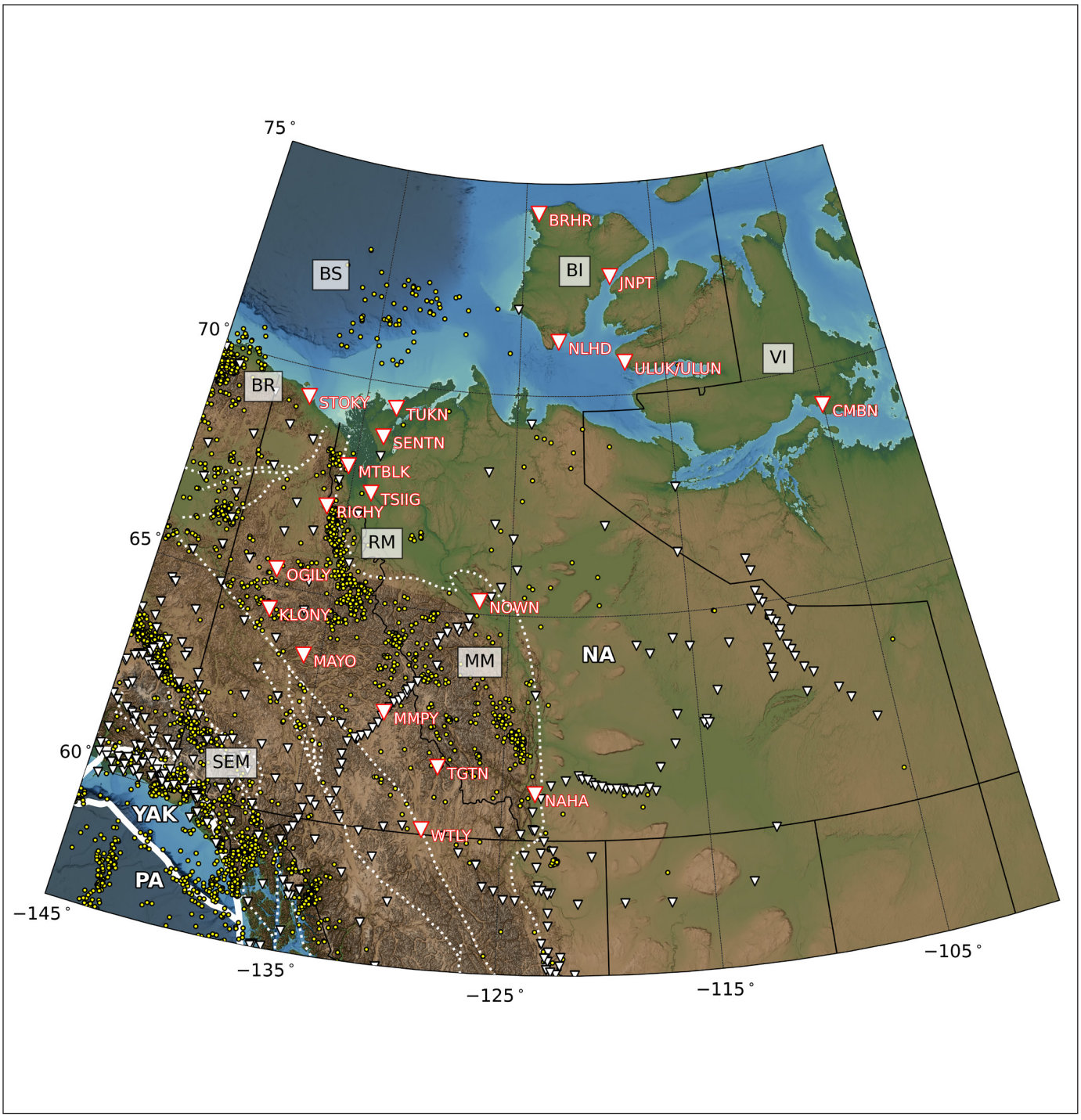

Figure 1. *Seismicity in northwestern Canada. The epicentres of earthquakes of magnitude ≥3 between 2000 and 2024 are shown as yellow circles. Seismicity in northern Canada is clustered near tectonic and topographic features, including the St. Elias Mountains (SEM), Mackenzie Mountains (MM), Richardson Mountains (RM), Brooks Range (BR) and the Beaufort Sea (BS). Seismic stations within the Western Arctic Regional Network of Seismographs (WARNS) are shown as large white triangles (outlined in red). Seismic stations with publicly available broadband seismic recordings (of any duration) are shown as small white triangles. Active tectonics are characterized by the interactions of the Pacific (PA), Yakutat (YAK) and North American (NA) tectonic plates. Tectonic plate boundaries are shown as thick white lines. The geology in this region is characterized by the juxtaposition of the North American Cordillera next to the stable North American Craton. The Cordillera is transected by several crustal-scale faults (dotted lines). Banks Island (BI) and Victoria Island (VI) are discussed in the text. Provincial and territorial boundaries are shown in black.*

and Hyndman, 2002). This implies a rigid upper crust within the NCC that transfers stress over hundreds of kilometres via a thermally modulated detachment in the lower crust, which has implications for crustal structure (e.g., Estève et al., 2021; Schutt et al., 2023). Oblique collision pushes the NCC to the northeast. The northerly motion causes strike-slip deformation in the Richardson Mountains and may contribute to the seismicity in the Beaufort Sea (Hyndman et al., 2005; Hyndman, 2010). An alternative mechanism for deformation in the Mackenzie and Richardson mountains involves stress transferred westward through the stable North American craton via the opening of the North Atlantic Ocean (Enkelmann et al., 2019; McKay et al., 2021).

The NCC is characterized by high temperatures at shallow depths, which impacts natural resource potential (e.g., geothermal) and natural hazards. Evidence of high temperatures includes high geothermal heat flow measurements (e.g., Grasby et al., 2011), shallow Curie depths (e.g., Gaudreau et al., 2019), an inferred shallow lithosphere-asthenosphere boundary (LAB; e.g., Audet et al., 2019) and low seismic velocities in the mantle (e.g., Schaeffer and Lebedev, 2014; Tesauro et al., 2014). Distributions of seismicity throughout the NCC concentrated at shallow depths (often approximately 10 km or less) suggest that high temperatures in the lower crust may inhibit brittle deformation (e.g., Choi et al., 2021; Estève et al., 2022; Drooff and Freymueller, 2023; Biegel et al., 2024). In contrast to the NCC, the adjacent North American craton is cold, tectonically stable, and exhibits low levels of seismicity. Additionally, the NCC is among the most volcanically active regions of Canada (Cassidy and Mulder, 2023; Russell et al., 2023), and although no volcanoes in Canada have erupted since seismic monitoring began more than a century ago, volcanic seismicity likely also occurs throughout the NCC. Furthermore, seismic monitoring limitations may preclude the ability to detect micro-earthquake activity associated with many volcanoes in Canada (Cassidy and Mulder, 2023).

Seismicity in northwestern Canada is spatially clustered near the aforementioned tectonic features associated with major tectonic domains and their bounding faults and structures. Notably, the majority of earthquakes occur in southwestern Yukon due to the active convergence of the Yakutat microplate with the western edge of North American (Fig. 1). The geometry (obliquity) of the active tectonic boundary with respect to relative plate motion leads to predominantly reverse and dextral strike-slip earthquakes (and likely slip partitioning) in this region (Doser, 2014; Gosselin et al., 2023, 2024). The largest earthquakes in northwestern Canada also occur here. This includes events along the active plate margin (Plafker et al., 2008), as well as inboard along major faults such as the Denali fault (Eberhart-Phillips et al., 2003). Much of the interior of the NCC exhibits low levels of seismicity (Fig. 1), and limited seismicity along other major faults (e.g., Teslin and Tintina). Seismicity is also clustered along the Cordilleran deformation front (eastern edge of the NCC), including the Mackenzie and Richardson mountains (Fig. 1). Earthquakes in the Mackenzie Mountains exhibit predominantly reverse mechanisms due to active convergence of the NCC with the North American craton. This transitions to predominantly dextral strike-slip earthquakes in the Richardson Mountains due to the component of northerly motion of the NCC relative to the North American plate (Hyndman et al., 2005; Ristau et al., 2007; Leonard et al., 2008). Despite their position hundreds of kilometres from the active plate boundary, recorded seismicity includes several large magnitude (M) earthquakes (M >6) in both the Richardson (e.g., Cassidy and Bent, 1993) and Mackenzie (e.g., Wetmiller et al., 1988; Horner et al., 1990; Cassidy et al., 2005) mountains.

Moderate seismicity is also clustered in the Beaufort Sea (Fig. 1). The western part of the basin is characterized by a fold and thrust belt associated with the Cordilleran orogen, whereas the eastern part of the basin is characterized by extensional structures (Hyndman et al., 2005). As these events occur offshore but are only observed at seismograph stations on land, the constraints on seismicity in the Beaufort-Mackenzie basin are poor; improving these details will require offshore ocean-bottom seismometer deployments. Limited earthquake mechanism solutions exhibit normal and strike-slip faulting, and consistently subhorizontal tension axes (Hyndman et al., 2005). Earthquakes beneath the Beaufort Sea are interpreted to occur in the lower crust or uppermost mantle (Audet and Ma, 2018). It has been suggested that this seismicity may be related to flexural bending and tension in the upper lithosphere due to loading from the rapidly developing Mackenzie Delta (and associated sedimentary trough; Lane, 2002; Hyndman et al., 2005). Furthermore, the Beaufort Sea continental margin is considered a Cenozoic convergent boundary and may represent incipient subduction (Estève et al., 2022). Furthermore, large (M >6) earthquakes have been recorded in the region, demonstrating the potential for future large (though infrequent) earthquakes (Hasegawa et al., 1979).

Evolution of seismic infrastructure in northwestern Canada

The historically limited density of geophysical infrastructure across the Canadian Arctic was due to various factors, including accessibility, the vastness of the terrain (i.e., sparse resources), and weather that may exhibit severe seasonal fluctuations. Much of the region is inaccessible during winter months, and there are few passable roads. Combined, these factors made routine scientific operations, including instrument maintenance, more challenging. The challenges in field operations and maintenance necessitate larger budgets to work in remote, northern regions. Such research budgets were often difficult to justify, in part due to the low population density of the Canadian territories, and therefore lower inferred risk. With the present increase in proposed northern development and infrastructure projects, the recognition of the growing risks posed to northern inhabitants, in addition to the potential opening of the Northwest Passage through the Canadian Arctic Archipelago, it becomes even more critical to maintain a strong geophysical monitoring network to inform policy, impact assessments, and infrastructure design and resilience to a range of natural and induced hazards.

Despite these challenges, geophysical instrumentation has made its way into the Canadian north episodically during the last few decades. Though the expansion and improvement of the permanent CNSN has been slow, temporary experiments have resulted in a significant advancement in geophysical instrumentation, followed by a regression of the cumulative network when these temporary stations have been removed (Fig. 2). However, some stations from these deployments have been retained and converted into permanent sites. The history of the cumulative seismic network reflects this growth and cyclical nature (Fig. 2).

Despite knowledge of the occurrence of large earthquakes in northwestern Canada (which can be detected on distant global seismic stations), the first seismograph station in the Yukon was not installed until 1971, in Whitehorse (Fig. 3). This was many decades after the establishment of the seismograph network in southern Canada and adjacent Alaska, and was motivated by the desire to improve the understanding of seismicity in the Yukon and the Mackenzie Valley due to ongoing discussions of a potential pipeline project in the region. Driven by the M 7.9 Denali earthquake in central Alaska in 2002 (Eberhart-Phillips et al., 2003), the CNSN was augmented with approximately 10 new seismograph stations in 2010. These were installed in the vicinity of the eastern segment of the Denali fault (in southwestern Yukon), significantly enhancing routine earthquake monitoring capabilities (Meighan et al., 2013) and improving capacity for research in regional seismology and tectonics. Several large-scale temporary deployments occurred around this time (a few years before and after; Fig. 2).

Numerous stations across Canada were associated with the multi-institution Portable Observatories for Lithospheric Analysis and Research Investigating Seismicity (POLARIS; Eaton et al., 2005) experiment. This large-scale investigation comprised more than 100 telemetered (i.e., real-time data transfer) broadband seismic stations, and 10 continuously recording magnetotelluric instruments. In the context of northwestern Canada, these stations (network code PO) were initially deployed over the Slave Craton in the Northwest Territories during the early 2000s (Fig. 4). Later, some stations were relocated westward toward the Mackenzie Mountains and the westernmost extent of the Canadian Shield.

Concomitant to the POLARIS experiment in northwestern Canada was the United States-led Canadian Northwest Experiment (CANOE; Gaherty and Revenaugh, 2003), which was deployed from 2003 to 2005 as a three-prong array centred on Fort Nelson, British Columbia. The instrumentation included 50 broadband seismographs from the Portable Array Seismic Studies of the Continental Lithosphere (PASSCAL) instrument pool (Aster et al., 2005), as well as an additional 10 seismographs from the University of British Columbia. The western transect extended from Fort Nelson to Whitehorse along the Alaska Highway, and the northern arm along the highway from Fort Nelson to Yellowknife (Fig. 4). The southern arm connected Fort Nelson to Edmonton, where it met with the northern termination of a similar experiment spanning from Florida to Edmonton.

The migration of the EarthScope Transportable Array (TA) from the continental United States to Alaska (Busby and Aderhold, 2020) represented another significant (though temporary) improvement in seismological instrumentation in northwestern Canada (Fig. 2). During the eight-year duration of the TA in Alaska, 38 stations were installed within Canada: 4 in Northwest Territories, 28 in the Yukon and 6 in British Columbia (Fig. 4). The earliest TA stations installed in the Canadian north during 2012 and 2013 were located in Sachs Harbour and Paulatuk, Northwest Territories, and Eagle Plains in the Yukon. The remaining TA stations in northwestern Canada were mostly installed between 2015 and 2017.

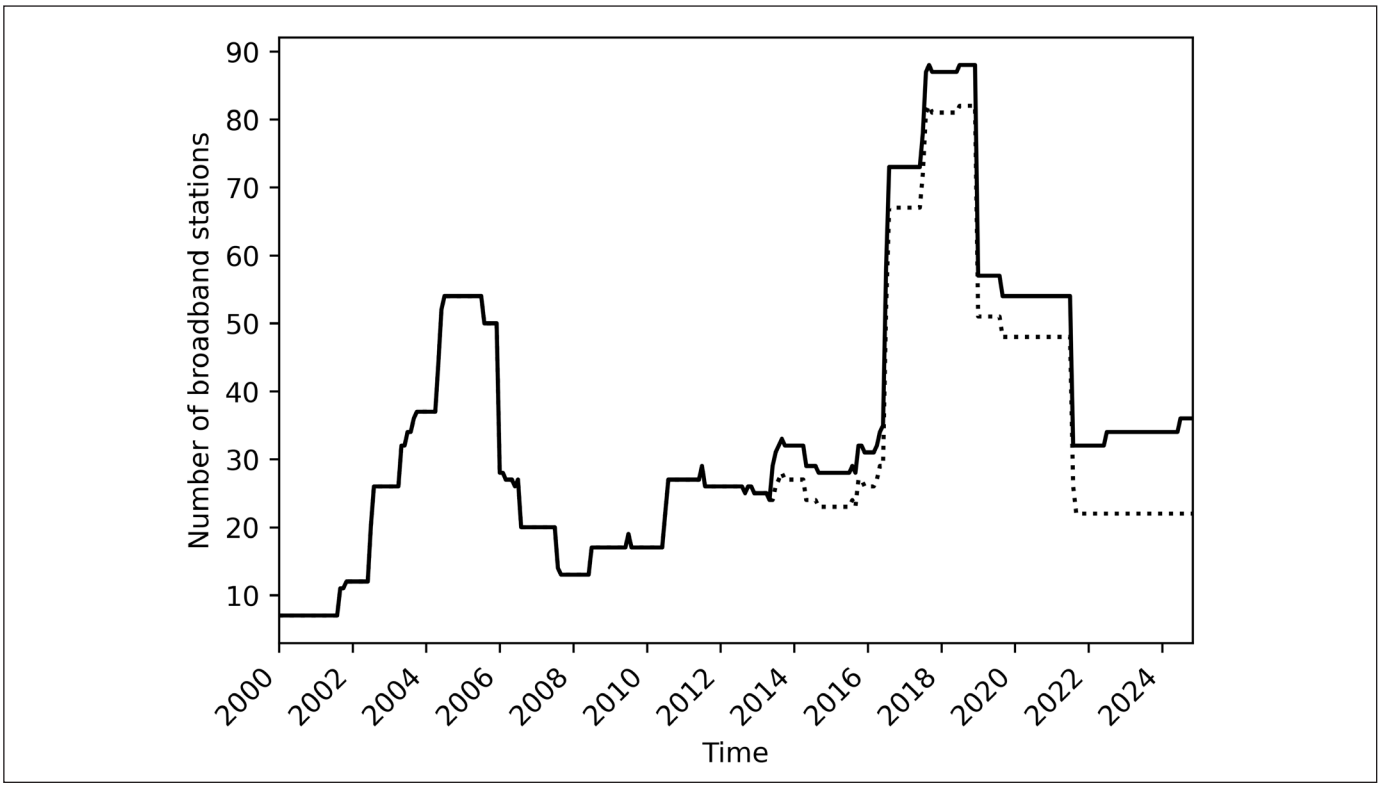

Figure 2. *Evolution of digital broadband seismic recordings in the Canadian territories, and the monthly number of broadband seismic stations with publicly available digital recordings in the Yukon, Northwest Territories and Nunavut (specifically within the range of 100°–141° longitude and 60°–80° latitude). Note the significant increase in available seismic recordings between 2002 and 2008 due to the Portable Observatories for Lithospheric Analysis and Research (POLARIS; Eaton et al., 2005) and Canadian Northwest Seismic Experiment (CANOE; Gaherty and Revenaugh, 2003) experiments. Similarly, a significant increase in available seismic recordings is observed between 2016 and 2022 due to the EarthScope Transportable Array experiment extension into western Yukon (Busby and Aderhold, 2020), as well as the Mackenzie Mountain transect experiment (Baker et al., 2020). The dashed line illustrates the number of available stations without the Western Arctic Regional Network of Seismographs (WARNS) stations. Without WARNS, the current broadband seismic network in northwestern Canada would revert to pre-2010 numbers.*

Decommissioning was planned for 2020; however, due to the global COVID-19 pandemic, the TA sites in Canada continued to operate for an additional year.

The flexible array Mackenzie Mountains EarthScope Project (MMEP; Baker et al., 2020) was a network of 40 broadband seismograph stations that also temporarily improved seismological instrumentation in northwest Canada (Fig. 2). The MMEP stations were deployed in a roughly linear array transecting much of the Northern Canadian Cordillera and extending into the Canadian Shield (Fig. 4), between 2016 and 2018, coinciding with the EarthScope TA experiment in Alaska.

The Yukon Northwest Seismograph Network (YNSN, network code NY) consisted of an array of seven seismic stations straddling the Mackenzie Mountains of central Yukon and the westernmost Northwest Territories. Originally deployed in 2013, the YNSN was a Canadian Foundation for Innovation (CFI) and Natural Sciences and Engineering Research Council of Canada (NSERC)-funded initiative of the University of Ottawa motivated by the EarthScope TA experiment. Data from all seven stations were telemetered in real time to the GSC Pacific Data Centre (GSC-PDC) via satellite-based communications. Currently, three of the YNSN stations have been decommissioned with the termination of the experiment (FLDN, WGLY and FARO), whereas four remain operational (MAYO, MMPY, TGTN and WTLY) due to adoption by the GSC and inclusion in WARNS (Figs. 4 and 5).

In 2015, the Banks Island Seismograph Network (BISN) was established as a joint endeavour between the formerly known Northwest Territories Geosciences Office (NTGO) and the University of Ottawa. The

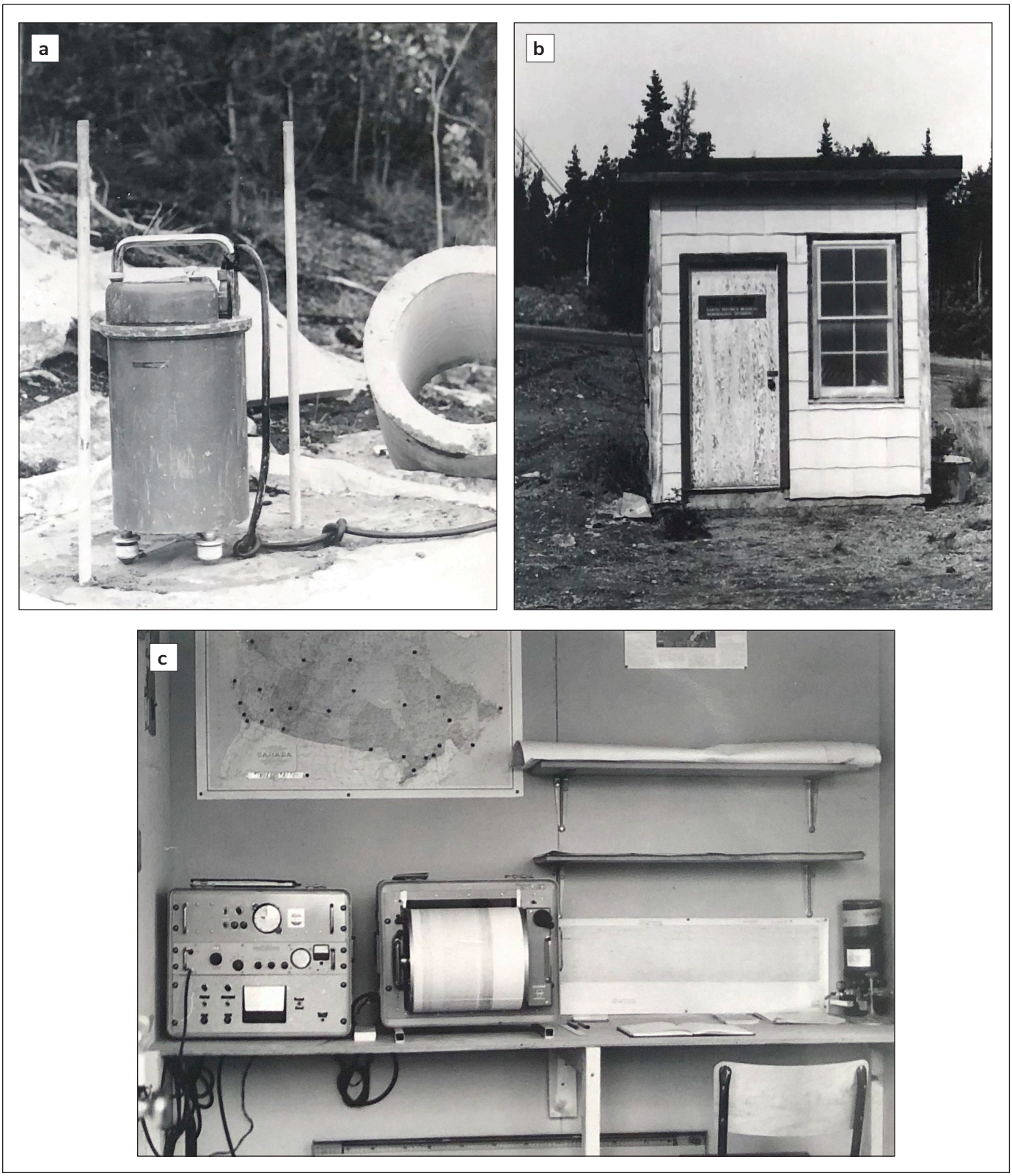

Figure 3. *The first seismograph station in the Yukon was originally installed in 1971 in Whitehorse.* ***(a)*** *The station consisted of a Willmore seismometer (sensor) installed on a cement pad.* ***(b)*** *The recording equipment for the station was housed in a nearby structure.* ***(c)*** *The sensor was connected to a Teledyne EA310 amplifier and helicorder inside the structure (Garry Rogers, pers. comm., November 2024).*

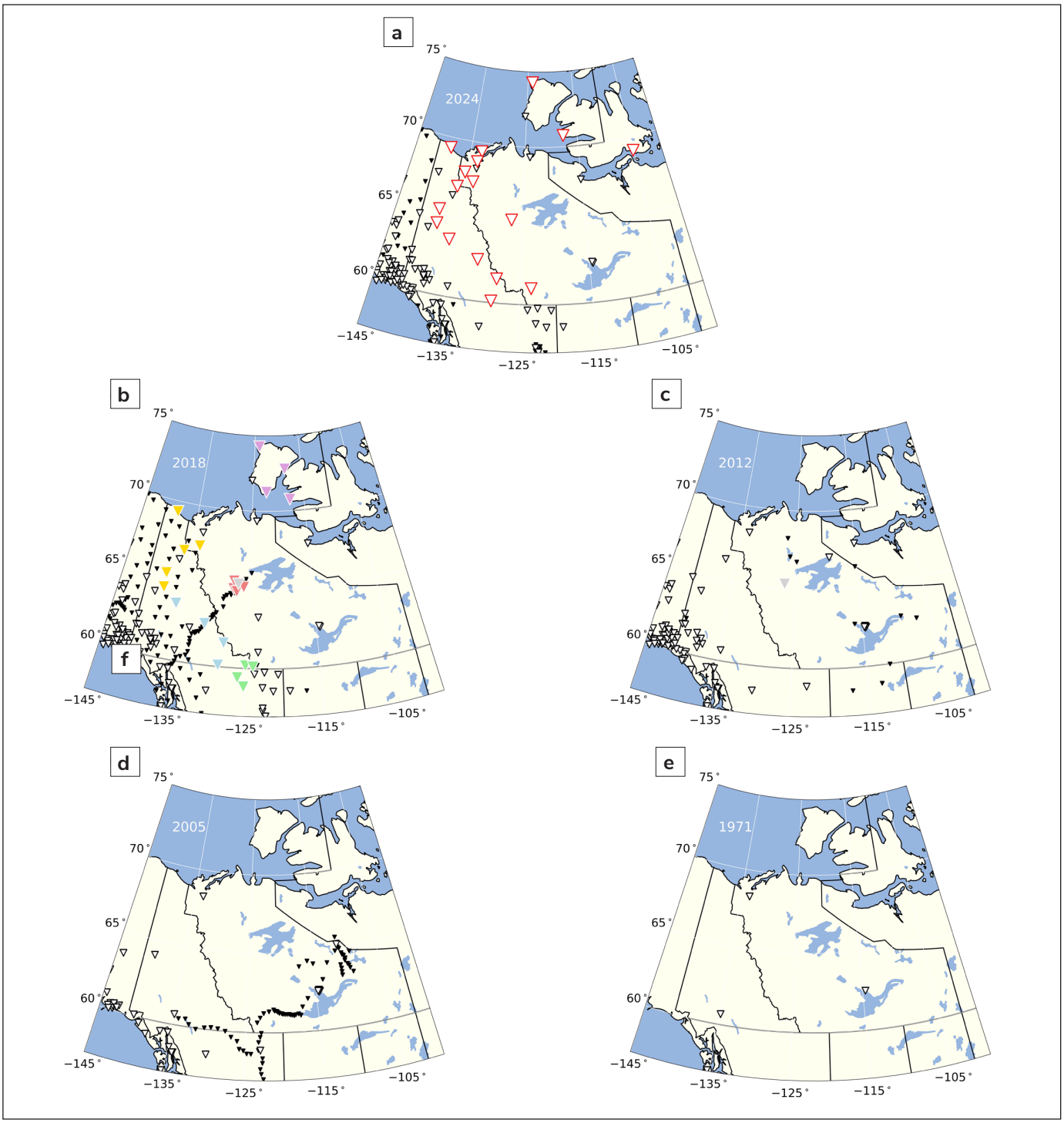

Figure 4. *Seismic network evolution in northwestern Canada. Stations that are part of the Western Arctic Regional Network of Seismographs (WARNS) are depicted by the red-outlined triangles. The locations of broadband seismic stations that were actively recording during the specific years of 2024, 2018, 2012, 2005 and 1971 are depicted in* ***(a)****–****(e)****. Stations affiliated to WARNS (details discussed in the text) are highlighted in (b) and (c) and are coloured according to experiment (same as Figure 5). Other permanent and temporary broadband seismic stations are represented by large (white) and small (black) triangles, respectively. The first seismic station in the Yukon was installed in Whitehorse in 1971. The POLARIS (Eaton et al., 2005) and CANOE (Gaherty and Revenaugh, 2003) experiments are illustrated in (d). The EarthScope TA (Busby and Aderhold, 2020) and MMEP (Baker et al., 2020) experiments are illustrated in (b). Provincial and territorial boundaries are denoted with solid black lines.*

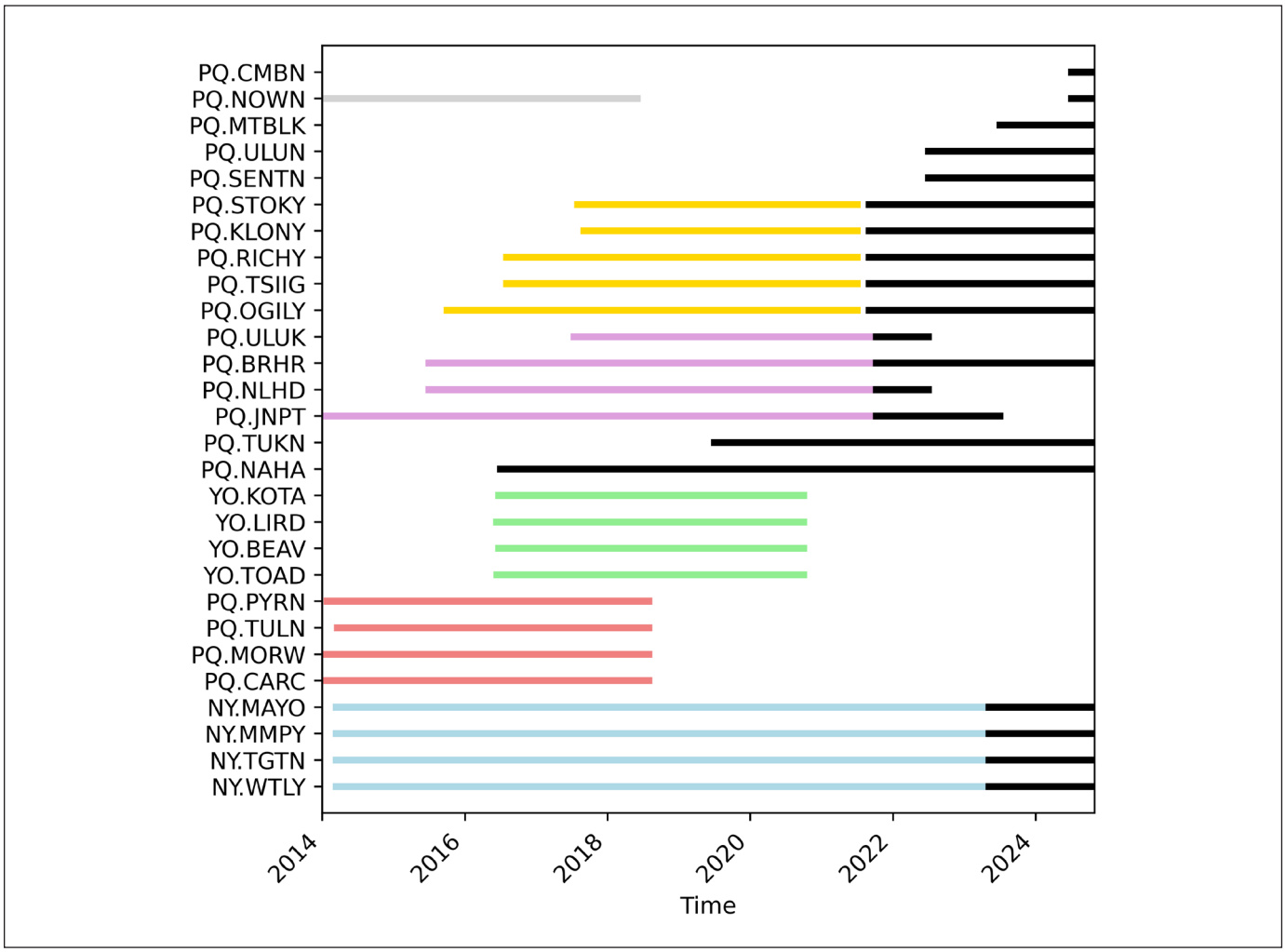

Figure 5. *Deployment history of stations in the Western Arctic Regional Network of Seismographs (WARNS). The history of WARNS station deployment is depicted in black. Select station deployment history for other networks and experiments are also illustrated, including the EarthScope Transportable Array (TA; yellow), the University of Ottawa Yukon Northwest Seismograph Network (YNSN; blue), the Normal Wells Seismic Monitoring array (NWSM; pink), the Yukon Observatory array (YO; green), the Banks Island Seismograph Network array (BISN; purple), and the Portable Observatories for Lithospheric Analysis and Research Investigating Seismicity (POLARIS; grey). Some sites and equipment were subsequently adopted by WARNS upon completion of the respective temporary experiments. Details are discussed in the text.*

objective of this experiment was to examine the nature of the lithosphere beneath Banks Island and the nearby continental shelf slope in the Beaufort Sea (Fig. 1). Two temporary stations had previously existed in the southwest Canadian Arctic Archipelago on Banks and Victoria islands (Fig. 1). The site at Johnson's Point on Banks Island (JNPT) was situated along the Prince of Wales Strait and hosted an exploration camp. It consisted of a significant beach landing strip that was once capable of handling a C-130 Hercules Aircraft. The equipment for JNPT had previously been located near the Hamlet of Ulukhaktok (ULU) on Victoria Island, at the western point of the Diamond Jenness Peninsula. The decision to relocate the equipment across the strait was made as station ULU had been damaged by wildlife several years in a row. Station JNPT was ultimately retained in BISN, which was eventually acquired by WARNS (Fig. 5). Both BISN and WARNS were assembled and operating, and a minimal budget was spent on the purchase of new seismic equipment (i.e., most sites were assembled and operating using preexisting available equipment).

Farther to the south near the Town of Norman Wells, NT, the NTGO and GSC deployed the Norman Wells Seismic Monitoring (NWSM) array. This consisted of

a cluster of four stations (MORW, CARC, PYRD and TULN) around a central station (NOWN) in Norman Wells, where oil and gas development has been ongoing for many decades. In response to the possible expansion of facilities, directional drilling and potential hydraulic fracturing, NWSM was deployed to generate a baseline of local seismicity and facilitate ongoing monitoring. This experiment operated from 2014 to 2018. The central station NOWN operated from 2012 to 2018 (Figs. 4 and 5) and was revived in 2024 for WARNS due to its critical position for earthquake monitoring in the Mackenzie Mountains.

The Yukon Observatory (network code YO), developed and operated by the YGS, was an array of four seismic stations that were operational from 2016 to 2020 (Fig. 5). Similar to the NWSM array, the YO was deployed in response to industrial interest in the Liard basin for oil and gas (Fig. 4). The observatory was to establish baseline seismicity then monitor ongoing activity. However, legislation placed a restriction on oil and gas extraction in the Liard basin unless approved by the local First Nations. As a result, the YO was decommissioned in 2020. The equipment from the observatory was redeployed at new sites within WARNS.

The creation of WARNS is largely based on the coincident termination of YNSN, BISN and the EarthScope TA in Canada in 2021. Efforts by the GSC (including funding) and YGS (equipment and in-kind) contributed to the adoption and continued operation of many seismic stations in northwestern Canada. This GSC-YGS collaboration adopted five of the EarthScope TA stations in the Yukon and the Northwest Territories and continues to operate them to this day (Fig. 5). These include sites D28M, F31M, G30M, I29M and J29N, which have been renamed under WARNS (STOKY, TSIIG, RICHY, OGILY and KLONY, respectively). The CNSN also adopted five stations from the EarthScope TA experiment: A36M, C36M, F28M, EPYK and P32M. With the assistance of the YGS and Northwest Territories Geological Survey (NTGS) in facilitating data transfer, these stations are now renamed under CNSN (SACHN, PAULN, CROWY, EAGLY and ATLI, respectively). WARNS and its predecessors have expanded and improved the seismic array through the conversion of offline sites into sites with real-time data transfer. In 2019, a new BISN station was deployed in the Hamlet of Tuktoyaktuk, on the coast of the Arctic Ocean at the end of the Inuvik-Tuktoyaktuk Highway. Through colocation with the Canadian Hydrographic Service (CHS) tide gauge station, and a Canadian Geodetic Service (CGS) geodetic monument, the new TUKN station streams real-time data to the GSC-PDC. Furthermore, the station ULUK, in the Hamlet of Ulukhaktok on Victoria Island (Fig. 1) was colocated with CHS and CGS infrastructure in 2022, enabling real-time data streaming. Additionally, WARNS has also expanded independently through new station deployments, for example, MTBLK and SENTN (Fig. 5).

WARNS

Motivation for continued operation

Seismological infrastructure in northwestern Canada reached a peak in density and uniformity of coverage in 2018–2019 (Fig. 2). Since then, the number of stations has decreased by a factor of apprximately 2–3. Most of the attrition was due to the termination of United States-led experiments (28 of 38 EarthScope TA stations and all 40 MMEP stations were removed). These experiments provided unprecedented potential to unravel new insights into the structure and evolution of the NCC and surrounding regions. However, 10 of these stations were adopted by the GSC and CNSN with territorial partners. As illustrated in Figure 2, it is evident that without the operation of WARNS, the decline in instrumentation post-EarthScope would have decreased station numbers by a factor of approximately four. Ignoring the several large (but temporary) experiments, Figure 2 also illustrates the slow expansion of the cumulative seismograph network in northwestern Canada over time.

The temporary influx of stations, and the data they provide, has led to improved resolving power to address important geoscientific questions. This work has also led to new questions regarding the structure and tectonic evolution of northwestern Canada, as well as associated implications for natural resources and hazards. In particular, enigmatic bands of seismicity are observed beyond the extent of the MMEP array and within the Richardson Mountains in the Yukon and the Northwest Territories. These may be related to deep offshore seismicity in the Beaufort Sea region. The WARNS network is poised to continue contributing to unravelling fundamental, outstanding tectonic questions and improving routine earthquake monitoring in a region of rapidly changing environmental conditions.

The northern territories of Canada are susceptible to more extreme impacts of climate change, which can significantly disrupt day-to-day life for northerners and potentially erase whole communities. For example,

much of the northern territories of Canada are underlain by permafrost that is expected to degrade and thaw in the coming years (Smith and Burgess, 2004). Changes in local site conditions due to the changing environment have the potential to enhance geohazards (including earthquake shaking and associated hazards). The ongoing operation and expansion of WARNS complements the CNSN and other temporary, national and international seismic stations. Together, these afford the capacity to discover the complex and interacting geohazards across the Canadian Arctic. In addition, with increasing accessibility to the Canadian Arctic due to melting sea ice, new development and transit opportunities are being sought, which may lead to an increased susceptibility to geohazards. Continuing the geophysical observations provided by WARNS is important for developing adaptation strategies for northerners and informing future industrial and socio-economic developments.

Challenges

Canada is a vast country, particularly in the northern territories. Beyond 200 km of the Canada-United States border, the distances between population centres are significant. The harsh northern climate further exacerbates the challenges of conducting geoscientific research in remote settings. However, the most significant barrier to conducting research or any type of fieldwork in the north is cost. All individual challenges ultimately result in increased costs compared to performing the same operation at southern latitudes. While year-round highways service many communities in the north, numerous communities remain accessible only by air or via winter roads. Furthermore, many of the areas that need to be accessed to install or maintain seismic stations that fill spatial gaps do not have roads or any nearby communities. In these cases, sites are only accessible by chartered aircraft (fixed wing or helicopter), snowmobile (during winter months) or boat. In addition, while a local community may provide a relatively accessible base for staging field operations, all equipment must still be shipped thousands of kilometres to these northern destinations. Transportation logistics are also generally more challenging due to insufficient transportation options. Adapting to challenging weather, wildfires, landslides and other phenomena may not always be possible. Northern residents are very familiar with these challenges and have lived through many of these phenomena. This presents a stark contrast for those accustomed to the often seamless, logistical benefits of working in southern Canada.

Beyond challenges in terms of cost and logistics, there are many unique challenges encountered specific to operating seismological infrastructure in the Canadian North. The main components of a seismograph station include the power supply, the sensor and digitizer, and communications (for real-time stations). A high-quality installation is typically located away from most sources of local activity capable of generating ground vibrations (e.g., pumps, generators, roads). Access to alternating current (AC) grid power allows for the simplest installations. In more remote settings, direct current (DC) power can be provided by solar panels (or small wind turbines) with supplemental battery banks (for when environmental conditions do not allow for electricity generation). Cellular services or line-based telecommunications are possible near communities to enable real-time seismic data transfer. In more remote settings, satellite telemetry is often required. The trade-offs between site quality, benefits and logistics are more apparent in Canada's north. Locating a station within a community simplifies logistics, power and communication. However, this comes at the cost of signal quality (i.e., higher background noise) and potentially poor site location within a regional context (i.e., not addressing spatial gaps in network coverage). Achieving better signal quality (or site selection) often increases logistical demands, and site accessibility, power and communication requirements.

The use of DC power is further complicated in polar regions. In the summer months, the solar input is significant and can be maximized to charge and maintain battery banks with carefully constructed and oriented solar arrays. However, during the winter months, there is little to no solar input and maintaining a battery bank is challenging. The cold temperatures compound the challenges for power systems. Even though the scientific instruments are typically rated to operate at these temperature extremes, the battery banks are highly temperature sensitive. The available amperage of a standard chemistry lead-acid or gel-cell style battery decreases significantly with decreasing temperature, requiring a larger battery bank to store power during winter months. The power systems used by the WARNS stations adopt a best-practice approach based on similar past experiments. An in-depth analysis of the range and complexity of cold-weather, off-grid power systems is beyond the scope of this report.

The WARNS stations are operated by a small group using a modest budget. Consequently, damage to instrumentation poses a significant operational challenge. As illustrated in Figure 6 (a–c, e), damage can

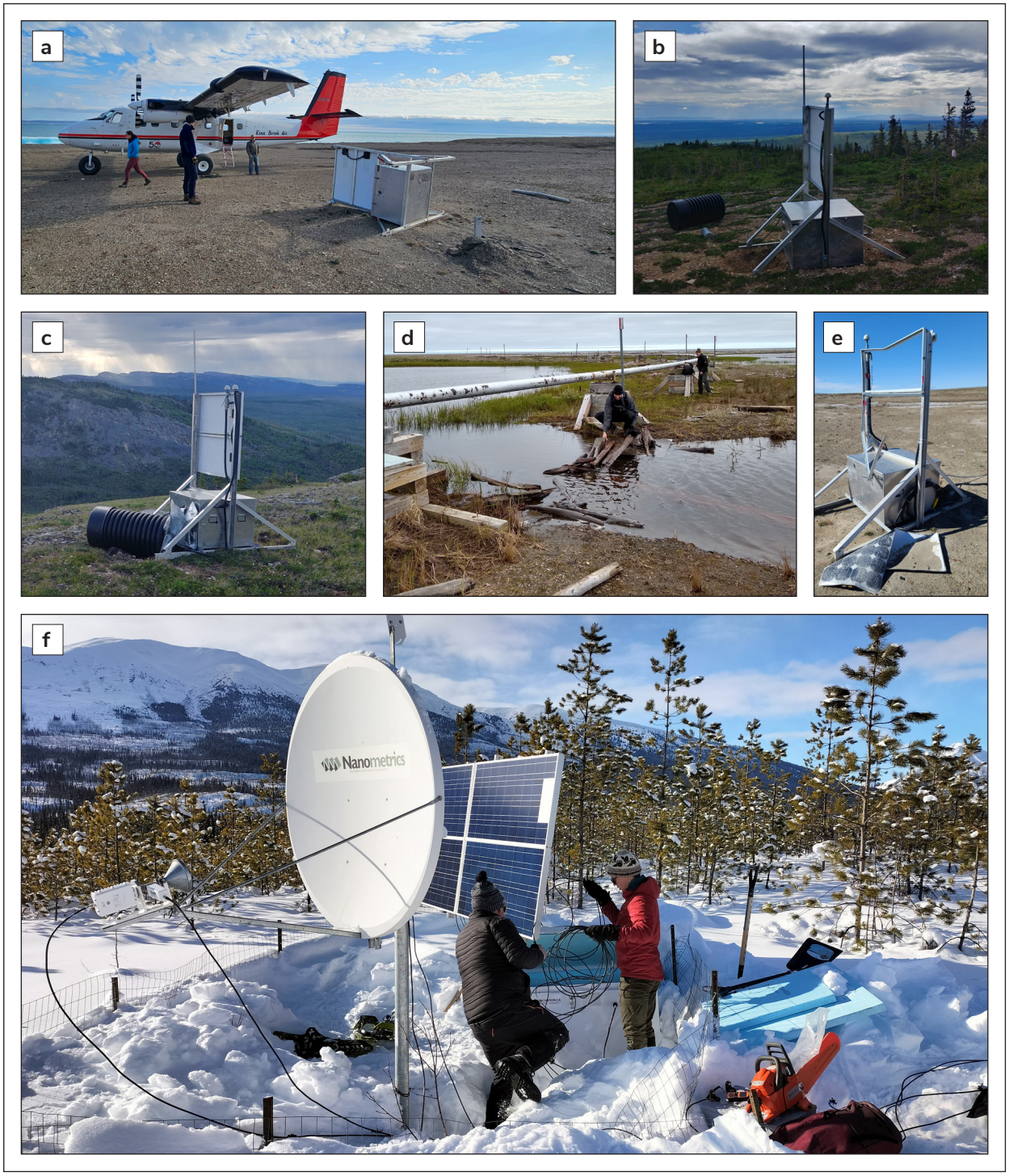

Figure 6. *Common challenges encountered operating geophysical instrumentation in the Canadian north.* ***(a)*** *Site access requires a chartered aircraft capable of off-strip landing. Also pictured is common damage to instrumentation, where polar bears have knocked over the 400 lb. battery and electronics kiosk with mounted solar panels.* ***(b, c)*** *Examples of helicopter-access-only locations where wildlife, likely grizzly bears, have exhumed the seismometer vault (and sensor).* ***(d)*** *Unexpected hazards or washouts are not uncommon when visiting remote sites.* ***(e)*** *The winds in some regions can reach hurricane-force speeds, and cause equipment to fail. Pictured here are two solar panels where high winds blew the panel interiors out of their frames.* ***(f)*** *Snow accumulation can present challenges in mountainous regions of the Northwest Territories and the Yukon. In this example, near Nahanni National Park during March, snow removal was required for site access and to expose the solar panels.*

be caused by various sources that are often unanticipated and/or challenging to prepare for. Due to accessibility and budgetary constraints, sites are generally visited yearly. Efficient and effective station servicing is critical as charter availability (including seasonal or weather limitations) may preclude the ability to visit a site for multiple years. There are several offline stations within WARNS (i.e., non-cellular and non-telemetered). For these stations, data must be harvested during site visits. Since the station's condition is unknown before arrival, a complete set of replacement equipment is typically transported to the site in case significant repairs are required. This includes replacement instrumentation (sensor and digitizer), solar panels, wiring and new batteries.

In the history of WARNS (and its predecessors), significant station damage is typically caused by wildlife. This predominantly involves damage by polar bears (e.g., Fig. 6a) and grizzly bears (e.g., Fig. 6b, c). In these cases, the entire power system and/or electronics enclosure may be overturned. The vault that houses the sensitive and costly seismometer may also be exhumed. While bears generally cause the most catastrophic damage to seismic stations, many smaller animals are also capable of disrupting station operations and causing costly damage. This can include rodents and other small mammals that chew through exposed cables (including costly seismometer cables) and strapping. As a result, where possible, cabling is typically installed in armoured conduit; however, given enough time, harsh conditions can also degrade or damage these materials. Fencing and other enclosures around a seismic station can be effective in some regions. However, anecdotally, enclosures have not made a noticeable difference to station preservation in tundra conditions typical of the Arctic. Here, the flat landscape and lack of vegetation means station infrastructure is visible from great distances and may be an attractant to curious wildlife.

In terms of weather, additional challenges beyond temperature and visibility include high winds in exposed regions. The seismic station equipment installed across this harsh landscape is routinely exposed to hurricane-force winds very close to the ground surface. This has resulted in solar panels getting cracked by high wind pressure and/or being blown out of their frames (e.g., Fig. 6e). In some cases, high winds have resulted in satellite communication dishes that have been rotated on their mounts or have had their solid steel mounting plates sheared off and the dish blown a great distance away.

There is also a perpetual element of new and unknown challenges that arise while operating seismic stations in remote regions of northern Canada. In one instance, high water and wind-driven waves washed out the access trail between the beach-side landing strip and the seismic station located some distance away on the tundra (Fig. 6d). Adaptability and improvisation are often necessary for success. In this case, a bridge over the washed-out trail (now under a metre of water) was constructed using driftwood scavenged from the nearby beach. This unforeseen damage and necessary repair resulted in using up more of the precious time available from the chartered flight schedule. This solution kept critical equipment and people dry. In all subsequent visits to this particular location, a ladder was brought to serve as a temporary bridge over this slowly widening water feature. In addition to adapting to unforeseen challenges, weather will dictate seismic station maintenance and operations in the Arctic. It is not uncommon to have a weather system disrupt small aircraft flights for many days, as pilots must adhere to the visual flight rules, which requires the weather to be clear enough for safe operation. Field teams are often waiting to access a site or more problematically, the team may be stuck at a remote site waiting to be able to leave.

In recent years, the western Canadian Arctic has experienced many wildfires that have had significant negative impacts on communities and their residents. These events have also caused downstream impacts on all activities within the region, including the operation of WARNS and other geoscience research. This has included evacuation orders for communities, air quality below national standards for safety, and rescheduling other aircraft that are not being used in firefighting activities or medical evacuations. Wildfires also cause highway closures that prevent the flow of goods and people, and limit the ability for large-scale road-based evacuation. Wildfires present an evolving hazard of seismic station operations in northwestern Canada and, indeed, the rest of Canada.

WARNS broadband seismic stations and their data in northwest Canada

The stations making up WARNS are diverse in their origin and, therefore, in their design and layout (Fig. 7). However, all sites share the same basic components. A seismometer is central to each station, and is the sensor that is placed in or on the ground that measures the Earth's vibrations. All seismometers at WARNS' sites are weak-motion broadband instruments. The seismometers are connected to a digitizer, a device that

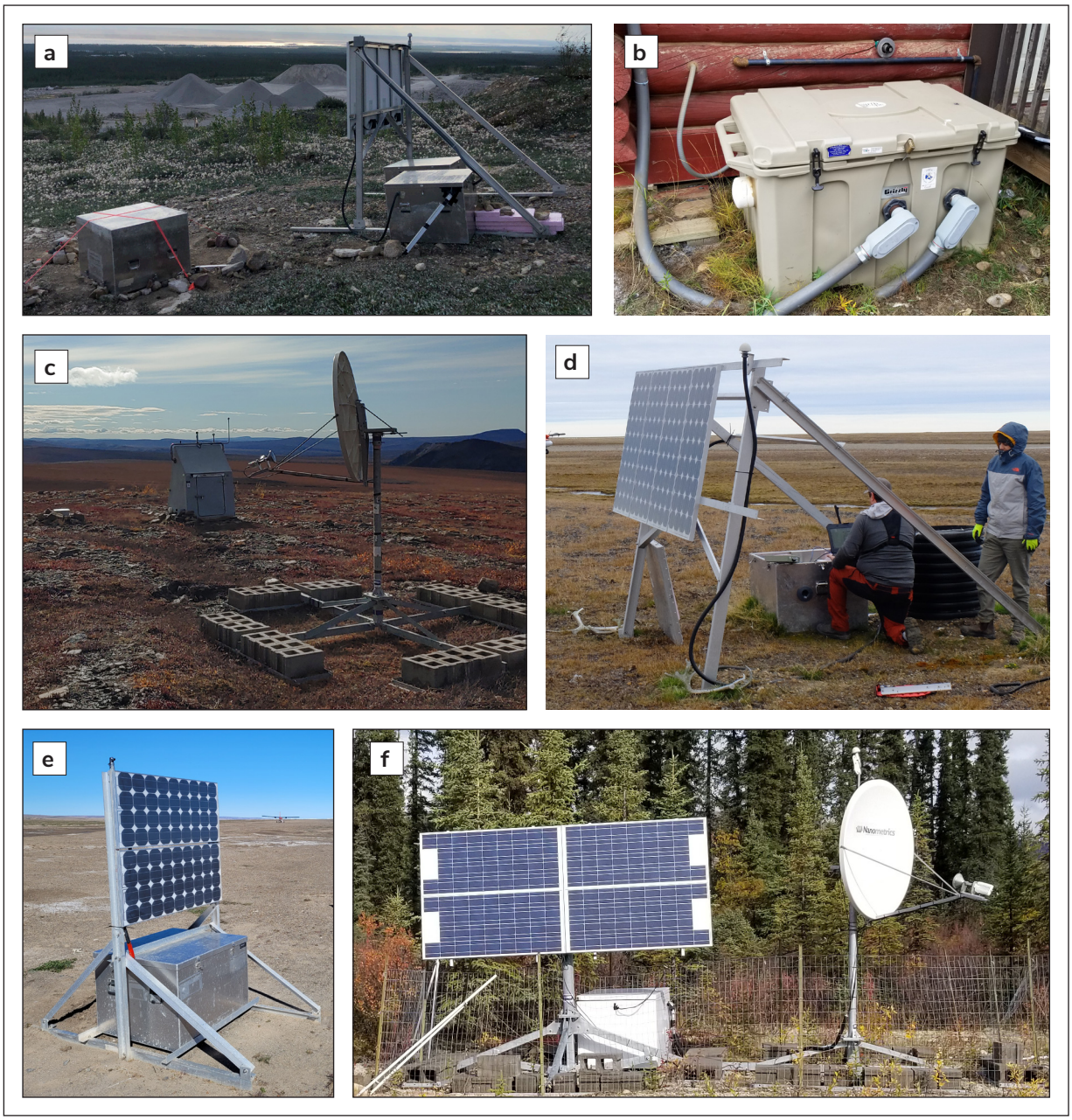

Figure 7. *Examples of WARNS seismic stations.* ***(a)*** *The NOWN station is located in a quarry east of the Town of Norman Wells. It is a solar-powered site equipped with cellular communications for real-time data streaming.* ***(b)*** *The TSIIG station is located within the Hamlet of Tsiigehtchic and is an adopted EarthScope TA station on the grounds of the local visitor's centre. It is AC mains-powered and has a dedicated DSL line for real-time data communications.* ***(c)*** *The RICHY station is located along the Dempster Highway at Wright's Pass (near the border of the Yukon and the Northwest Territories). This station was adopted from the EarthScope TA and still uses the solar power and communications enclosure from the previous experiment. Upon its adoption to WARNS, satellite telemetry was added to the station. Challenges with high winds have resulted in this location being converted to an offline site, and data is harvested annually.* ***(d)*** *The BRHR station is located at the northwest corner of Banks Island (see Figure 1). It is the northernmost WARNS station and was adopted from the BISN experiment. This is an offline solar-powered station. Data are harvested annually or as access permits.* ***(e)*** *The JNPT station was adopted from the BISN experiment and is located on the eastern coast of Banks Island (see Figure 1). This solar-powered station operates offline.* ***(f)*** *The MMPY station is located along the North Canol Road in the Yukon, southwest of Macmillan Pass. The station was adopted from the YNSN experiment and is solar-powered with a large array of panels and real-time data telemetry via satellite connection.*

converts the ground motion measured in analog volts into digital counts. The digitizer also handles assigning a time stamp to each data packet. Timing precision is achieved via a global positioning system (GPS) antenna connected to the digitizer to acquire satellite-based absolute time information. In modern equipment, the digitizer is often connected directly to the Internet and can accommodate real-time data streaming in addition to buffering and archiving the data on a local disk. Finally, the power system provides power to the digitizer, sensor and communications equipment. For WARNS, the power systems vary between sites and are either DC solar setups (with large battery banks) or AC grid power with a single backup battery. In this section, we briefly outline the equipment used at WARNS sites.

The following sensors are used across the range of WARNS stations: Guralp CMG-3ESP, Guralp CMG-40T, Nanometrics Trillium 120P/PA, Nanometrics Trillium 120PH (and SlimV2), Nanometrics Trillium Horizon 120 and Nanometrics Trillium Compact 120. The sensor selection for a given station depends on the local site conditions. Several of the sensors listed above are capable of direct-burial installations (i.e., the entire sensor is buried in soil/sediment). However, these direct-burial instruments are impractical when rock is at surface. In these circumstances, a vault-style instrument would be employed (e.g., CMG-3ESP, CMG-40T, or Trillium 120P/PA). Notably, the vault-style instruments have been used in the tundra, even when rock is not at surface. In these instances, a pit is excavated (approximately 1 m deep), and a large-diameter culvert is placed vertically within the pit to create a protective housing for the sensor. In some cases, sand is used to level the base of the pit, and a large flat rock or patio stone is used as a platform for the sensor. The range of digitizers paired with these sensors include Nanometrics Trident, Nanometrics Taurus, Nanometrics Centaur and Nanometrics Pegasus. In most cases, the seismic equipment used for WARNS stations was reused from past temporary seismic experiments (e.g., POLARIS) or loaned from interested academic collaborators.

Some stations in WARNS operate without data streaming (i.e., offline). The Taurus, Centaur and Pegasus digitizers are used for these stations because they can accommodate large flash storage volumes to maintain a local data archive. Depending on the size of the flash media and the noise conditions of the site, approximately two to three years' worth of continuous seismic recordings can be collected without concern of data loss. In practice, a station would never intentionally be left operating offline for this length of time due to the numerous challenges in collecting reliable data (discussed above). Typically, an offline station is visited once per year to harvest data and facilitate a local disk change, as well as perform upkeep and maintenance on the site equipment. However, there are circumstances when a station is not accessible during a scheduled visit (e.g., due to inclement weather preventing departure from the base of operations or landing at the remote site). In these cases, site visits are postponed until the next available flight window, or even to the following year. At present, there are five stations operating offline within WARNS: BRHR (Fig. 7d), MTBLK, SENTN, RICHY (Fig. 7c) and STOKY. The now-decommissioned JNPT station (Fig. 7e) illustrates an alternative compact station design used for WARNS.

The power systems used at WARNS stations are relatively simple and include DC solar and AC mains power. Stations located within communities use AC mains power as it substantially reduces station complexity, including maintenance requirements. A deep-cycle Absorbent Glass Mat (AGM) battery with a charger/maintainer is also connected to serve as a temporary backup DC power source in case grid power is lost. In remote northern communities that produce electricity from diesel generators, short power surges or brownouts occur frequently. The battery backup helps to ensure continuity in station operation. These simple backup power sources can keep a station operating for five to seven days without grid power. The typical power system for remote WARNS stations is solar power. This includes a battery bank on the order of 1000 amp-hours composed of AGM or Gel-cell lead-acid batteries. The battery bank is connected to a solar array ranging from 200 to 400 W using a solar controller. The battery bank is insulated to reduce temperature fluctuations, and in some circumstances, a small electric heater is added inside the battery/station enclosure.

Real-time data streaming for WARNS is accomplished in several ways. The simplest communications consist of a cellular modem colocated at the station, providing a direct data connection for the digitizer. The data are then streamed in real time from the remote site location to the GSC-PDC. In several locations, cellular communications are facilitated through collaboration with other Government of Canada departments operating other scientific equipment. Currently, three WARNS stations stream over cellular connections: TUKN, ULUN and NOWN (Fig. 7a). Colocation of stations with other agencies' research equipment also provides additional technical personnel and local contacts to assist with site maintenance when required. The WARNS stations

also use digital subscriber line (DSL) services, where a dedicated account and DSL modem provide internet. The site digitizer is connected to the modem and streams the data in real time back to the GSC-PDC. To date, the WARNS territorial geological survey partners (YGS and NTGS) have provided these communication services, whereby one station is currently operating in this configuration (Fig. 7b; TSIIG). In some cases, WARNS stations are colocated with other government, research or private facilities, and arrangements have been made for the seismic instruments to be connected to existing Internet services at these sites. Currently, there are four stations operating in this configuration (OGILY, KLONY, NAHA and CMBN). Furthermore, WARNS also uses satellite-based telemetry to stream data, known as very small aperture terminals (VSATs), which are configurations of small satellite dishes capable of transmitting data while drawing relatively low power. For these stations, an additional component, Nanometrics Cygnus, is required to act as the satellite modem connecting the local digitizer (either a Trident or Centaur) to the local network back at the GSC-PDC. Currently, four of the WARNS stations stream their data using satellite connections: MMPY (Fig. 7f), TGTN, MAYO and WTLY, and an additional two are planned to be brought online in the coming years.

The near future holds interesting possibilities for the simplification of real-time communications at remote sites. Although satellite-based communications require less power, the dish can be susceptible to damage from wind or wildlife. Additionally, the agreements for these services are costly. With the upcoming implementation of direct-to-cell satellite services, remote seismic stations can be switched online using standard cellular modems equipped with SIM cards capable of connecting to satellite-LTE networks. This will be beneficial in terms of simplifying and reducing the footprint size of the site. Furthermore, there is a cost benefit with the increase in overall data transfer bandwidth.

As indicated above, all online WARNS stations stream their data in real time to the GSC-PDC and have typical latencies of two to five seconds. These data are then immediately streamed to the EarthScope Data Management Centre (previously IRIS DMC), making these raw data freely available (i.e., open access). For the offline stations, the data are processed into a common format and manually uploaded to the EarthScope DMC after returning from site visits. The stations under the banner of WARNS belong to the network code PQ, which is the research network for the Public Safety Geoscience Program of the Pacific division of the GSC (Geological Survey of Canada, 2013).

The data quality for sites across WARNS varies between locations and is dependent upon the installation type, sensor, as well as local noise conditions (e.g., within a community or located near the coast). In general, the data quality of WARNS stations is good and equivalent to other long-term broadband stations. Figures 8 and 9 illustrate probabilistic power spectral densities (PPSD) for stations TUKN and WTLY, respectively. The grey lines denote the bounds of the new, high and low-noise models (Peterson, 1993). These represent a globally averaged range of expected background ambient seismic noise across different frequencies. The PPSD for each station illustrates the long-term average site conditions in the context of the global range. The lower the PPSD level (near the lower bound of the noise model), the quieter the site is. Presumably, this leads to a higher-quality station where low-amplitude signals can be detected among the background noise. Conversely, the higher the PPSD level, the noisier the site, that is, the PPSD is not only influenced by nearby sources of Earth vibrations. The site construction, shelter and local subsurface geology (e.g., soft sedimentary material) can also influence the baseline performance of a seismic station.

Figure 8 illustrates the PPSD and spectrogram for station TUKN, located within the Hamlet of Tuktoyaktuk, Northwest Territories, on the coast of the Arctic Ocean. This site consists of a Trillium 120PH (direct-burial sensor) installed within a sand pit on a small (several metres high) bluff overlooking the bay. The site has reasonable lower noise conditions at periods of 1 to 50 s.

We observe greater variance in (and generally higher) noise levels at longer and shorter periods. High-frequency noise is likely attributed to the station location, which is within the community, near a road and within 5 m of the beach. The noise levels at longer periods are more difficult to explain. Seasonally, global ambient seismic noise at periods >1 s is attributed to ocean storm activity, and stations in the northern hemisphere experience higher noise levels during winter months (Li et al., 2022). We note the opposite seasonal trend in Figure 8, where noise levels are often lower by 40 to 60 dB during winter months. As much of the western Canadian Arctic is underlain by permafrost, the observed seasonality in the PPSD for station TUKN may be due to fluctuations in air temperature that lead to changes in soil rigidity (i.e., seasonal thawing of the

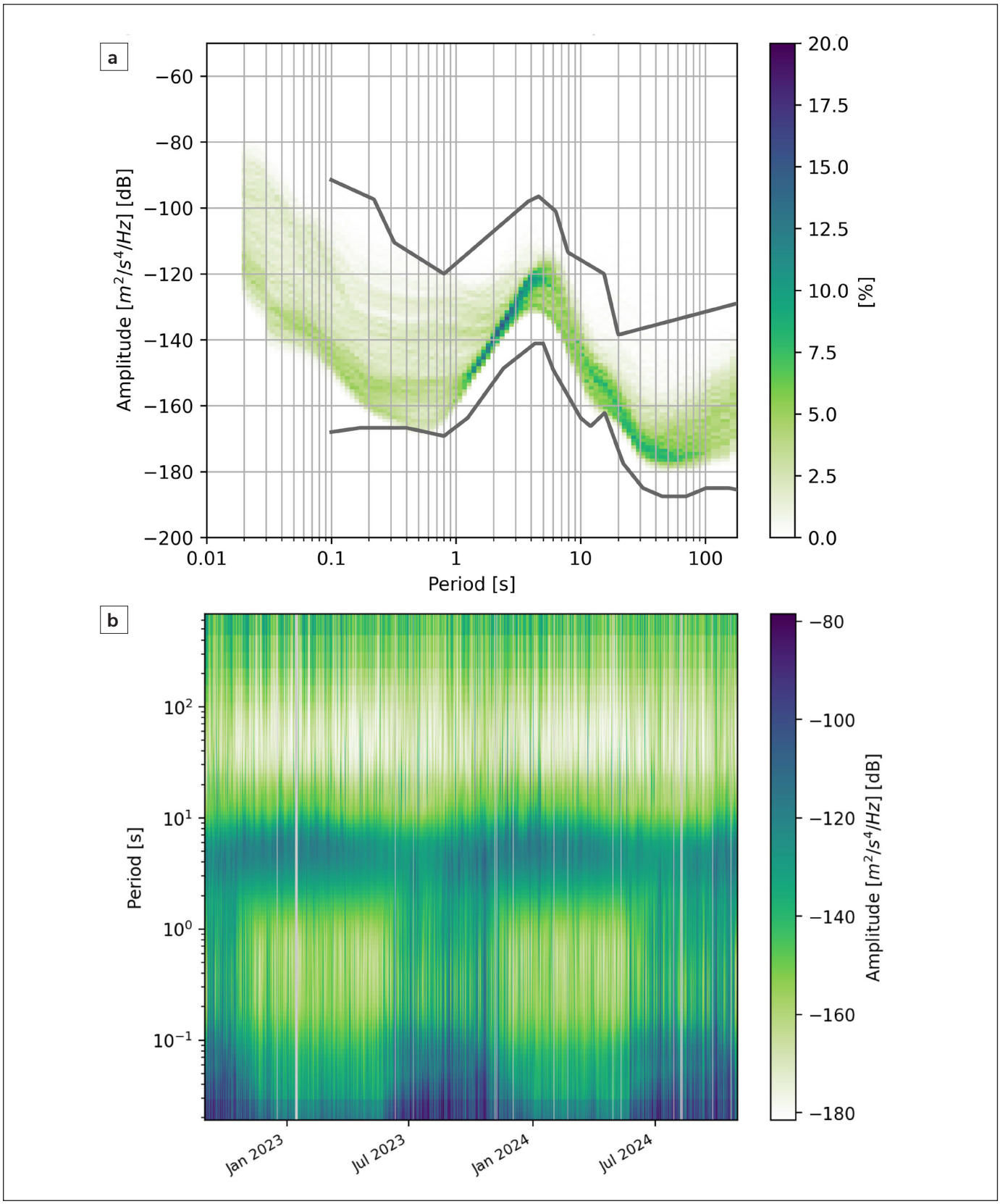

Figure 8. *Probabilistic power spectral density* **(a)** *and spectrogram* **(b)** *of ambient seismic noise for station TUKN. Upper and lower grey lines in (a) represent the new high and low-noise models, respectively (Peterson, 1993).*

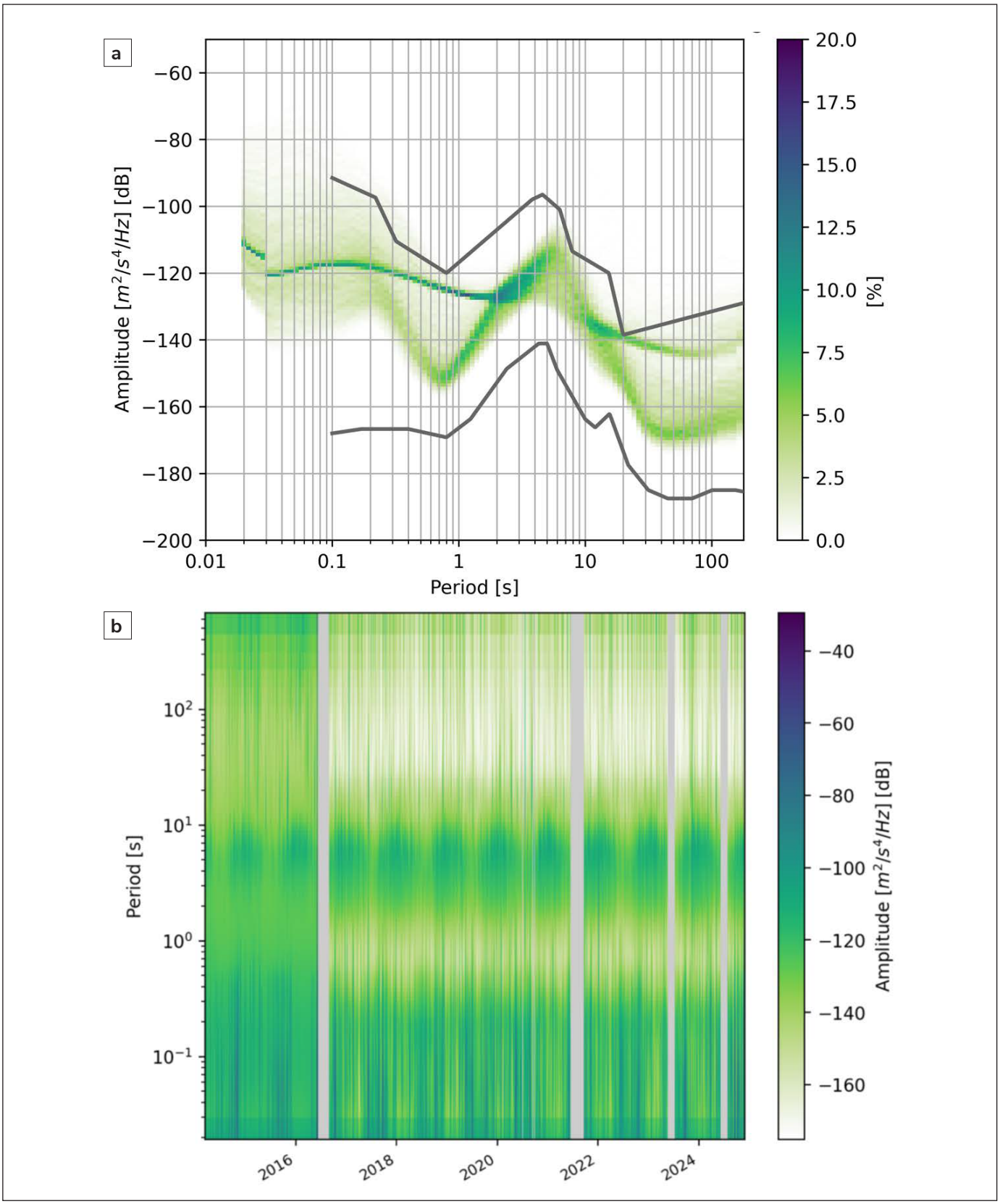

Figure 9. *Probabilistic power spectral density* ***(a)*** *and spectrogram* ***(b)*** *of ambient seismic noise for station WTLY. Upper and lower grey lines in (a) represent the new high and low-noise models, respectively (Peterson, 1993).*

active layer), resulting in dramatically different site conditions (geophysically) throughout the year.

Figure 9 illustrates the PPSD and spectrogram for station WTLY, located near the community of Watson Lake, Yukon, at the outer limits of the local airport. Though the airport does not experience regular traffic, it does serve as a base of operations for wildfire services for southern Yukon and northern British Columbia. The sensor at WTLY is a Trillium 120PH (direct-burial sensor) installed within the unconsolidated sediments located approximately 20 m away from the edge of a lake. The PPSD for WTLY exhibits similar patterns as TUKN, with higher noise levels at high frequencies (short periods). Figure 9 also illustrates variations in data quality due to technical challenges and installation. A secondary band is observed in the PPSD plot at systematically higher levels across all periods, which coincides with the early deployment period shown in the spectrogram plot before late 2016. Recorded background noise levels decreased significantly after the sensor was repaired and reinstalled.

Concluding remarks

Though vast and remote, the Canadian north is gaining an increased awareness due to improved accessibility, development interests and the impacts of climate change. The continued study of geohazards in the Canadian north is important for addressing the needs and security of northerners. The collaborative efforts between Canadian academic groups, territorial governments and the federal government have led to the development and successful operation of seismic networks in northwestern Canada, including WARNS. This initiative would not exist today without the support and contributions from a broad and diverse group during the last decade (see Acknowledgments). The WARNS program will continue to provide important open-source seismological data (mostly in real time) that enables improved earthquake monitoring and geoscientific discovery in northern Canada. As the will and the means permit, WARNS will continue to expand in the coming years to help address unresolved (and evolving) tectono-climactic questions, and will help Canada adapt to future environmental conditions.

Acknowledgments

We respectfully acknowledge that many of the seismic stations of WARNS are installed on the Traditional Territories of Indigenous Peoples of Canada. Summer 2025 will mark 10 years since the initial deployment of BISN stations. This report provides an opportunity to acknowledge and thank the many individuals who have contributed to the development and maintenance of the various seismic networks deployed in northwestern Canada that is discussed in this work, and which led to the inception of WARNS. Contributions include fieldwork assistance, logistics support, in-kind support and provision of equipment. Our thanks and acknowledgements are extended to: David Snyder (retired), Roger MacLeod, Riddhi Dave, Peter Morse, Jiri Raska, Lisa Nykolaishen and Mingzhou Li (NRCan); Justin Emberley (formerly YGS); Hendrick Falck (NTGS); Clement Estève (University of Vienna); Justin Strauss and Marisa Palucis (Dartmouth College); Yajing Liu (McGill University); Fiona Darbyshire (Université du Québec à Montréal); Michael Bostock (University of British Columbia); Quinn Worthington and Joel Cubley (Yukon University); Rick Moore and Marian Jusko (Nanometrics Inc.); Stephen Mosher (formerly University of Ottawa); Edwin Nissen (University of Victoria); Stephane Poitras (formerly NTGS); Michael Schmidt (CANImage). We also thank Dr. Jan Dettmer for his critical review of this manuscript.

Data and code availability

The seismological datasets discussed in this article are freely available, either upon request from the authors, or from the EarthScope Data Management Centre. The facilities of EarthScope Consortium were used to access waveforms, related metadata and/or derived products used in this study. These services are funded through the National Science Foundation's Seismological Facility for the Advancement of Geoscience (SAGE) Award under Cooperative Agreement EAR-1724509.

References

Aster, R., Beaudoin, B., Hole, J., Fouch, M., Fowler, J. and James, D., 2005. IRIS seismology program marks 20 years of discovery. EOS, Transactions American Geophysical Union, vol. 86, no. 17, p. 171–172.

Audet, P., Currie, C.A., Schaeffer, A.J. and Hill, A.M., 2019. Seismic evidence for lithospheric thinning and heat in the Northern Canadian Cordillera. Geophysical Research Letters, vol. 46, no. 8, p. 4249–4257.

Audet, P. and Ma, S., 2018. Deep crustal earthquakes in the Beaufort Sea, western Canadian Arctic, from teleseismic depth phase analysis. Seismological Research Letters, vol. 89, no. 4, p. 1379–1384.

Baker, M.G., Heath, D.C., Schutt, D.L., Aster, R.C., Cubley, J.F. and Freymueller, J.T., 2020. The Mackenzie Mountains EarthScope project: Studying active deformation in the northern North American Cordillera from margin to craton. Seismological Research Letters, vol. 91, no. 1, p. 521– 532.

Biegel, K.M., Gosselin, J.M., Dettmer, J., Colpron, M., Enkelmann, E. and Caine, J.S., 2024. Earthquake relocations delineate a discrete fault network and deformation corridor throughout southeast Alaska and southwest Yukon. Tectonics, vol. 43, issue 5, e2023TC008140, https://doi.org/10.1029/2023TC008140

Bruhn, R.L., Sauber, J., Cotton, M.M., Pavlis, T.L., Burgess, E., Ruppert, N. and Forster, R.R., 2012. Plate margin deformation and active tectonics along the northern edge of the Yakutat terrane in the Saint Elias orogen, Alaska, and Yukon, Canada. Geosphere, vol. 8, no. 6, p. 1384– 1407.

Busby, R.W. and Aderhold, K., 2020. The Alaska Transportable Array: As built. Seismological Research Letters, vol. 91, no. 6, p. 3017–3027.

Cassidy, J.F. and Bent, A.L., 1993. Source parameters of the 29 May and 5 June 1940 Richardson Mountains, Yukon Territory, earthquakes. Bulletin of the Seismological Society of America, vol. 83, no. 3, p. 636–659.

Cassidy, J.F. and Mulder, T.L., 2023. Seismicity and seismic monitoring of Canada's volcanic zones. Canadian Journal of Earth Sciences, vol. 61, no. 2, p. 248–269.

Cassidy, J.F., Rogers, G.C. and Ristau, J., 2005. Seismicity in the vicinity of the SNORCLE corridors of the northern Canadian Cordillera. Canadian Journal of Earth Sciences, vol. 42, no. 6, p. 1137–1148.

Choi, M., Eaton, D.W. and Enkelmann, E., 2021. Is the eastern Denali fault still active? Geology, vol. 49, no. 6, p. 662–666.

Doser, D.I., 2014. Seismicity of southwestern Yukon, Canada, and its relation to slip transfer between the Fairweather and Denali fault systems. Tectonophysics, vol. 611, p. 121–129.

Drooff, C. and Freymueller, J.T., 2023. New insights into the active tectonics of the northern Canadian Cordillera from an enhanced earthquake catalog. Journal of Geophysical Research: Solid Earth, vol. 128, issue 12, e2023JB026793, https://doi.org/10.1029/2023JB026793

Eaton, D.W., Adams, J., Asudeh, I., Atkinson, G.M., Bostock, M.G., Cassidy, J.F., Ferguson, I.J., Samson, C., Snyder, D.B., Tiampo, K.F. and Unsworth, M.J., 2005. Investigating Canada's lithosphere and earthquake hazards with portable arrays. EOS, Transactions American Geophysical Union, vol. 86, issue 17, p. 169–173.

Eberhart-Phillips, D., Christensen, D.H., Brocher, T.M., Hansen, R., Ruppert, N.A., Haeussler, P.J. and Abers, G.A., 2006. Imaging the transition from Aleutian subduction to Yakutat collision in central Alaska, with local earthquakes and active source data. Journal of Geophysical Research: Solid Earth, vol. 111, no. B11, 31 p.

Eberhart-Phillips, D., Haeussler, P.J., Freymueller, J.T., Frankel, A.D., Rubin, C.M., Craw, P., Ratchkovski, N.A., Anderson, G., Carver, G.A., Crone, A.J., Dawson, T.E., Fletcher, H., Hansen, R., Harp, E.L., Harris, R.A., Hill, D.P., Hreinsdóttir, S., Jibson, R.W., Jones, L.M., Kayen, R., Keefer, D.K., Larsen, C.F., Moran, S.C., Personius, S.F., Plafker, G., Sherrod, B., Sieh, K., Sitar, N. and Wallace, W.K., 2003. The 2002 Denali fault earthquake, Alaska: A large magnitude, slip-partitioned event. Science, vol. 300, no. 5622, p. 1113–1118.

Enkelmann, E., Finzel, E. and Arkle, J., 2019. Deformation at the eastern margin of the northern Canadian Cordillera: Potentially related to opening of the north Atlantic. Terra Nova, vol. 31, no. 3, p. 151–158.

Enkelmann, E., Garver, J.I. and Pavlis, T.L., 2008. Rapid exhumation of ice-covered rocks of the Chugach–St. Elias orogen, southeast Alaska. Geology, vol. 36, no. 12, p. 915–918.

Estève, C., Audet, P., Schutt, D., Aster, R., Schaeffer, A. and Cubley, J., 2023. Structure, origin, and deformation of the lithosphere in the Northern Canadian Cordillera from high-resolution, passive-source seismic velocity models. *In*: Tectonics and Seismicity of Alaska and Western Canada, AGU Geophysical Monograph, N.A. Ruppert, M.A. Jadamec and J.T. Freymueller (eds.), vol. 290, American Geophysical Union, Washington, DC.

Estève, C., Gosselin, J., Audet, P., Schaeffer, A., Schutt, D. and Aster, R., 2021. Surface-wave tomography of the Northern Canadian Cordillera using earthquake Rayleigh wave group velocities. Journal of Geophysical Research: Solid Earth, vol. 126, issue 8, https://doi.org/10.1029/2021JB021960

Estève, C., Liu, Y., Koulakov, I., Schaeffer, A.J. and Audet, P., 2022. Seismic evidence for a weakened thick crust at the Beaufort Sea continental margin. Geophysical Research Letters, vol. 49, issue 16, e2022GL100158, https://doi.org/10.1029/2022GL100158

Finzel, E.S., Trop, J.M., Ridgway, K.D. and Enkelmann, E., 2011. Upper plate proxies for flat-slab subduction processes in southern Alaska. Earth and Planetary Science Letters, vol. 303, no. 3–4, p. 348–360.

Gabrielse, H., Murphy, D.C. and Mortensen, J.K., 2006. Cretaceous and Cenozoic dextral orogen-parallel displacements, magmatism and paleogeography, north-central Canadian Cordillera. *In*: Paleogeography of the North American Cordillera: Evidence For and Against Large-Scale Displacements, J.W. Haggart, J.W.H. Monger and R.J. Enkin (eds.), Geological Association of Canada, Special Paper 46, p. 255–276.

Gaherty, J. and Revenaugh, J., 2003. Collaborative Research: Canadian Northwest Seismic Experiment [Dataset]. International Federation of Digital Seismograph Networks. https://doi.org/10.7914/SN/XN_2003

Gaudreau, E., Audet, P. and Schneider, D.A., 2019. Mapping Curie Depth across western Canada from a wavelet analysis of magnetic anomaly data. Journal of Geophysical Research: Solid Earth, vol. 125, p. 4365–4385.

Geological Survey of Canada, 2013. Public Safety Geoscience Program Canadian Research Network [Dataset]. International Federation of Digital Seismograph Networks. https://doi.org/10.7914/SN/PQ

Gosselin, J.M., Biegel, K., Hamidbeygi, M. and Dettmer, J., 2023. Improvements in the regional earthquake focal mechanism catalogue for southwestern Yukon. *In:* Yukon Exploration and Geology 2022, K.E. MacFarlane (ed.), Yukon Geological Survey, p. 63–76 (plus digital appendices).

Gosselin, J.M., Biegel, K.M., Dettmer, J., Hersh, G., Colpron, M. and Enkelmann, E., 2024. Crustal stress near the Yakutat microplate collision from probabilistic earthquake focal mechanisms. Canadian Journal of Earth Sciences, e-First. https://doi.org/10.1139/cjes-2024-0095

Grasby, S.E., Jessop, A., Kelman, M., Ko, M., Chen, Z., Allen, D.M., Bell, S., Ferguson, G., Majorowicz, J., Moore, M., Raymond, J. and Therrien, R., 2011. Geothermal energy resource potential of Canada. Geological Survey of Canada, Open File 6914, 322 p., https://doi.org/10.4095/288745

Hasegawa, H., Chou, C. and Basham, P., 1979. Seismotectonics of the Beaufort Sea. Canadian Journal of Earth Sciences, vol. 16, no. 4, p. 816–830.

Hoggard, M.J., Czarnota, K., Richards, F.D., Huston, D.L., Jaques, A.L. and Ghelichkhan, S., 2020. Global distribution of sediment-hosted metals controlled by craton edge stability. Nature Geoscience, vol. 13, no. 7, p. 504–510.

Horner, R., Wetmiller, R., Lamontagne, M. and Plouffe, M., 1990. A fault model for the Nahanni earthquakes from aftershock studies. Bulletin of the Seismological Society of America, vol. 80, no. 6A, p. 1553–1570.

Hyndman, R., 2010. The consequences of Canadian Cordillera thermal regime in recent tectonics and elevation: A review. Canadian Journal of Earth Sciences, vol. 47, no. 5, p. 621–632.

Hyndman, R., 2023. The thermal regime of NW Canada and Alaska, and tectonic and seismicity consequences. Geochemistry, Geophysics, Geosystems, vol. 24, issue 7. https://doi.org/10.1029/2022GC010570

Hyndman, R., Cassidy, J., Adams, J., Rogers, G. and Mazzotti, S., 2005. Earthquakes and seismic hazard in the Yukon-Beaufort-Mackenzie. Canadian Society of Exploration Geophysicists Recorder, vol. 30, no. 5, p. 32–66.

Kolaj, M., Adams, J. and Halchuk, S., 2020. The 6th generation seismic hazard model of Canada. In 17th World Conference on Earthquake Engineering, p. 1–12.

Lane, L.S., 2002. Tectonic evolution of the Canadian Beaufort Sea–Mackenzie Delta region: A brief review. Canadian Society of Exploration Geophysicists Recorder, vol. 27, no. 2, p. 49–56.

Larsen, J.N. and Huskey, L., 2015. The Arctic economy in a global context. *In*: The New Arctic, B. Evengård, J. Nymand Larsen and Ø. Paasche (eds.), Springer Cham, p. 159–174, Cham. https://doi.org/10.1007/978-3-319-17602-4_12

Lawley, C.J., McCafferty, A.E., Graham, G.E., Huston, D.L., Kelley, K.D., Czarnota, K., Paradis, S., Peter, J.M., Hayward, N., Barlow, M., Emsbo, P., Coyan, J., San Juan, C.A. and Gadd, M.G., 2022. Data–driven prospectivity modelling of sediment–hosted Zn–Pb mineral systems and their critical raw materials. Ore Geology Reviews, vol. 141, article no. 104635.

Leonard, L.J., Mazzotti, S. and Hyndman, R.D., 2008. Deformation rates estimated from earthquakes in the northern cordillera of Canada and eastern Alaska. Journal of Geophysical Research: Solid Earth, vol. 113, article no. B08406, https://doi.org/10.1029/2007JB005456

Li, X., Xu, Y., Xie, C. and Sun, S., 2022. Global characteristics of ambient seismic noise. Journal of Seismology, vol. 26, no. 2, p. 343–358.

Mazzotti, S. and Hyndman, R.D., 2002. Yakutat collision and strain transfer across the northern Canadian Cordillera. Geology, vol. 30, no. 6, p. 495–498.

McKay, R., Enkelmann, E., Hadlari, T., Matthews, W. and Mouthereau, F., 2021. Cenozoic exhumation history of the eastern margin of the northern Canadian Cordillera. Tectonics, vol. 40, no. 4, https://doi.org/10.1029/2020TC006582

Meighan, L.N., Cassidy, J.F., Mazzotti, S. and Pavlis, G.L., 2013. Microseismicity and tectonics of southwest Yukon Territory, Canada, using a local dense seismic array. Bulletin of the Seismological Society of America, vol. 103, no. 6, p. 3341–3346.

Monger, J. and Price, R., 2002. The Canadian Cordillera: Geology and tectonic evolution. CSEG Recorder, vol. 27, no. 2, p. 17–36.

Nelson, J.L., Colpron, M. and Israel, S., 2013. The Cordillera of British Columbia, Yukon, and Alaska: Tectonics and metallogeny. *In*: Tectonics, Metallogeny, and Discovery: The North American Cordillera and Similar Accretionary Settings, M. Colpron, T. Bissig, B.G. Rusk and J.F.H. Thompson (eds.), Special Publication 17. https://doi.org/10.5382/SP.17.03

Peterson, J., 1993. Observations and modeling of seismic background noise. USGS Open File Report 93-322, p. 1–95.

Plafker, G., Thatcher, W., Freymueller, J., Haeussler, P., Wesson, R. and Ekström, G., 2008. Geological and geophysical evaluation of the mechanisms of the great 1899 Yakutat Bay earthquakes. *In*: Active Tectonics and Seismic Potential of Alaska, J.T. Freymueller, P.J. Haeussler, R.L. Wesson and G. Ekström (eds.), vol. 179, p. 215–236.

Rantanen, M., Karpechko, A.Y., Lipponen, A., Nordling, K., Hyvärinen, O., Ruosteenoja, K., Vihma, T. and Laaksonen, A., 2022. The Arctic has warmed nearly four times faster than the globe since 1979. Communications Earth & Environment, vol. 3, article no. 168.

Ristau, J., Rogers, G.C. and Cassidy, J.F., 2007. Stress in western Canada from regional moment tensor analysis. Canadian Journal of Earth Sciences, vol. 44, no. 2, p. 127–148.

Russell, J.K., Edwards, B.R., Williams-Jones, G. and Hickson, C.J., 2023. Pleistocene to Holocene volcanism in the Canadian Cordillera. Canadian Journal of Earth Sciences, vol. 60, no. 10, p. 1443–1466.

Schaeffer, A. and Lebedev, S., 2014. Imaging the North American continent using waveform inversion of global and US Array data. Earth and Planetary Science Letters, vol. 402, p. 26–41.

Schutt, D.L., Porritt, R.W., Estève, C., Audet, P., Gosselin, J.M., Schaeffer, A.J., Aster, R.C., Freymueller, J.T. and Cubley, J.F., 2023. Lithospheric S wave velocity variations beneath the Mackenzie Mountains and Northern Canadian Cordillera. Journal of Geophysical Research: Solid Earth, vol. 128, no. 1, https://doi.org/10.1029/2022JB025517

Smith, S.L. and Burgess, M.M., 2004. Sensitivity of permafrost to climate warming in Canada. Geological Survey of Canada, Bulletin 579, 24 p., https://doi.org/10.4095/216137

Tesauro, M., Kaban, M.K., Mooney, W.D. and Cloetingh, S.A., 2014. Density, temperature, and composition of the North American lithosphere—new insights from a joint analysis of seismic, gravity, and mineral physics data: 2. Thermal and compositional model of the upper mantle. Geochemistry, Geophysics, Geosystems, vol. 15, issue 12, p. 4808–4830.

Vogel, B. and Bullock, R.C., 2021. Institutions, indigenous peoples, and climate change adaptation in the Canadian Arctic. GeoJournal, vol. 86, no. 6, p. 2555–2572.

Waldien, T.S., Roeske, S.M. and Benowitz, J.A., 2021. Tectonic underplating and dismemberment of the Maclaren-Kluane Schist records Late Cretaceous terrane accretion polarity and ~480 km of post-52 Ma dextral displacement on the Denali fault. Tectonics, vol. 40, e2020TC006677, https://doi.org/10.1029/2020TC006677

Wetmiller, R., Horner, R., Hasegawa, H., North, R., Lamontagne, M., Weichert, D. and Evans, S., 1988. An analysis of the 1985 Nahanni earthquakes. Bulletin of the Seismological Society of America, vol. 78, no. 2, p. 590–616.

Stratigraphic context for reef-building microbialites in the Tonian Reefal assemblage (Fifteenmile Group) of the Yukon

*Charlotte Spruzen**
McGill University

Katie M. Maloney
Royal Ontario Museum

J. Wilder Greenman
Dalhousie University

Maxwell A. Lechte
University of Melbourne

Galen P. Halverson
McGill University

Spruzen, C., Maloney, K.M., Greenman W.J., Lechte, M.A. and Halverson, G.P., 2025. Stratigraphic context for reef-building microbialites in the Tonian Reefal assemblage (Fifteenmile Group) of the Yukon. *In*: Yukon Exploration and Geology Technical Papers 2024, L.H. Weston, A. Stuart, S.K. Schultz, A.D. Brubacher and D.C. Cronmiller (eds.), Yukon Geological Survey, p. 75–95.

Abstract

The Tonian Period (1000–720 Ma) likely represents a critical transition in microbial reef construction, given the emergence of reefs built by thrombolites and other cavity-dense microbialites. However, there are few detailed studies on Tonian reef development to constrain this ecologically significant transformation. Here, we build on previous documentation of reefal buildups in the ca. 850–780 Ma Fifteenmile Group in the Coal Creek inlier (Ogilvie Mountains) and contribute seven new detailed stratigraphic sections featuring microbial accumulations in the Reefal assemblage. We document the stratigraphic context for these Tonian reefs and distinguish between predominantly laminated and unlaminated microbial textures. In addition, we identify rare instances of exceptional preservation of unlaminated microbialite, suggesting that reef-building microbialites of the Reefal assemblage have similar framework morphologies to those of the approximately coeval Little Dal Group in the Mackenzie Mountains.

Plain language summary

Before the evolution of animals, reefs were formed of carbonate rock built by micro-organisms. It has been suggested that around one billion years ago, these microbial reefs went through a transition from simple layered structures to complex clotted, three-dimensional frameworks. To better understand this transition, we studied an 800 to 850 million-year-old reef exposed in the Ogilvie Mountains of the Yukon, on the Traditional Territory of the Tr'ondëk Hwëch'in First Nation. We document substantial reefs that built up on uplifted topography, adjacent to a deeper-water basin of shale and carbonate rocks. We also demonstrate for the first time that these reefs were built by clotted frameworks, with strong similarities to reefs of the same age from the Northwest Territories.

* charlotte.spruzen@mail.mcgill.ca

Introduction

It has been suggested that the Tonian Period represents a pivotal point in reef evolution, during which thrombolites and cavity-dense microbialite frameworks became volumetrically important reef-builders for the first time (Grotzinger and James, 2000; James and Jones, 2015). This hypothesis was largely based on observations from the Tonian Little Dal Group of the Mackenzie Mountains (Northwest Territories; Fig. 1), specifically the Stone Knife and Silverberry formations, which contain reefs built by a consortium of shallow-water stromatolites (Batten et al., 2004) and deep-water calcimicrobes (Turner et al., 1993, 1997, 2000). The Fifteenmile Group is thought to correlate with the Little Dal Group based on lithostratigraphic and chemostratigraphic correlations integrated with available geochronological constraints (Macdonald et al., 2012; Thomson et al., 2015a, b). Therefore, further investigation into the timing of reef development and the nature of reef-building organisms in the Reefal assemblage could aid in correlating Tonian strata across northwestern Canada and provide additional insight into the evolution of Neoproterozoic reef complexity.

The Reefal assemblage is a mixed carbonate-siliciclastic formation within the Tonian Fifteenmile Group in the Coal Creek and Tatonduk inliers of central western Yukon (Fig. 1 ; Macdonald et al., 2010b, 2012; Halverson et al., 2012). This formation is considered to record platformal reef development on the footwall of normal faults and successive shale-to-carbonate transitions in the adjacent basin, reflecting transgressive-regressive sequences (Macdonald et al., 2012). The shales and slope carbonates of the Reefal assemblage have been the subject of detailed studies, including investigations of carbonate carbon isotope ($\delta^{13}C_{carb}$) variability and the onset of the global Bitter Springs negative carbon isotope anomaly (Coal Creek inlier; Macdonald et al., 2010a), as well as paleoredox geochemistry of black shales (Coal Creek inlier; Sperling et al., 2013 ; Gibson et al., 2020) and apatitic scale microfossils (age-equivalent assemblage in the Tatonduk inlier; Cohen et al., 2017).

In this report, we present stratigraphic sections of the Fifteenmile Group from the Coal Creek inlier, with a focus on the Reefal assemblage (Fig. 2). Previous authors have described the Proterozoic geology of the inlier (Green, 1972; Thompson and Roots, 1982; Thompson et al., 1994; Strauss et al., 2014) and the basin-scale reef stratigraphy of the Reefal assemblage (Macdonald and Roots, 2010; Macdonald et al., 2010b, 2012; Halverson et al., 2012). In this study we focus on documenting microbialite facies within their stratigraphic context. We observe a substantial prograding platformal reef system that is largely composed of framework-constructing microbialites.

Geological history

The Yukon block is a crustal promontory on the northwest corner of Laurentia, bound to the east by the Richardson fault array and to the south by the Dawson thrust fault (Fig. 1a). Neoproterozoic strata of the Yukon block are exposed in a series of inliers and broadly correlate across them, as well as with thick Neoproterozoic successions in the Mackenzie Mountains to the east, and the Amundsen basin (including the Minto Inlier and the Brock Inlier) to the northeast (Rainbird et al., 1996; Thomson et al., 2015a, b; Greenman et al., 2020). These strata were originally divided into three sequences (A, B and C) based on major unconformities that can be correlated across the region (Young et al., 1979). In the Coal Creek inlier, these strata range in age from the polydeformed siliciclastic-carbonate succession of the ca. 1600 Ma Wernecke Supergroup (sequence A; Young et al., 1979; Thorkelson et al., 2005; Furlanetto et al., 2013) to the Ediacaran Rackla Group of sequence C (Busch et al., 2021).

Sequence B (ca. 1.2–0.8 Ga) begins with the Pinguicula Group, a siliciclastic-carbonate succession that unconformably overlies the Wernecke Supergroup and the Hart River sills (Medig et al., 2016). The age of the Pinguicula Group has recently been hypothesized to be ca. 1.1 Ga based on correlation with the Amundsen and Bylot basins (Greenman et al., 2021). In the Ogilvie Mountains, the Pinguicula Group is unconformably overlain by the Fifteenmile Group, which was originally divided into 'upper' and 'lower' subgroups with five and three map units, respectively (Thompson et al., 1994). More recently, four distinct formations were defined within the Fifteenmile Group in the Coal Creek inlier (Halverson et al., 2012; Kunzmann et al., 2014), which together record a series of coherent transgressive-regressive cycles without major unconformities. The informal Gibben formation is characterized by a shallowing-up succession that progresses from wavy laminated dolomudstone containing common molar-tooth structure, to shallow marine oolitic grainstones and tidal flat, microbially laminated carbonates (Macdonald et al., 2012; Kunzmann et al., 2014). The upper subaerial exposure surface of the Gibben formation is conformably overlain by deltaic facies of the formalized Chandindu Formation (Kunzmann et al., 2014), comprising predominantly maroon to green-weathering siltstone including shale to siltstone to

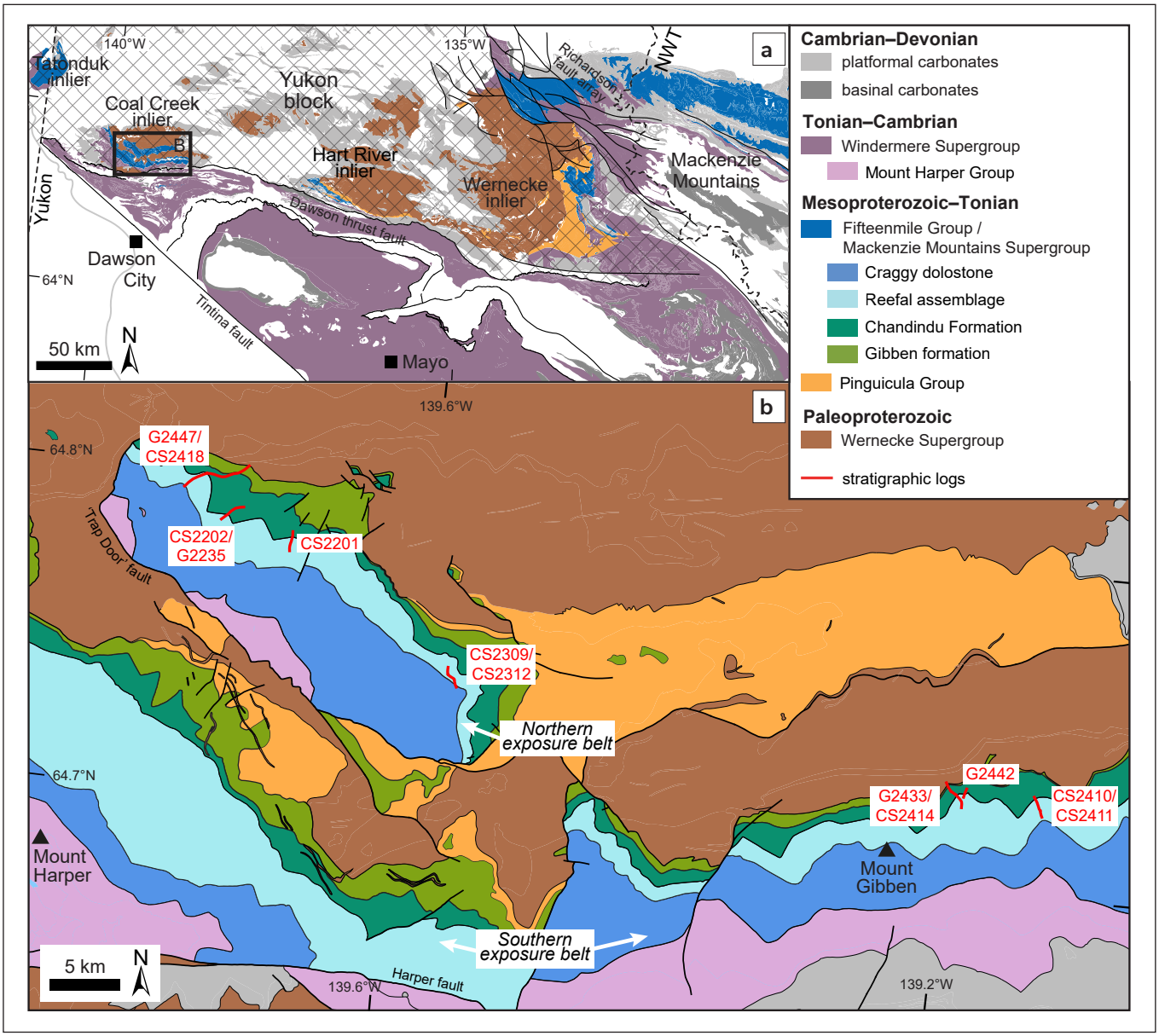

Figure 1. *Geology of the study area:* ***(a)*** *Simplified geological map of Proterozoic strata in the Yukon and Northwest Territories (after Colpron et al., 2016), delineating the location of the study area (Coal Creek inlier) relative to other Proterozoic inliers.* ***(b)*** *Inset of (a); geological map of the Coal Creek inlier (after Strauss et al., 2014). Legend is the same as (a), except for the Fifteenmile Group, which is separated into its four constituent formations. Stratigraphic sections measured as part of this study are denoted in red. The study area has been annotated to show two belts of exposure separated by the 'Trap Door' fault (Strauss et al., 2015).*

dolostone cycles, as well as horizons of stromatolitic dolostone and channelized sandstone (Macdonald et al., 2012; Kunzmann et al., 2014). An abrupt contact characterized by a dark, organic-rich shale, and most pronounced in proximal settings, marks a major flooding surface and separates the Chandindu Formation from the Reefal assemblage (Macdonald et al., 2012). The abrupt re-establishment of marine conditions is followed by the development of a platformal reef system (Halverson et al., 2012; Macdonald et al., 2012), which is the topic of this contribution. The upper contact of the Reefal assemblage is a subaerial exposure surface, which is overlain by the heavily recrystallized and silicified grainstones and debrites of the Craggy dolostone, interpreted to record progradation of a thick, laterally extensive carbonate platform (Halverson et al., 2012; Macdonald et al., 2012).

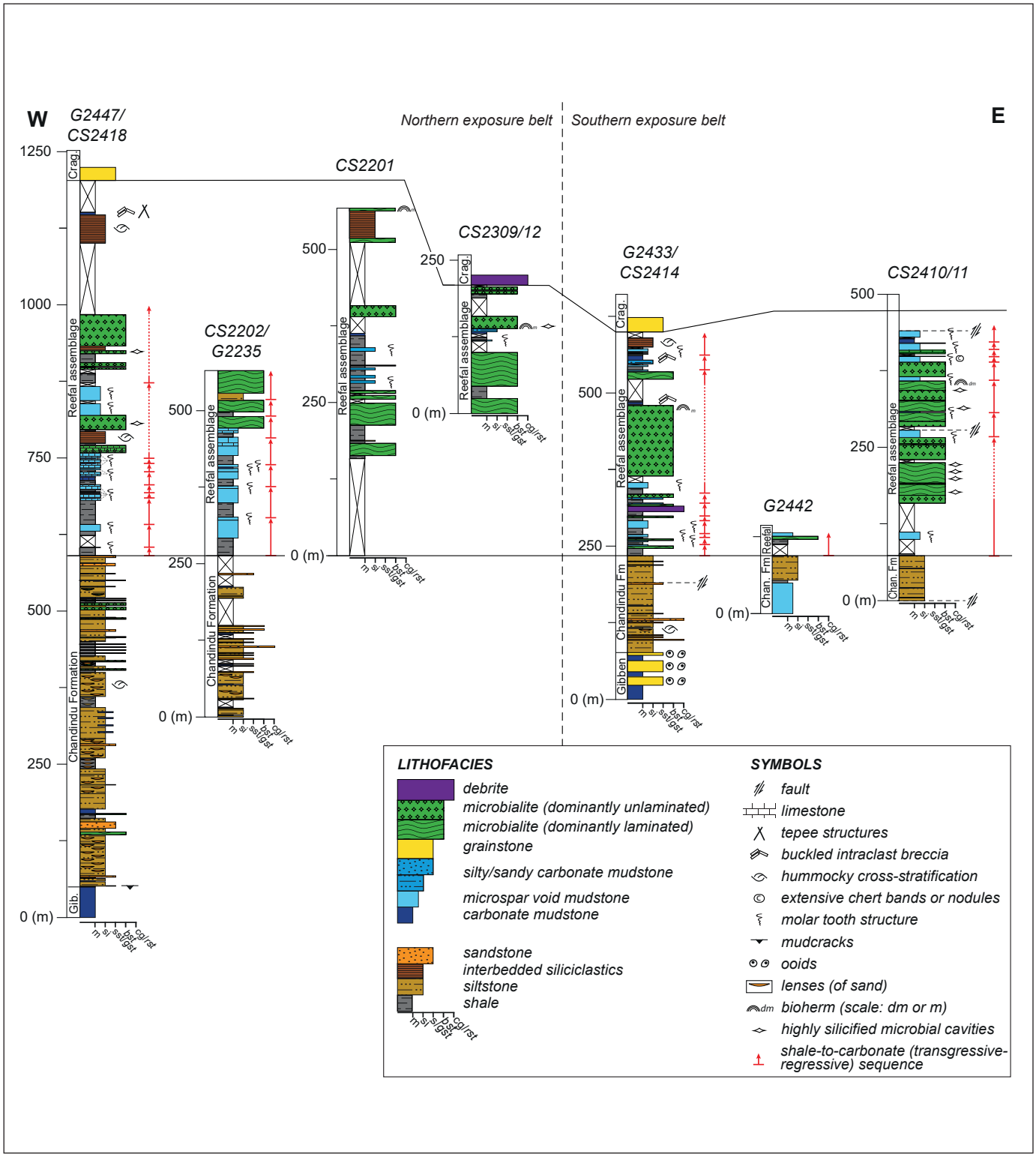

Figure 2. *Logs of stratigraphic sections measured through the Fifteenmile Group. Section locations are denoted in Figure 1b, and their coordinates are listed in Table 2. The x-axes refer to increasing grain size of siliciclastic rocks (m: mudstone, si: siltstone, sst: sandstone, cg: conglomerate) and Dunham classification of carbonates (m-si: mudstone, gst: grainstone, rst: rudstone). The y-axis refers to stratigraphic height (perpendicular to regional bedding) in metres, levelled to the Chandindu Formation–Reefal assemblage contact. Gib.: Gibben formation, Chan.: Chandindu Formation, Crag.: Craggy dolostone, Fm: Formation.*

The Fifteenmile Group exhibits significant lateral variation in both facies and thickness of individual units, and much of this discrepancy is attributed to its deposition during a period of active extension and related growth faulting (Macdonald et al., 2012). The Gibben formation has the highest lateral variability in thickness due to its deposition during a phase of syndepositional normal faulting, which developed a horst and graben basin bathymetry (Macdonald et al., 2012). Variations in thickness and lithology continue in the overlying Chandindu Formation due to its deposition on this rift-inherited complex basin topography, as well as continued syndepositional faulting (Macdonald et al., 2012; Kunzmann et al., 2014). Coarsening-upward cycles from shale to sandstone to carbonate are common throughout the Chandindu Formation, but the carbonate facies vary significantly and range from supratidal to below storm-wave base, indicating that carbonate deposition was ongoing, accumulating locally during lapses in siliciclastic input (Kunzmann et al., 2014).

A flooding surface, marked by deposition of deeper-water, organic-rich shale, forms the base of the Reefal assemblage and is ubiquitous across the basin. Higher in the succession, the Reefal assemblage also demonstrates significant lateral variability (Macdonald et al., 2012). Though this was variably attributed to thrust repetition (Thompson et al., 1994), the conformable nature of stratigraphic contacts prompted a reinterpretation of the formation as a platformal reef system with coeval shale and carbonate deposition (Halverson et al., 2012; Macdonald et al., 2012). On inferred paleotopographic highs on the uplifted footwall of north-northwest-side-down normal faults, the Reefal assemblage consists predominantly of platformal microbialite buildups (Macdonald et al., 2012). In the basinal settings of the hanging wall, the Reefal assemblage comprises shale-to-carbonate cycles, and the predominant carbonate facies is laminated carbonate mudstone containing extensive molar-tooth structure and internal brecciation (Macdonald et al., 2012). These cycles are interpreted as transgressive-regressive sequences where highstand systems tracts correspond to progradation of the platform reefal buildups (Macdonald et al., 2012). Mass-flow deposits and olistoliths also occur in these slope-to-basinal settings (Macdonald et al., 2012).

Two radiometric ages have been obtained on the Reefal assemblage: a U-Pb zircon age of 811.51 ± 0.25 Ma from a tuff in basinal facies near the top of the Reefal assemblage in the Coal Creek inlier (Macdonald et al., 2010a), and a statistically overlapping Re-Os age of 810.7 ± 6.3 Ma from just below a fossiliferous horizon of the correlative Upper Tindir Group in the Tatonduk inlier (Cohen et al., 2017). The base of the Reefal assemblage is poorly constrained, having a maximum depositional age of ca. 1000 Ma based on U-Pb dating of detrital zircon in the Reefal assemblage and the Chandindu Formation (Gibson et al., 2021). The top is directly constrained by a 752.7 ± 5.5 Ma Re-Os age from the base of the Callison Lake Formation (Rooney et al., 2015), but the continuation of the globally correlative Bitter Springs $\delta^{13}C$ anomaly into the lower Craggy dolostone implies a minimum age constraint of ca. 800 Ma (Macdonald et al., 2010a; Halverson et al., 2022). Thus, in the absence of major unconformities within the Reefal assemblage, an age range of ca. 850–800 Ma is inferred (e.g., Gibson et al., 2020).

Lithofacies descriptions

Sections of the Fifteenmile Group were documented using carbonate (Figs. 3–5) and siliciclastic (Fig. 6) lithofacies, described in Table 1. The carbonate lithofacies were based broadly on Dunham's classification scheme, including an internal division in the categories of boundstone and mudstone. Given the lack of observable features in many outcrop faces of the Reefal assemblage, it was impractical to use established terms such as stromatolite (Kalkowsky, 1908) or thrombolite (Aitken, 1967) to describe microbialites, because their defining features in the field—accretionary laminations radiating from a fixed surface (Semikhatov et al., 1979) and clotted mesostructure (Shapiro, 2000), respectively—could only be identified in rare cases. Therefore, we used a bimodal division of microbialites into dominantly laminated and dominantly unlaminated textures (Table 1; Fig. 4) highlighted by cavities (such as fenestrae) composed of either dolomite microspar or silica. The microbialite is locally variable, but facies are classified by the dominant features seen on a metre scale. Carbonate mudstones (calcimudstone and dolomudstones) were divided based on the presence of abundant cements, which we interpret to be pre- or syn-compaction and lithification, such as molar-tooth structure (Table 1).

Section descriptions

Southern exposure belt (east to west)

Section CS2410/11

At the base of the easternmost section, between Mount Gibben and the Chandindu River (64.7294°N, 139.1229°W; Figs. 1b and 2, Table 2), the Chandindu Formation comprises ~75 m of maroon to grey-green

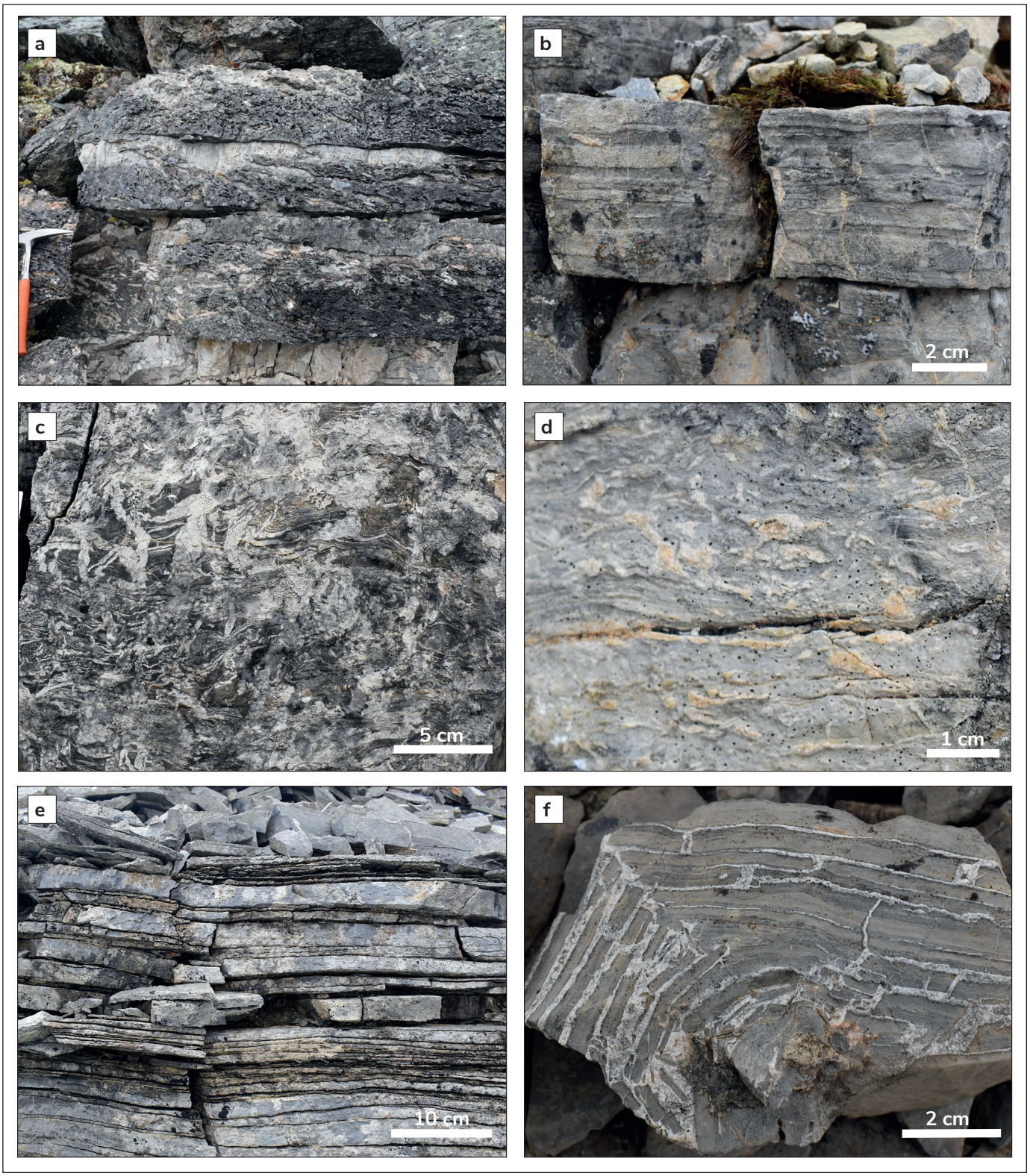

Figure 3. *Field photographs of carbonate facies of the Reefal assemblage, excluding microbialite.* ***(a)*** *Debrite beds with tabular clasts in a heavily silicified matrix. Rock hammer for scale measures ~33 cm.* ***(b)*** *Dolomudstone with thin interbeds of very fine quartz sand.* ***(c)*** *Microspar-void calcimudstone facies, with extensive molar-tooth structure distorting planar laminated dolomudstone.* ***(d)*** *Microspar-void dolomudstone facies, with round, elongate dolomite microspar cement seams.* ***(e)*** *Laminated dolomudstone.* ***(f)*** *Dolomudstone with buckled tabular internal breccia.*

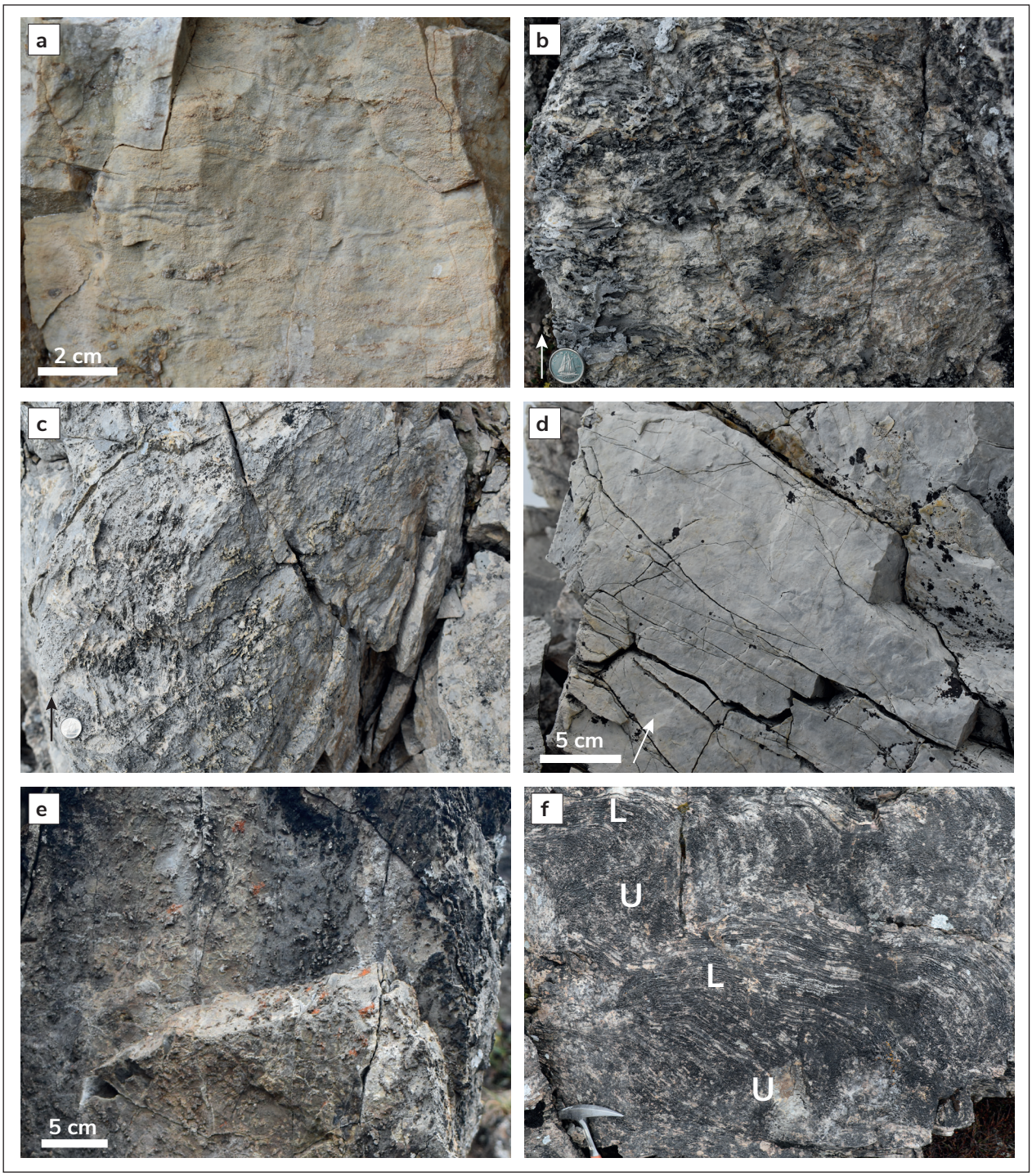

Figure 4. *Field photographs of archetypal microbialite doloboundstone of the Reefal assemblage.* ***(a)*** *Typical example of laminated microbialite doloboundstone, with faint, bedding-parallel laminations of orange-weathering microspar.* ***(b)*** *Extensively silicified microbialite doloboundstone, with prominent elongate, bedding-parallel lenses of crystalline silica (arrow denotes way-up direction). Canadian dime for scale is 1.8 cm in diameter.* ***(c)*** *Domal stromatolite defined by silicified elongate fenestrae, with laminations at a high angle to regional bedding (arrow denotes way-up direction). Canadian dime for scale.* ***(d)*** *Typical example of unlaminated microbialite doloboundstone, preserved as massive dolomite with no discernable features other than a slight mottling between shades of light grey. Arrow denotes way-up direction.* ***(e)*** *Extensively silicified unlaminated microbialite doloboundstone, with prominent, low aspect-ratio protrusions of crystalline silica.* ***(f)*** *Highly silicified microbialite bioherms that transition from unlaminated microbialite at the base and centre (U) to laminated microbialite at the outer edges (L).*

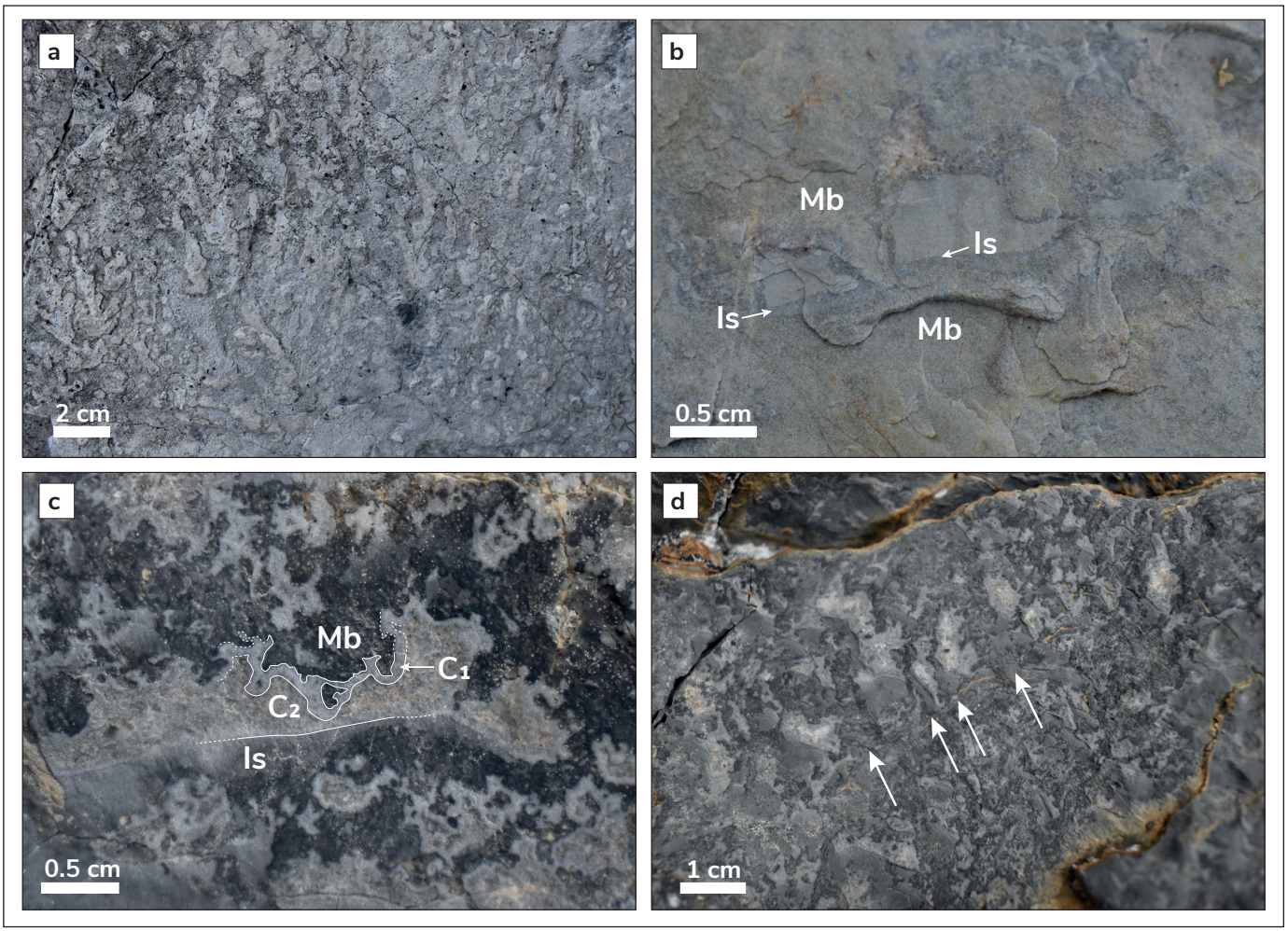

Figure 5. *Field photographs of exceptionally well-preserved microbialite boundstone of the Reefal assemblage.* ***(a)*** *Microbialite doloboundstone from stratigraphic section CS2411, with columnar, locally dendritic texture defined by a sharp distinction between light and dark dolostone, reflecting cavity space and microbialite, respectively.* ***(b)*** *Microbialite doloboundstone from stratigraphic section CS2414, with textural variation between tan-weathering microbialite (Mb) and slightly blue-tinged cavity fill. Note the layer of dark internal sediment (ls) spanning either side of the microbialite bridge bisecting the cavity.* ***(c)*** *Microbialite calciboundstone from stratigraphic section CS2418, displaying a dark, clotted microbial framework (Mb). Cavities are filled with internal sediment (ls) and two generations of cement: the first (C_1) is a <1 mm outline of the upper surface of the microbialite cavity, and the second (C_2) is a tan-weathering later-stage fill.* ***(d)*** *Wider view of the microbialite calciboundstone from stratigraphic section CS2418; arrows show local columnar growth of dark microbialite. Cavities between the columns have internal sediment and later-stage cement, creating geopetal structures.*

weathering siltstone, with rare ~5 cm interbeds of orange, laminated dolomudstone (occurring approximately every ~20 m). The base of the Reefal assemblage is marked by a distinct interval of black shale that is 3 m thick. The lowermost dolostone outcrop is microspar-void dolomudstone, with thin, bedding-parallel microspar seams and small-scale molar-tooth structure throughout. This is overlain by ~65 m of doloboundstone microbialite, which alternates between laminated microbialite with dense, prominent silicified cavities at a high angle to regional bedding; laminated microbialite with faint, elongate microspar cavities at a low angle to regional bedding; and massive microbialite with no cavities. Molar-tooth dolomudstone onlaps the top of the uppermost bed of microbialite.

The section resumes approximately 50 m to the southeast on an adjacent ridge exposure. We infer a fault with limited displacement separating the ridges, as the stratigraphic thickness of the adjacent ridge is approximately the same. The succeeding 75 m consists of a prominent outcrop of primarily microbialite

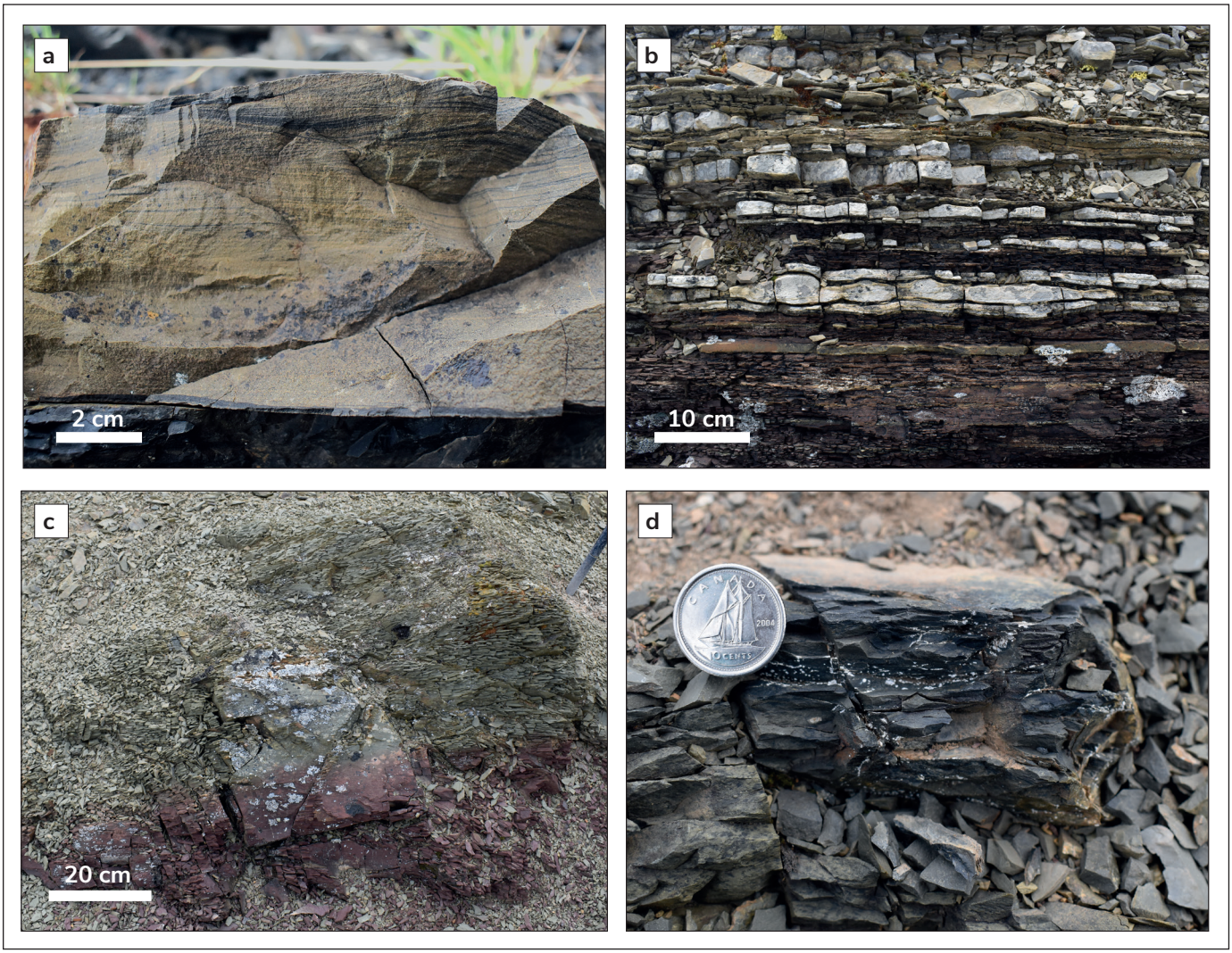

Figure 6. *Field photographs of siliciclastic facies of the Chandindu Formation and the Reefal assemblage.* ***(a)*** *Very fine quartz sandstone, with hummocky cross-stratification at the top of the bed.* ***(b)*** *Interbedded siliciclastic facies, predominantly composed of maroon shale and tan silt, with regular beds of very fine sandstone with calcite cement.* ***(c)*** *Typical outcrop of siltstone, grading from maroon to tan.* ***(d)*** *Typical example of black shale subcrop. Canadian dime, for scale, is 1.8 cm diameter.*

doloboundstone, and internal structure varies between unlaminated, faintly laminated low angle, and highly silicified high angle. Preservation quality is mixed at the outcrop scale, and one face displays a columnar, potentially dendritic texture (Fig. 5a). At the top of the exposure, 0.5 m bioherms are defined by low-angle laminations.

Above this, microspar-void dolomudstone contains abundant molar-tooth structure, chert bands and nodules. The top of the section consists of multiple cycles of microspar-void or parallel-laminated dolomudstone overlying microbialite doloboundstone.

Section G2442

This short section, between CS2410/11 and G2433/CS2414 (64.7305°N, 139.1768°W; Figs. 1b and 2, Table 2), was logged through a 50 m interval of dolostone that is absent from the G2433 ridge (only 200 m to the west). This outcrop comprises crudely medium-bedded, microspar-void dolomudstone, and pockets of darker dolomudstone with molar-tooth cements. Above the dolomudstone, black shale grades upward into grey siltstone, followed by green to maroon siltstone typical of the Chandindu Formation. We place the Chandindu–Reefal contact above the variegated siltstone, at the transition to dark soil interpreted to represent a thick

Table 1. *Lithofacies descriptions for the Reefal assemblage and Chandindu Formation, used for the stratigraphic logs in Figure 2. Gf: Gibben formation, CF: Chandindu Formation, Ra: Reefal assemblage and Cd: Craggy dolostone.*

Lithofacies	Description	Occurrence	Figure
debrite	Gravel to boulder-sized tabular, angular to subangular clasts. Some debrites are clast-supported, others are within a dolomudstone matrix. Clasts are primarily parallel-laminated dolomudstone, although some are extensively silicified.	Ra, Cd	3a
laminated microbialite doloboundstone	White to tan-weathering dolostone with crinkly lamination. Laminae are not laterally continuous and may be faint, marked by fenestrae and sheet cavities filled with microspar, or may be strongly resistant due to extensive silicification. Laminae vary in their orientation, and may be bedding parallel or at a high angle to bedding. There are domal stromatolites of 0.1–1 m radius.	Ra	4a–c
unlaminated microbialite doloboundstone	White to tan-weathering dolostone. Most outcrop faces are massive. Rare outcrop faces show irregular, low aspect-ratio cavities with no lamination or orientation (Figs. 5e and 6), which may be accentuated by silicification. Where well exposed, outcrop faces display columnar and dendritic growth of a microbialite framework, and cavities are (partially) filled by internal sediment.	Ra, CF	4d–f, 5a–d
sandy/silty carbonate mudstone	Interbedded dolomudstone with quartz silt or fine sand. Laminae/beds are 1–5 cm thick. Grey chert nodules are common in the thicker sand layers.	Ra	3b
microspar-void mudstone	Finely laminated calcimudstone or dolomudstone with distortion by voids filled with carbonate microspar cements. Many of these cements are the classic endmember form of molar-tooth structure as sheet-like ribbons with homogenous microspar (Kriscautzky et al., 2022). Others are round blebs or elongate seams of microspar (Fig. 3d). Internal brecciation is common.	Ra	3c,d
carbonate mudstone	Planar laminated (sub-mm scale) calcimudstone or dolomudstone. As dolomudstone, the facies is resistant and tan-weathering. As calcimudstone, it is fissile or flaggy and dark grey.	Ra, Gf	3e,f
sandstone	Bedded or channelized sandstone and conglomerate. Dominant lithology is moderately well-sorted, well-cemented fine quartz sandstone. Minor lithologies include very coarse angular lithic sandstone and pebble conglomerate.	CF	6a
interbedded siliciclastics	Interbedded silt, shale and either nodular dolostone or indurated very fine quartz sandstone with low-angle (hummocky) cross-stratification. Silt is generally maroon; grey shale is more resistant than subcropping black shale, common in these sections.	Ra	6b
siltstone	Maroon to grey-green weathering siltstone, commonly poorly laminated to massive.	Ra, CF	6c
shale	Black shale, often present as subcrop.	Ra, CF	6d

Table 2. *Coordinates for the base and top of the stratigraphic sections in Figures 1 and 2.*

Section	Base		Top	
	Latitude	Longitude	Latitude	Longitude
G2447	64.8024	-139.7402	64.7988	-139.7704
CS2418	64.7988	-139.7704	64.7939	-139.7861
CS2202	64.7898	-139.7398	64.7852	-139.7556
CS2201	64.7841	-139.7011	64.7782	-139.7017
CS2309	64.7486	-139.5730	64.7464	-139.5725
CS2312	64.7435	-139.5662	64.7425	-139.5646
G2433	64.7317	-139.1925	64.7284	-139.1847
CS2414	64.7284	-139.1847	64.7246	-139.1792
G2442	64.7305	-139.1768	64.7278	-139.1785
CS2410	64.7294	-139.1229	64.7266	-139.1204
CS2411	64.7266	-139.1204	64.7246	-139.1187

interval of weathered black (organic-rich) shale. This is followed by laminated microbialite forming small domes, and microspar-void dolomudstone.

The microspar-void dolomudstone interval appears to thin to the west from the base (Fig. 7) and is adjacent to maroon-weathering siltstone. Some high-angle, dip-slip fault planes were observed in the siltstone of G2442. The first shale-to-carbonate cycle in the overlying Reefal assemblage is laterally continuous between the two ridges.

Section G2433/CS2414

A more complete section of the Fifteenmile Group is preserved on a ridge 2.5 km west of CS2410/11 and 200 m west of G2442 (64.7284°N, 139.1847°W; Figs. 1b and 2, Table 2). The Gibben formation in this section unconformably overlies flaggy yellow dolostone of the Gillespie Lake Formation (Wernecke Supergroup). The Gibben formation lithology alternates between yellow and grey-laminated dolostone including irregular brown chert, and well-sorted oolitic grainstone. The coarse, poorly sorted grainstone defining the upper contact of the Gibben formation is overlain by siltstone, which is the dominant lithology throughout the Chandindu Formation, punctuated by intervals of sandstone or conglomerate that are 1 to 3 m thick. The sandstone is generally thinly parallel-bedded, fine-grained quartz sandstone, whereas the conglomerate is a quartz-pebble conglomerate with a muddy matrix. Sand content decreases up-section.

The Reefal assemblage begins as organic-rich, black shale subcrop. The first 65 m of the section has four shale-to-carbonate cycles, which include some or all of the following facies (but consistently in this order): black shale; dolomudstone with abundant molar-tooth structure; faintly laminated microbial doloboundstone; and microspar-void dolomudstone with internal brecciation and small, elongate microspar seams but no molar-tooth structure. The microbial doloboundstone at 26 m includes outcrop faces with unusually good preservation of branching stromatolites.

These cycles are capped by another black shale interval. This is overlain by a 9 m-thick debrite bed, comprising tabular, angular clasts (1–40 cm length) of parallel-laminated dolomudstone in a dolomudstone matrix. The succeeding layer of microspar-void dolomudstone has regularly spaced (every ~8 cm) interbeds containing spherical chert (1–3 mm in diameter), which we interpret as silicified coated grains, and grades into unlaminated microbial doloboundstone including localized crinkly lamination and internal breccia.

The last outcrop of dolomudstone before the thick interval of microbial doloboundstone includes molar-tooth structure and is extensively recrystallized, in places resembling zebra dolomitization. The thick

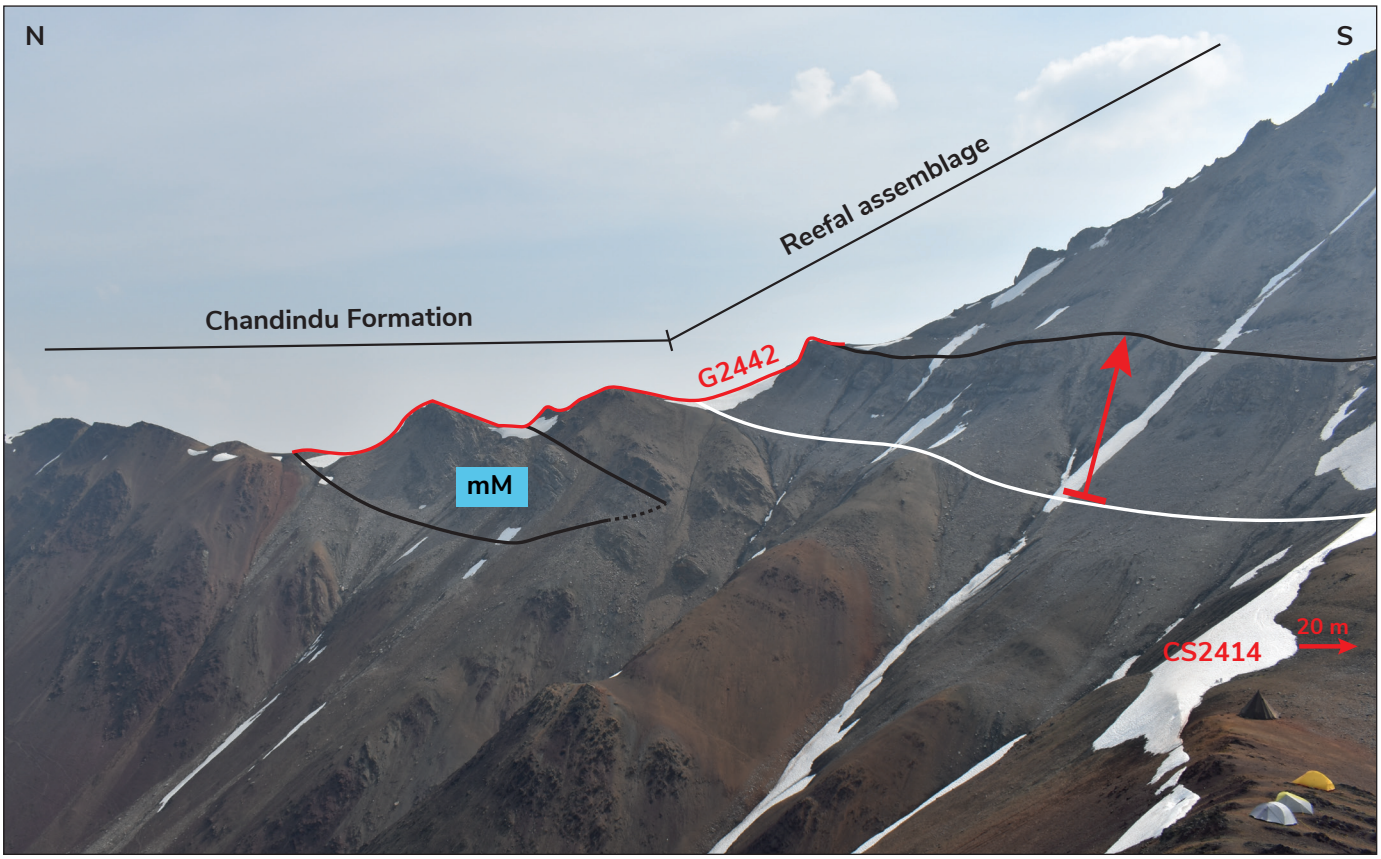

Figure 7. *Annotated photo of stratigraphic section G2442. An interval of microspar-void dolomudstone (mM) we assign to the Chandindu Formation thins to the west. The first shale-to-carbonate cycle (red arrow; black line is top of cycle) of the Reefal assemblage is laterally continuous across the ridge and is also measured by stratigraphic section CS2414. Tents, for scale, are ~2.5 m across.*

section of microbial doloboundstone begins at 130 m, and is generally massive with local preservation of cavities within the microbial framework, which are defined by curved protruding edges of the microbialite and filled with internal sediment (Fig. 5b). No clear lamination or growth direction is apparent. At the top of the exposure, the unlaminated microbialite forms domal bioherms ~1 m in diameter.

The thick microbialite interval is overlain by black shale interbedded with dark grey dolomudstone dominated by tabular internal breccia, which commonly forms decimetre-scale buckled folds reminiscent of tepee structures. This is followed by an interval of crinkly laminated, tan-weathering, recessive laminated microbialite doloboundstone. The rest of the section consists of mixed siliciclastic and fine-grained carbonate sedimentary rocks, including parallel-laminated dolomudstone containing shale partings and thin lenses of fine sand, dolomudstone with buckled tabular breccia, and interbedded black shale and dolomudstone with extensive molar-tooth structure and internal brecciation. The Reefal assemblage is capped by a distinctive 15 m-thick interval of interbedded maroon silt, shale, and very fine sandstone displaying hummocky cross-stratification (HCS), forming parasequences 1 to 2 m thick. At the base of the parasequences, very fine calcitic sandstone occurs in clear hummocks and swales within shale and silt, then sandstone layers become thicker and more laterally continuous toward the top of the parasequence. After an interval of recessive cover, the Craggy dolostone appears as a prominent outcrop of highly silicified, parallel-laminated, fine grainstone containing rare, low-angle cross-lamination and a tabular-clast breccia at its base.

Northern exposure belt (east to west)

Section CS2309/12

The exposure at this locality (64.7486°N, 139.5730°W; Figs. 1b and 2, Table 2) commences with discontinuous,

faintly laminated, microbial doloboundstone. The texture of these rocks is not clearly visible on outcrop faces, but irregular orange-weathering dolomite microspar cavities define discontinuous laminations that are predominantly parallel to regional bedding but are locally variable. At 91 m, the outcrop becomes laterally continuous across the ridge, and in the upper 5 m of doloboundstone, sheet cavities are lined by orange-weathering dolomite microspar. These microbialites are overlain by blue and red-weathering dolomudstones and calcimudstones, which can feature molar-tooth structure and round microspar blebs.

The next exposure is unlaminated microbialite, which at the base is highly silicified, accentuating vertical dendritic growth patterns similar to the dendritic face of CS2410/11 (at stratigraphic height of 170 m; Fig. 5a). Locally, this texture appears within metre-scale bioherms, where unlaminated microbialite is capped by silicified laminated stromatolites (Fig. 4f). Above the lowermost 5 m of the outcrop, the texture of the rock transitions to massive unlaminated microbialite doloboundstone. Lenses of debrites with silicified clasts were also found approximately 25 m along strike from the microbialite doloboundstone.

Above the unlaminated microbialite is a dip-slope of recessive shale, from which multiple isolated outcrops of faintly laminated microbialite emerge (Mb_L; Fig. 8a). The textures in these isolated build-ups are faintly laminated, in places exhibiting similarities to the columnar texture of the limestone in CS2418. Lamination orientation varies across the build-ups, and the south-facing edges have lamination approximately parallel to regional bedding, whereas the north-facing edges have lamination that is very steep relative to regional bedding (Fig. 8b).

Section CS2309 ends at the top of the microbialite outcrop, and section CS2312 (Fig. 1b) begins approximately 30 m stratigraphically above, and 200 m laterally, from the top of CS2309. This section commences with an outcrop of organic-rich shale overlain by unlaminated, massive, light-coloured dolomite we interpret as microbialite doloboundstone. Matrix-supported breccias of white, very fine carbonate also occur within these exposures, one of which has a sharp steep contact between breccia and microbialite, implying the clasts are derived from the microbialite. Above a thin interval of cover is a very coarse, highly silicified debrite, which we interpret as the base of the Craggy dolostone. Other debrite beds within the Craggy dolostone comprise tabular, silicified clasts, and local erosive bases.

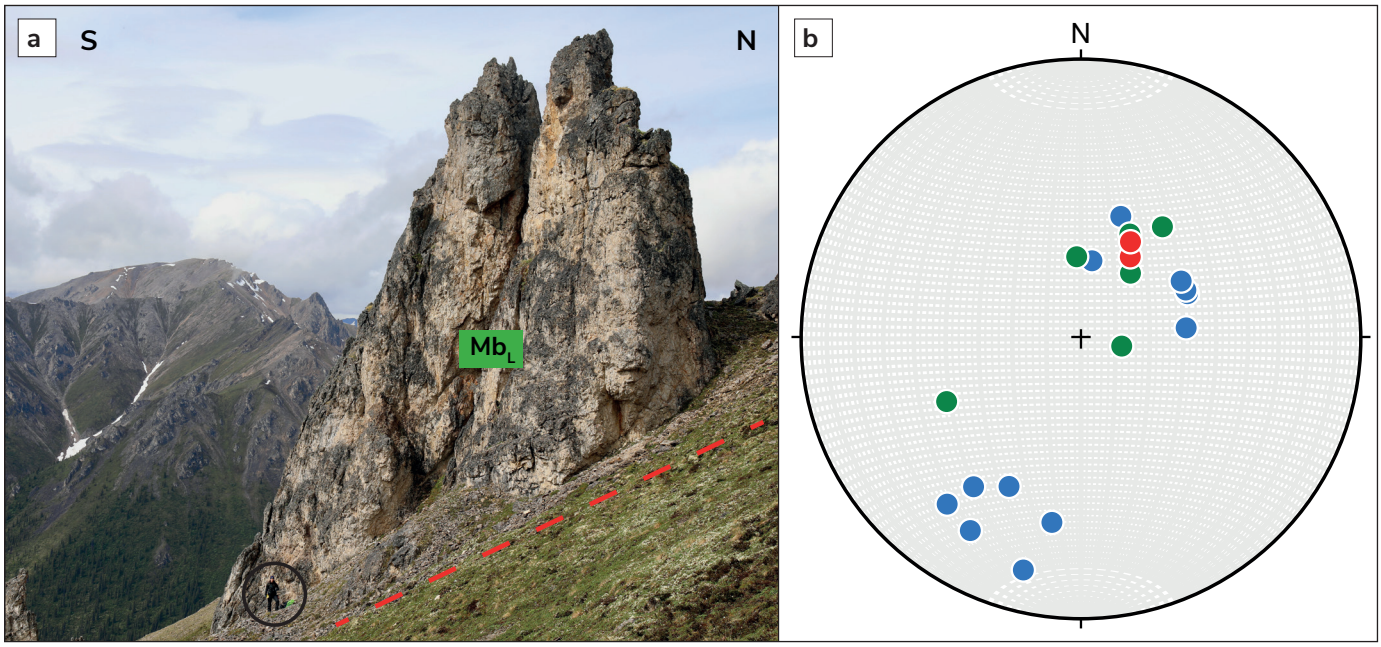

Figure 8. (a) *Annotated photo of isolated build-ups of laminated microbialite doloboundstone (Mb_L) emerging from a dip-slope (red dashed line). Location is adjacent to the top of stratigraphic section CS2309. Person for scale, circled in black.* ***(b)*** *Stereonet displaying poles to regional bedding (red), microbial lamination from isolated build-ups (blue) and microbial lamination from stratigraphic section CS2309 (green).*

Section CS2201

Section CS2201 (64.7842°N, 139.7010°W; Figs. 1b and 2, Table 2) begins with an abrupt transition from the red-weathering siltstone of the Chandindu Formation to organic-rich shale of the basal Reefal assemblage. The lowermost exposure of laminated microbialite at CS2201 is distinct from other sections, comprising localized partings of shale and internal brecciation between domal stromatolites with simple lamination and no cements or cavities. This interval is capped by a bed of siltstone and is followed by three successive beds of laminated microbialite with faint microspar-filled fenestrae, interbedded with black shale.

In the next 140 m of section, shale intervals alternate with various lithofacies of dolostone. In the lower part of this interval, the carbonate layers are highly brecciated molar-tooth dolomudstone that are significantly darker than the preceding microbialite. Up-section, the dolostone layers are faintly laminated tan-weathering microbialite doloboundstone, carbonate mudstone, and massive doloboundstone with no discernable features.

The uppermost 56 m of section CS2201 mostly comprises red shale to siltstone with thinly bedded, very fine grained quartz sandstone and orange dolostone, which become more common as interlayers up-section. This exposure is capped by laminated microbialite doloboundstone with metre-scale bioherms.

Section CS2202/G2235

The Chandindu Formation in this section (2.5 km west-northwest of section C2201: 64.7898°N, 139.7398°W; Figs. 1b and 2, Table 2) is dominated by siltstone, with beds of thinly laminated orange-weathering dolostone and coarse-grained quartz sandstone, which is typically laterally discontinuous. A transition from red-weathering mudstone to black shale marks the contact with the overlying Reefal assemblage. Four shale to microspar-void dolomudstone cycles follow, and contain molar-tooth structures in the upper 2–3 m of dolomudstone outcrop. The final cycle has microspar-void calcimudstone, rather than dolomudstone. This is followed by three intervals of faintly laminated microbialite doloboundstone, punctuated by shale and siltstone.

Section G2447/CS2418

In this section (1.6 km northwest of section CS2202: 64.8023°N, 139.7402°W; Figs. 1b and 2, Table 2), the Gibben formation overlies the yellow, flaggy dolomitic siltstone of the Gillespie Lake Group. The Gibben formation comprises medium-bedded, wavy laminated, grey-blue dolomudstone, with rare scour surfaces in the lower half of the section. The contact with the overlying Chandindu Formation begins with red-weathering shale and fine-grained quartz sandstone with polygonal (desiccation) cracks. The dominant lithology in the remaining section of Chandindu Formation is shaley siltstone, with abundant lenses of mostly fine, well-rounded quartz sandstone, and rare examples of dolomitic cement and HCS. By contrast, the more laterally continuous sandstone beds comprise angular, coarse-grained lithic sandstones. Microbialites and other carbonates are more abundant in this section than in sections farther east. The microbialites are dominated by unlaminated facies, with distinctive white to light grey cements in some beds highlighting the clotted texture. Microbialites variably form discontinuous metre-scale thick beds, commonly interbedded with shale, or low-relief metre-scale mounds.

The top of the Chandindu Formation is a well-cemented sandstone: a 3-m interval of quartz wacke with a distinct 10-cm bed of angular, very coarse lithic sandstone. Black shale dominates the first 90 m of the Reefal assemblage. Above the black shale interval, three cycles of calcimudstone contain extensive molar-tooth structure, grading into bedded organic-rich planar laminated calcimudstone. Above are six cycles with a reverse gradation of facies: shale, to fissile planar-laminated calcimudstone, to organic-rich wavy bedded calcimudstone, to thickly bedded calcimudstone with extensive molar-tooth structure.

The following 12 m section of limestone microbialite is exceptionally well preserved compared to the dolomite microbialite boundstone in other sections. It displays primary microbial textures, including differentiation between dense, locally columnar, clotted microbial framework, and cavities filled with internal sediment (Fig. 5c, d). Cavities are defined by protrusions of the microbialite, and in some cases, partial fill defines geopetal structures in which two generations of carbonate cement can be discerned (Fig. 5c). These geopetal structures are only seen in the centre of the outcrop. Within 5 m of the base and top, cavities are completely filled by internal sediment, and in the uppermost and lowermost 2 m of the exposure, the texture is obscured, transitioning into coarse mottling between grey and orange-weathering dolomite.

Above the limestone microbialite, alternating shale and silt are interbedded with 2–10 cm beds of well-indurated, very fine grained quartz sandstone with

low-angle cross stratification and nodular dolostone. Three subsequent, laterally discontinuous, outcrops of microbialite doloboundstone, separated by molar-tooth dolomudstone and black shale subcrop, have localized extensive silicification. Some faces with limited weathering reveal cavities partially filled with internal sediment. The uppermost microbialite doloboundstone weathers orange, and some cavities have a flat base and digitate roof (i.e., 'stromatactis' sensu, Aubrecht, 2011). Overlying shales are interbedded with nodular dolomite and indurated, very fine grained, HCS quartz sandstone.

The substantial unlaminated microbialite doloboundstone buildup in this section manifests predominantly as massive dolomite, with no visible cavities. Less weathered outcrop faces and blocks in float reveal faint cavities similar to the laterally discontinuous blocks and exceptionally preserved limestone microbialite below. No significant change in texture occurs up-section. The interval above the reef buildup is covered by vegetation, but laterally, the reefal buildup is draped by black shale (Fig. 9).

Above the covered, black shale interval is a succession of interbedded shale, silt, indurated very fine grained quartz sandstone, and planar-laminated limestone. It is overlain by tan-weathering laminated dolomite with extensive, buckled tabular internal breccia, and tepee structures. After 52 m, a prominent outcrop of recrystallized parallel-laminated grainstone defines the base of the Craggy dolostone.

Discussion

Facies associations

Both types of microbialite doloboundstone form extensive, laterally discontinuous outcrops, at times adjacent to shale (Fig. 9b). Certain sections also include shale-adjacent, discontinuous outcrops of microspar-void dolomudstone facies (e.g., Fig. 7). We therefore define the relief-forming reef core by the lithofacies assemblage of laminated microbialite doloboundstone, unlaminated microbialite doloboundstone and microspar-void dolomudstone. The facies adjacent to the reef core may be preliminarily split into two facies associations. The first is an association of carbonate mudstone, interbedded siliciclastics and laterally continuous beds of laminated microbialite (e.g., 244–364 m of CS2414, 179–205 m and 509–562 m of CS2418; Fig. 2). Given the presence of tepees, buckled internal breccia, low-relief stromatolites and HCS, we consider this facies association to be deposited in intertidal to supratidal water depth with periodic restriction, and therefore represents a back-reef lagoon on the proximal side of the reef core. By contrast, we consider the association of molar-tooth-dominated dolomudstone, debrite and shale to reflect deposition on a distally steepened ramp, and thick intervals of shale correspond to basinal deposition below storm-weather wave base.

Record of reef development

The sections spanning the Reefal assemblage demonstrate an overall up-section increase in the proportion of reef core lithofacies, particularly unlaminated microbialite doloboundstone. Although there is substantial variability across the inlier, the general trend is a transition from thick successions of shale with intervening microspar-void dolomudstone, to isolated outcrops of microbialite doloboundstone, to laterally continuous exposures of (generally unlaminated) microbialite doloboundstone up to 115 m thick. This transition is particularly apparent in the westernmost sections of both exposure belts in the Coal Creek inlier (CS2414 and CS2418; Fig. 1b). In the easternmost section of the northern belt (CS2309/12), patchy laminated microbialite precedes the onset of more substantial coverage.

We suggest that this transition is due to an overall shallowing and progradation of reefs as the basin filled, as inferred by Macdonald et al. (2012). In isolation, the increasing abundance of unlaminated microbialite is a poor depth indicator, given that Precambrian unlaminated microbialites have been inferred to develop in variable water depths and settings, including the deep slope and basin floor (Little Dal Group; Turner et al., 1997; Batten et al., 2004), lower-subtidal settings (Wumishan Formation; Tang et al., 2013), and near-vertical deep escarpments (Balcanoona Formation; Wallace et al., 2015). However, the increase in substantial unlaminated microbialite up-section is also accompanied by a decrease in the abundance of shale, as well as the appearance of a) interbedded siliciclastic facies with nodular limestone beds and fine HCS sandstone; and b) dolomudstone with tepee structures and buckled tabular breccias. Hummocky cross-stratification is characteristic of deposition between fair and storm-weather wave base (Dumas and Arnott, 2006), whereas tepees and buckled tabular breccia are characteristic of deposition in an intertidal to supratidal environment, where evaporation induces fluid escape and carbonate cementation (Kendall and Warren, 1987). Therefore, both facies represent a much

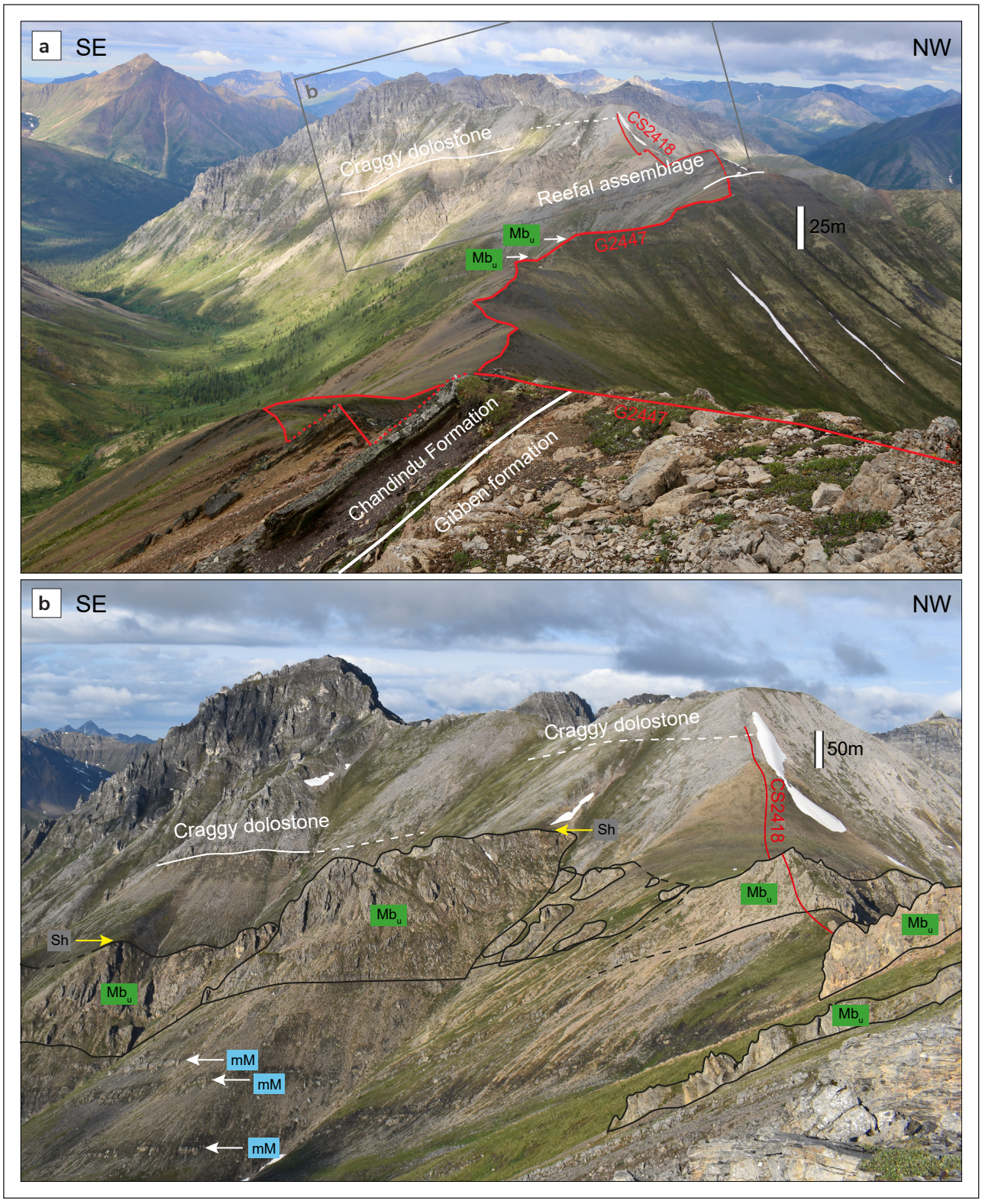

Figure 9. (a) *Annotated photo of stratigraphic section G2447. White arrows denote outcrops of unlaminated (clotted) microbialite (Mb_u).* ***(b)*** *Inset of (a); annotated photo of CS2418. Black outlines denote reefal outcrops of unlaminated microbialite, and yellow arrows denote the abrupt contact with black shale (Sh) above the southeastern outcrop. White arrows denote exposures of microspar-void dolomudstone (mM) capping shale-to-carbonate cycles. Scale varies with perspective; in both subplots, scale bars are applicable to their relevant place in the section.*

shallower depositional setting than the organic-rich shale characteristic of most of the Reefal assemblage. The interbedded siliciclastic facies is a common feature in the uppermost part of the Reefal assemblage (sections CS2418, CS2201 and CS2414), suggesting that by this point, shallow environments extended across the basin and terrigenous input may have increased. Furthermore, this shallowing-up sequence is followed conformably by the onset of the Craggy dolostone carbonate platform.

Within this context of an overall progradational succession, we identified regular, smaller-scale, shale-to-carbonate cycles in some sections of the Reefal assemblage. We interpret these as higher order transgressive-regressive cycles (Fig. 2), reflecting some combination of shallowing and increased carbonate saturation, possibly related to basin restriction. Regression is represented by a common motif of shale followed by molar-tooth carbonate mudstone. This motif varies across the basin; for example, section CS2418 also has an organic-rich calcimudstone facies between shale and molar-tooth calcimudstone. In section CS2414, the shale and molar-tooth dolomudstone is succeeded by faintly laminated microbialite doloboundstone and microspar-void dolomudstone with blebs and seams rather than molar-tooth structure. These latter facies may represent a lowstand system tract during which the basin was restricted. The generally sharp contacts with black shale atop each cycle are interpreted to record flooding with minimal to no transgressive systems tract being preserved.

The pattern of shale-to-carbonate cycles followed by thick, laterally extensive, microbialite is not seen in stratigraphic section CS2410/11. Here, reef core lithofacies begin lower in the section, and non-microbial facies are rare above this level. We interpret this difference to reflect a proximal setting closer to the reef core. As a result, high-order shale-to-carbonate cycles are absent, though changes in base level may correlate with shifts in the dominant microbialite morphology from laminated to unlaminated. At present, this remains a hypothesis, as our preliminary study cannot conclusively assign a depth control on microbialite morphology.

Significance of microbialite textures

The unlaminated microbialite calciboundstone in CS2418 (stratigraphic height 168 m) is exceptionally well-preserved (Fig. 5c, d). In four of our seven sections, we identified comparable features in rare preservation windows in otherwise massive and featureless dolostone. Although neither the internal structure of the microbialite nor different cement generations can be discerned in the field, preservational windows display cavities defined by clotted protrusions of microbialite, and columnar features and internal sediment (Fig. 5b) reveal their similar morphology to the calciboundstone in CS2418. Therefore, given the spectrum of unlaminated microbialite features, from featureless (Fig. 4d) to clotted, columnar and cavity-dense (Fig. 5c, d), we suggest that all the 'unlaminated microbialite doloboundstone' of the Reefal assemblage was originally framework-building, clotted microbialite similar to the calciboundstone in CS2418. The primary features of this microbialite are variably obscured by a variety of late-stage recrystallization and poor outcrop.

There are notable similarities and differences between the reefal textures of the Reefal assemblage and the deep-water reefs of the lower Little Dal Group (Stone Knife and Silverberry formations), which is thought to correlate to the Fifteenmile Group (Thomson et al., 2015a, b). The Little Dal reefs are also constructed by a mixture of laminated ('lamelliform') and unlaminated ('dendritic/clotted') microbialite textures (Turner et al., 1997). In addition, the shape of cavities in well-preserved calciboundstone and doloboundstone in the Reefal assemblage is very similar to the shape of cavities in the Little Dal clotted microbialite (Fig. 18.15b in James and Jones, 2015; Fig. 2f, g in Turner, 2021). However, the two reef systems differ in their scale and their depositional environment. The unlaminated microbialite reefs of the Little Dal had up to 100 m of topographic relief above a deep slope (Turner et al., 1997). By contrast, Reefal assemblage reefs formed in proximal environments (Macdonald et al., 2012). There is evidence that Reefal assemblage reefs formed on topographic highs, given the talus and olistoliths in basinal settings (Macdonald et al., 2012), and here we provide evidence that the reefs themselves were relief-forming, given the change in bedding orientation associated with isolated reef build-ups (Fig. 8) and the onlap of shale onto large reef exposures (e.g., Fig. 9b). However, we find no clear evidence for significant, continuous escarpments, or paleotopography on the scale of the Little Dal (up to 100 m). Nevertheless, the shale-to-carbonate repetitions in the basin, as well as the presence of talus and olistoliths (Macdonald et al., 2012), demonstrate that the Reefal assemblage was a long-lived, basin-scale carbonate factory.

Lateral variability in the Chandindu Formation

Our findings support previous lithological studies of the Chandindu Formation that identified siltstone and minor outcrops of sandstone, shale, dolomudstone, and a variable abundance of generally laterally discontinuous or mounded microbialite (Macdonald et al., 2012 Kunzmann et al., 2014). We note a bimodal distribution of coarse siliciclastic sediments: gritty, coarse, angular lithic sandstone, and fine, rounded, quartz sandstone with intermittent HCS. This likely reflects two distinct sediment sources, one more proximal and one more distal, and/or variably hyperpycnal and hypopycnal flow from delta channels (Zavala, 2020).

We note the higher proportion of carbonate in the western sections of the Chandindu Formation, and the clotted microbialite in the westernmost section (CS2418), which is similar to the unlaminated microbialite identified in the Reefal assemblage. We suggest that this demonstrates that marine conditions in the basin were already suitable for unlaminated reef development during deposition of the Chandindu Formation. However, as argued by Kunzmann et al. (2014), substantial reef development was generally prevented by the regular input of terrigenous detritus (e.g., through delta lobe switching), which may have been linked to ongoing extension and footwall uplift at this time (Macdonald et al., 2012). This interpretation also provides an explanation for the 50 m of microspar-void dolomudstone in the Chandindu Formation at section G2442. The continuity of the first shale-to-carbonate cycle of the Reefal assemblage (Fig. 7) suggests that the underlying microspar-void dolomudstone belongs to the Chandindu Formation and may be linked to proximal reef development. Furthermore, we placed the base of CS2410 above an approximately 100 m interval of microspar-void dolomudstone and unlaminated microbialite doloboundstone, assuming a thrusted contact. However, it is plausible that these lower reef facies belong to the Chandindu Formation, representing a successful reef in proximal settings.

The thicknesses of our complete measured sections of the Chandindu Formation (186 m for G2433, 540 m for G2447) differ significantly from one another and from the adjacent sections measured by Kunzmann et al. (2014). The discrepancy with previous studies may be partially explained by our recognition that the contact, as defined by an abrupt flooding and deposition of black shale, in places overlies interbedded coarse clastic rocks and microbial build-ups, which were originally assigned to the Reefal assemblage. The difference between our measured thicknesses and those of adjacent sections further emphasizes the pronounced basin topography that influenced deposition of the Fifteenmile Group.

Conclusion

Our findings support previous work (Macdonald et al., 2012) demonstrating that the Reefal assemblage is a basin-scale carbonate factory deposited in an overall progradational system in a basin with inherited extension-related topography. Suitable conditions for reef development began during deposition of the uppermost Chandindu Formation, although continuous siliciclastic input hampered substantial reef development. We have defined the contact between the Chandindu Formation and the Reefal assemblage as the distinct black shale flooding surface, which we interpret to strongly correlate across the basin, and above which siltstone is no longer the dominant lithology.

The Reefal assemblage is characterized by platformal microbialite, which alternates between laminated and unlaminated facies, and shale-to-carbonate cycles in the adjacent shale basin. The unlaminated facies of the reef was a framework-constructing microbialite, which is now primarily preserved as recrystallized massive dolostone, with primary growth features seen in rare preservation windows. These well-preserved microbialites have similar morphologies to the unlaminated reef systems in the Little Dal Group. Our work therefore provides additional evidence in favour of a transition in the nature of dominant reef-builders during the Tonian period.

Acknowledgments

We acknowledge that this project took place on the Traditional Territory of the Tr'ondëk Hwëch'in First Nation, and we are grateful for their permission to work on this land. The project was supported by the Polar Continental Shelf Program and NSERC Discovery and Northern Research Supplement grants to G. Halverson. Fireweed Helicopters provided safe and reliable transport to the field. We thank Lucy Webb, Maggie Whelan, Elizabeth Sullivan, Tyler Ambrose, Maddie Norman and Caroline Dee for their assistance in the field. We thank Rob Rainbird for his detailed review, which greatly improved this manuscript.

References

Aitken, J.D., 1967. Classification and environmental significance of cryptalgal limestones and dolomites, with illustrations from the Cambrian and Ordovician of southwestern Alberta. Journal of Sedimentary Research, vol. 37, p. 1163–1178. https://doi.org/10.1306/74D7185C-2B21-11D7-8648000102C1865D

Aubrecht, R., 2011. Stromatactis. *In*: Encyclopedia of Geobiology. Encyclopedia of Earth Sciences Series. J. Reitner and V. Thiel, (eds.), Springer Netherlands, Dordrecht, p. 847–850. https://doi.org/10.1007/978-1-4020-9212-1_226

Batten, K.L., Narbonne, G.M. and James, N.P., 2004. Paleoenvironments and growth of early Neoproterozoic calcimicrobial reefs: platformal Little Dal Group, northwestern Canada. Precambrian Research, vol. 133, p. 249–269. https://doi.org/10.1016/j.precamres.2004.05.003

Busch, J.F., Rooney, A.D., Meyer, E.E., Town, C.F., Moynihan, D.P. and Strauss, J.V., 2021. Late Neoproterozoic – early Paleozoic basin evolution in the Coal Creek inlier of Yukon, Canada: implications for the tectonic evolution of northwestern Laurentia. Canadian Journal of Earth Sciences, vol. 58, p. 355–377. https://doi.org/10.1139/cjes-2020-0132

Cohen, P.A., Strauss, J.V., Rooney, A.D., Sharma, M. and Tosca, N., 2017. Controlled hydroxyapatite biomineralization in an ~810 million-year-old unicellular eukaryote. Science Advances, vol. 3, issue 6, e1700095, https://www.science.org/doi/10.1126/sciadv.1700095

Colpron, M., Israel, S., Murphy, D., Pigage, L. and Moynihan, D., 2016. Yukon bedrock geology map. Yukon Geological Survey, Open File 2016-1, scale 1:1 000 000, map and legend.

Dumas, S. and Arnott, R.W.C., 2006. Origin of hummocky and swaley cross-stratification—The controlling influence of unidirectional current strength and aggradation rate. Geology, vol. 34, no. 12, p. 1073–1076. https://doi.org/10.1130/G22930A.1

Furlanetto, F., Thorkelson, D.J., Gibson, H.D., Marshall, D.D., Rainbird, R.H., Davis, W.J., Crowley, J.L. and Vervoort, J.D., 2013. Late Paleoproterozoic terrane accretion in northwestern Canada and the case for circum-Columbian orogenesis. Precambrian Research, vol. 224, p. 512–528. https://doi.org/10.1016/j.precamres.2012.10.010

Gibson, T.M., Faehnrich, K., Busch, J.F., McClelland, W.C., Schmitz, M.D. and Strauss, J.V., 2021. A detrital zircon test of large-scale terrane displacement along the Arctic margin of North America. Geology, vol. 49, no. 5, p. 545–550. https://doi.org/10.1130/G48336.1

Gibson, T.M., Kunzmann, M., Poirier, A., Schumann, D., Tosca, N.J. and Halverson, G.P., 2020. Geochemical signatures of transgressive shale intervals from the 811 Ma Fifteenmile Group in Yukon, Canada: Disentangling sedimentary redox cycling from weathering alteration. Geochimica et Cosmochimica Acta, vol. 280, p. 161–184. https://doi.org/10.1016/j.gca.2020.04.013

Green, L.H., 1972. Geology of Nash Creek, Larsen Creek, and Dawson map areas, Yukon Territory. Geological Survey of Canada, Memoir 364, 157 p. https://doi.org/10.4095/100697

Greenman, J.W., Rainbird, R.H. and Turner, E.C., 2020. High-resolution correlation between contrasting early Tonian carbonate successions in NW Canada highlights pronounced global carbon isotope variations. Precambrian Research, vol. 346, 105816. https://doi.org/10.1016/j.precamres.2020.105816

Greenman, J.W., Rooney, A.D., Patzke, M., Ielpi, A. and Halverson, G.P., 2021. Re-Os geochronology highlights widespread latest Mesoproterozoic (ca. 1090–1050 Ma) cratonic basin development on northern Laurentia. Geology, vol. 49, no. 7, p. 779–783. https://doi.org/10.1130/G48521.1

Grotzinger, J.P. and James, N.P., 2000. Precambrian carbonates: Evolution of understanding. *In*: Carbonate Sedimentation and Diagenesis in the Evolving Precambrian World, J.P. Grotzinger and N.P. James (eds.), SEPM Society for Sedimentary Geology, p. 320.

Halverson, G.P., Macdonald, F.A., Strauss, J.V., Smith, E.F., Cox, G.M. and Hubert-Théou, L., 2012. Updated definition and correlation of the lower Fifteenmile Group in the central and eastern Ogilvie Mountains. *In*: Yukon Exploration and Geology 2011, K.E. MacFarlane and P.J. Sack (eds.), Yukon Geological Survey, p. 75–90.

Halverson, G.P., Shen, C., Davies, J.H.F.L. and Wu, L., 2022. A Bayesian approach to inferring depositional ages applied to a Late Tonian reference section in Svalbard. Frontiers in Earth Science vol. 10. https://doi.org/10.3389/feart.2022.798739

James, N.P. and Jones, B., 2015. Origin of carbonate sedimentary rocks. John Wiley & Sons, West Sussex, UK, 454 p.

Kalkowsky, E., 1908. Oolith und Stromatolith im norddeutschen Buntsandstein. Zeitschrift der Deutschen Geologischen Gesellschaft vol. 60, p. 68–125. https://doi.org/10.1127/zdgg/60/1908/68

Kendall, C.G.St.C. and Warren, J., 1987. A review of the origin and setting of tepees and their associated fabrics. Sedimentology, vol. 34, p. 1007–1027. https://doi.org/10.1111/j.1365-3091.1987.tb00590.x

Kriscautzky, A., Kah, L.C. and Bartley, J.K., 2022. Molar-tooth structure as a window into the deposition and diagenesis of Precambrian carbonate. Annual Review of Earth and Planetary Sciences, vol. 50, p. 205–230. https://doi.org/10.1146/annurev-earth-031621-080804

Kunzmann, M., Halverson, G., Macdonald, F., Hodgskiss, M., Sansjofre, P., Schumann, D. and Rainbird, R., 2014. The early Neoproterozoic Chandindu Formation of the Fifteenmile Group in the Ogilvie Mountains, *In*: Yukon Exploration and Geology 2013, K.E. MacFarlane, M.G. Nordling and P.J. Sack, (eds.), Yukon Geological Survey, p. 93–107.

Macdonald, F.A. and Roots, C.F., 2010. Upper Fifteenmile Group in the Ogilvie Mountains and correlations of early Neoproterozoic strata in the northern Cordillera. *In*: Yukon Exploration and Geology 2009, K.E. MacFarlane, L.H. Weston and L.R. Blackburn (eds.), Yukon Geological Survey, p. 237–252.

Macdonald, F.A., Halverson, G., Strauss, J., Smith, E., Cox, G., Sperling, E. and Roots, C., 2012. Early Neoproterozoic Basin Formation in Yukon, Canada: Implications for the make-up and break-up of Rodinia. Geoscience Canada, vol. 39, no. 2, p. 77–100.

Macdonald, F.A., Schmitz, M.D., Crowley, J.L., Roots, C.F., Jones, D.S., Maloof, A.C., Strauss, J.V., Cohen, P.A., Johnston, D.T. and Schrag, D.P., 2010a. Calibrating the Cryogenian. Science, vol. 327, issue 5970, p. 1241–1243. https://doi.org/10.1126/science.1183325

Macdonald, F.A., Smith, E.F., Strauss, J.V., Cox, .M., Halverson, G.P. and Roots, C.F., 2010b. Neoproterozoic and early Paleozoic correlations in the western Ogilvie Mountains, Yukon. *In*: Yukon Exploration and Geology 2011, K.E. MacFarlane, L.H. Weston and C. Relf (eds.), Yukon Geological Survey, p. 161–182.

Medig, K.P.R., Turner, E.C., Thorkelson, D.J. and Rainbird, R.H., 2016. Rifting of Columbia to form a deep-water siliciclastic to carbonate succession: The Mesoproterozoic Pinguicula Group of northern Yukon, Canada. Precambrian Research, vol. 278, p.179–206. https://doi.org/10.1016/j.precamres.2016.03.021

Rainbird, R.H., Jefferson, C.W. and Young, G.M., 1996. The early Neoproterozoic sedimentary Succession B of northwestern Laurentia: Correlations and paleogeographic significance. GSA Bulletin vol. 108, no. 4, p. 454–470. https://doi.org/10.1130/0016-7606(1996)108<0454:TENSSB>2.3.CO;2

Rooney, A.D., Strauss, J.V., Brandon, A.D. and Macdonald, F.A., 2015. A Cryogenian chronology: Two long-lasting synchronous Neoproterozoic glaciations. Geology, vol. 43, no. 5, p. 459–462. https://doi.org/10.1130/G36511.1

Semikhatov, M.A., Gebelein, C.D., Cloud, P., Awramik, S.M. and Benmore, W.C., 1979. Stromatolite morphogenesis—progress and problems. Canadian Journal of Earth Sciences, vol. 16, no. 5, p. 992–1015. https://doi.org/10.1139/e79-088

Shapiro, R.S., 2000. A Comment on the systematic confusion of thrombolites. Palaios, vol. 15, no. 2, p. 166–169. https://doi.org/10.1669/0883-1351(2000)015<0166:ACOTSC>2.0.CO;2

Sperling, E.A., Halverson, G.P., Knoll, A.H., Macdonald, F.A. and Johnston, D.T., 2013. A basin redox transect at the dawn of animal life. Earth and Planetary Science Letters, vols. 371–372, p. 143–155. https://doi.org/10.1016/j.epsl.2013.04.003

Strauss, J.V., Roots, C.F., MacDonald, F.A., Halverson, G.P., Eyster, A. and Colpron, M., 2014. Geological map of the Coal Creek Inlier, Ogilvie Mountains (NTS 116B/10-15 and 116C/9, 16). Yukon Geological Survey, Open File 2014-15, scale 1:100 000.

Strauss, J.V., MacDonald, F.A., Halverson, G.P., Tosca, N.J., Schrag, D.P. and Knoll, A.H., 2015. Stratigraphic evolution of the Neoproterozoic Callison Lake Formation: Linking the break-up of Rodinia to the Islay carbon isotope excursion. American Journal of Science, vol. 315, p. 881–944. https://doi.org/10.2475/10.2015.01

Tang, D., Shi, X. and Jiang, G., 2013. Mesoproterozoic biogenic thrombolites from the North China platform. International Journal of Earth Sciences, vol. 102, p. 401–413. https://doi.org/10.1007/s00531-012-0817-9

Thompson, R.I. and Roots, C.F., 1982. Ogilvie Mountains project, Yukon; Part A: a new regional mapping program. Geological Survey of Canada, Paper 82-1A, p. 403–411 https://doi.org/10.4095/111324

Thompson, R.I., Roots, C.F. and Mustard, P.S., 1994. Geology of Dawson map area (116B,C) (northeast of Tintina Trench). Geological Survey of Canada, Open File, 2849. https://doi.org/10.4095/194830

Thomson, D., Rainbird, R.H. and Krapez, B., 2015a. Sequence and tectonostratigraphy of the Neoproterozoic (Tonian-Cryogenian) Amundsen Basin prior to supercontinent (Rodinia) breakup. Precambrian Research, vol. 263, p. 246–259. https://doi.org/10.1016/j.precamres.2015.03.001

Thomson, D., Rainbird, R.H., Planavsky, N., Lyons, T.W. and Bekker, A., 2015b. Chemostratigraphy of the Shaler Supergroup, Victoria Island, NW Canada: A record of ocean composition prior to the Cryogenian glaciations. Precambrian Research, vol. 263, p. 232–245. https://doi.org/10.1016/j.precamres.2015.02.007

Thorkelson, D.J., Abbott, J.G., Mortensen, J.K., Creaser, R.A., Villeneuve, M.E., McNicoll, V.J. and Layer, P.W., 2005. Early and middle Proterozoic evolution of Yukon, Canada. Canadian Journal of Earth Sciences, vol. 42, p. 1045–1071.

Turner, E.C., 2021. Possible poriferan body fossils in early Neoproterozoic microbial reefs. Nature, vol. 596, p. 87–91. https://doi.org/10.1038/s41586-021-03773-z

Turner, E.C., James, N.P. and Narbonne, G.M., 1997. Growth dynamics of Neoproterozoic calcimicrobial reefs, Mackenzie Mountains, Northwest Canada. Journal of Sedimentary Research, vol. 67, p. 437–450. https://doi.org/10.1306/D4268590-2B26-11D7-8648000102C1865D

Turner, E.C., James, N.P. and Narbonne, G.M., 2000. Taphonomic control on microstructure in early Neoproterozoic reefal stromatolites and thrombolites. Palaios, vol. 15, p. 87–111.

Turner, E.C., Narbonne, G.M. and James, N.P., 1993. Neoproterozoic reef microstructures from the Little Dal Group, northwestern Canada. Geology, vol. 21, no. 3, p. 259–262. https://doi.org/10.1130/0091-7613(1993)021<0259:NRMFTL>2.3.CO;2

Wallace, M.W., Hood, A.v.S., Woon, E.M.S., Giddings, J.A. and Fromhold, T.A., 2015. The Cryogenian Balcanoona reef complexes of the Northern Flinders Ranges: Implications for Neoproterozoic ocean chemistry. Palaeogeography, Palaeoclimatology, Palaeoecology, vol. 417, p. 320–336. https://doi.org/10.1016/j.palaeo.2014.09.028

Young, G.M., Jefferson, C.W., Delaney, G.D. and Yeo, G.M., 1979. Middle and late Proterozoic evolution of the northern Canadian Cordillera and Shield. Geology, vol. 7, no. 3, p. 125–128. https://doi.org/10.1130/0091-7613(1979)7<125:MALPEO>2.0.CO;2

Zavala, C., 2020. Hyperpycnal (over density) flows and deposits. Journal of Palaeogeography, vol. 9, article 17. https://doi.org/10.1186/s42501-020-00065-x

Yukon Geological Survey

Yukon Geological Survey staff are located in two buildings in Whitehorse: the Elijah Smith Building at 300 Main Street, room 102, and the H.S. Bostock Core Library at Mile 918 on the Alaska Highway.

Operations

Elijah Smith Building

Relf, Carolyn – Director, (867) 667–8892 ..... carolyn.relf@yukon.ca
Annau, Tamara – Supervisor, Finance & Operations, (867) 667–8508 ..... tamara.annau@yukon.ca

Bedrock Geology

H.S. Bostock Core Library

Colpron, Maurice – Head, Bedrock Geology, (867) 667–8235 ..... maurice.colpron@yukon.ca
Ambrose, Tyler – Project Geologist, (867) 667–5175 ..... tyler.ambrose@yukon.ca
Cobbett, Rosie – Project Geologist, (867) 455–2802 ..... rosie.cobbett@yukon.ca
Moynihan, David – Project Geologist, (867) 455–2805 ..... david.moynihan@yukon.ca
Schultz, Sarah – Project Geologist, (867) 332–0846 ..... sarah.schultz@yukon.ca
Vacant – Project Geologist

Surficial Geology

H.S. Bostock Core Library

Cronmiller, Derek – Head, Surficial Geology, (867) 332–4961 ..... derek.cronmiller@yukon.ca
Lipvosky, Panya – Surficial Geologist, (867) 667–8520 ..... panya.lipovsky@yukon.ca
Painter, Moya – Permafrost Geologist, (867) 667–8514 ..... moya.painter@yukon.ca
Stewart-Jones, Emilie – Transportation Geohazard Specialist (joint position with Transportation Planning Branch, HPW), (867) 332–2530 ..... emilie.stewart-jones@yukon.ca
Vacant – Surficial Geologist

Elijah Smith Building

van Loon, Sydney – Placer Geology Technician, (867) 332–3324 ..... sydney.vanloon@yukon.ca

Minerals Geology

H.S. Bostock Core Library

Sack, Patrick – Head, Minerals Geology, (867) 667–3203 ..... patrick.sack@yukon.ca
Brubacher, Alex – Economic Geologist, (867)334–6314 ..... alex.brubacher@yukon.ca
Ellis, Sarah – Economic Geologist, (867) 332–9263 ..... sarah.ellis@yukon.ca
Naber, Tiera – Economic Geologist, (867) 456–3828 ..... tiera.naber@yukon.ca
Skerget, Spencer – Core Library Manager, (867) 393–6492 ..... spencer.skerget@yukon.ca
Vacant – Mineral Assessment Geologist

Technical Services & Outreach

Elijah Smith Building

Stuart, Amy – Manager, Technical Services, (867) 332–7865 ..... amy.stuart@yukon.ca
Côté, Chad – Geological Spatial Database Administrator, (867) 393–7186 ..... chad.cote@yukon.ca
Elliot, Brett – Geological Spatial Database Administrator (Temporary Assignment)
O'Connor, Amanda – Outreach Geologist, (867) 332–9376 ..... amanda.oconnor@yukon.ca
Staffen, Bailey – GIS Technician/Web Manager (Temporary Assignment)
Weston, Leyla – Outreach Geologist, (867) 393–7187 ..... leyla.weston@yukon.ca

Yukon Geological Survey
Energy, Mines and Resources
Government of Yukon